# Durham E-Theses

## *Bound states of Van der Waals trimers*

Wright, Nicholas J.

# Bound states of Van der Waals trimers.

## Nicholas J. Wright

Ph.D Thesis

Chemistry Department

University of Durham

1998

# Abstract of Ph.D Thesis

# 'Bound states of Van der Waals trimers.'

# Nicholas J. Wright, University of Durham, October 1998

A method for calculating the energy levels and wave functions of floppy triatomic systems such as rare-gas trimers has been developed. It is based upon a potential-optimized discrete variable representation and takes into account the wide-amplitude vibrations that occur in such systems. The quadrature error that occurs in DVR calculations is analysed and a method of correction implemented. The diagonalisation procedure is based upon a combination of successive diagonalisation and truncation and a Lanczos diagonaliser.

Using this method the wave functions of the $Ar_3$ Van der Waals trimer have been calculated. The wave functions for the low-lying states show very regular behaviour. Above the barrier to linearity, most of the wave functions are irregular but some have simple nodal patterns that suggest localization along periodic orbits. In addition to the "horseshoe" states previously described for $H_3^+$, localized features corresponding to symmetric and antisymmetric stretching vibrations around a linear configuration have been identified. The different localized modes can be combined to form more complex states in a manner analogous to normal modes.

A preliminary study of the rotational states of $Ar_3$ has also been performed. The rotational constants for the low lying states of $Ar_3$ reflect the increasing average size of $Ar_3$ with increasing vibrational excitation. The rotational constants are obtained from two methods, expectation values and energy level differences. The results for the levels above the barrier to isomerisation reveal that the simple models used for obtaining the rotational constants are no longer valid and indicate that a more sophisticated treatment is necessary.

'The underlying physical laws necessary for the mathematical theory of a large part of physics and the whole of chemistry are thus completely known, and the difficulty is only that the exact application of these laws leads to equations much too complicated to be soluble.'

– P. A. M. Dirac, 1929

# Acknowledgments

I would like to begin by thanking my supervisor Jeremy Hutson. His encouragement and guidance have made my PhD both enjoyable and interesting. The various members of the Durham theoretical chemistry group, Keith Atkins, Christine Roche, Robert Bryan, Joanna Howson and Markus Meuwly; have provided a stimulating and friendly environment to work in for which I am very grateful. I extend special thanks to Keith for his guidance during the first year of my PhD. I would also like to acknowledge Lydia Heck's assistance with all matters computational. I have had very valuable correspondence about performing DVR calculations with Hamse Mussa, Rita Prosmiti, Jonathan Tennyson and Prakashan Korambath, all of whom I am very grateful to. My family and friends have provided a lot of support to me during this period and I would like to express my gratitude to them. The EPSRC and the Durham University Chemistry department provided my funding which I gratefully acknowledge. Finally I would like to thank Jo, without whom I might never have made it.

# Statement

No part of this thesis has been previously submitted by me for a degree to any university. Every effort has been made to ensure that all work which is not original to the author has been properly credited. I place no restriction upon access to, or copying of, this thesis.

# CONTENTS

# CHAPTER

## 1

## Introduction

This thesis describes a method of calculating the bound states of triatomic Van der Waals molecules. Before the detailed description of these calculations it would be pertinent to outline the incentives for performing them. The motivations for this work can be broken down into two areas: the study of intermolecular forces and the development of methods for studying large-amplitude motion.

The study of intermolecular forces has far-reaching implications across all fields of science [1]. Crystal structure, reaction kinetics and phase behaviour, for example, cannot be fully understood without an understanding of intermolecular potentials. An increased knowledge of such forces should lead to the development of better models for all such physical phenomena. The eventual aim of such studies must be a description of macroscopic properties from a rigorous microscopic viewpoint.

Analysis of the structure and dynamics of Van der Waals molecules provide a very powerful method of investigating intermolecular forces [2, 3]. A

Van der Waals molecule is a complex formed from two or more chemically stable neutral molecules or atoms. By measuring the spectra of these complexes it is possible to obtain very detailed information about the intermolecular forces holding the cluster together. The weak nature of the intermolecular forces means that the clusters often exhibit large-amplitude motions. This means the spectra contain information about a large region of the potential energy surface and allows information on the anisotropy of the intermolecular forces to be extracted.

In general the intermolecular potential between atoms or molecules is not just the sum of interactions between pairs. The electron distribution of one atom or molecule in a cluster will affect all of the others. For example, it is known that the binding energy of solid argon is overestimated by $\sim 10\%$ if the many-body terms are neglected from the calculation [4]. An understanding of non-additive intermolecular forces is therefore something that is essential for the accurate prediction of a wide variety of condensed phase properties. Van der Waals molecules provide a powerful method of studying such non-additive intermolecular forces [5–8]. Through studying complexes of increasingly higher order each successive many-body term can be extracted uniquely.

To allow the accurate determination of these forces, precise and efficient methods of calculating the spectroscopic properties from potential energy surfaces are needed. By comparison of the calculated spectra with the experimentally measured one it is possible to model the nature of the intermolecular forces present in the system [8].

For a strongly bound molecule the 'traditional' method of predicting a spectrum was to derive an effective Hamiltonian, based upon the normal modes of the molecule, using perturbation theory [9, 10]. Unfortunately for Van der Waals (and other floppy) molecules the traditional approach breaks down. The assumption implicit in the derivation of the effective Hamiltonian, that the molecule only undergoes small amplitude motions, invalidates the approach. A more general way to understand the spectrum is to solve the Schrödinger equation exactly using a global potential energy surface.

The exact solution of the Schrödinger equation is an extremely challeng-

ing task for floppy systems such as Van der Waals molecules. One method of determining the solution of the Schrödinger equation is to represent the wave function as an expansion of basis functions in each degree of freedom and then construct a matrix representation of the Hamiltonian operator. The resulting matrix is then diagonalised (its eigenvalues and eigenvectors determined) to yield the energy levels and the wave functions of the molecule. The size of the matrix involved depends upon the number of energy levels for which the solution is required and upon the number of degrees of freedom in which the motion can be considered 'floppy'. To obtain a solution for all the bound states of the molecule typically about 30 basis functions are needed in each floppy degree of freedom. For a molecule with 2 floppy degrees of freedom the problem is easily solvable with modern computers. For molecules with 3 the problem is much more difficult to solve. The memory requirement, which would be between 1 and 2 gigabytes if the matrix was explicitly constructed, begins to defeat even the largest computers available today. There are two possible solutions to this problem. The first is to wait until a computer that is powerful enough becomes available. The second is to try to develop a novel method of constructing and diagonalising the Hamiltonian matrix that requires less computer power. The work in this thesis is based on the second solution to this problem.

I concentrate in this thesis on the $Ar_3$ Van der Waals trimer. The aim is to develop an efficient method of solving the Schrödinger equation that is extendable to obtain the rotational constants of $Ar_3$. Accurate calculation of these is essential as they provide a rich source of information on the nature of the potential energy surface and hence the intermolecular forces present in the system. Although $Ar_3$ is unlikely to have its spectra measured experimentally because its dipole moment is very small it provides a prototype system to develop such calculations upon. Microwave spectra have been measured for several 'mixed' rare-gas trimers [11, 12], such $Ar_2Ne$, and in principle the method could be used to study them. The method could also be used for highly-excited states of chemically bound molecules as these also undergo large-amplitude motions.

Two particularly attractive systems for the study non-additive intermolec-

ular forces in are $Ar_2HF$ and $Ar_2HCl$ [8]. These are 5-dimensional systems for which $Ar_3$ provides a prototype. The pair potentials for Ar-Ar [13], Ar-HCl [14] and Ar-HF [15] are all known with sufficient accuracy to allow the determination of the three-body forces present in the system by comparison with the extensive spectroscopic data available [16–18]. The problem with these systems is that the dynamical problem is a five-dimensional one which means it is extremely difficult to solve. Although preliminary studies have been performed they were restricted to solving the $J = 0$ problem and obtained rotational constants from expectation values [5]. A method known to be inaccurate. It is hoped that methods developed here could be extended to solve the full $J > 0$ problem for such a system which would enable the accurate determination of the rotational constants.

To solve the Schrödinger equation for floppy molecules such as $Ar_3$, approaches based upon the discrete variable representation (DVR) have often been used [19, 20]. Several of these have been applied to the $H_3^+$ molecular ion [21–23] making it the benchmark for the development of new DVR-based methods. The advantages of using a DVR method are outlined in chapter 2 and the details of my implementation of it for states with $J = 0$ are in chapters 3, 4 and 5. Calculations for states with $J = 1$ and the methods employed for extraction of rotational constants are described in chapter 7.

The wave functions and energy level distribution of a polyatomic molecule reflect the underlying nature of its phase space. At high energies where the classical phase space is chaotic the vibrational wave functions are expected to be irregular. During the course of the studies upon $H_3^+$ several interesting features were observed in the wave functions [24–28]. The wave functions showed regular nodal patterns, and only sampled a portion of the energetically accessible phase space at high energies. One of the aims of the work in this thesis was to see if the same behaviour occurs in $Ar_3$, which has the same equilibrium structure as $H_3^+$, despite the very different energy scales and masses involved. This work is described in chapter 6.

There have been several previous calculations of the bound states of $Ar_3$ using a variety of different methods. Horn *et al.* [29] used vibrational self-consistent-field theory in hyperspherical coordinates to investigate the ef-

fects of non-additive intermolecular forces upon the vibrational energy levels. Horn *et al.* claim that their vibrational levels are converged to 0.01 cm$^{-1}$. However their calculations of degenerate energy levels differ by between 0.3 cm$^{-1}$ and 1.2 cm$^{-1}$. Therefore their calculation is probably subject to a programming error of some kind and does not provide a reliable benchmark. Leitner, Berry and Whitnell [30] performed a DVR calculation in hyperspherical coordinates. They were interested in obtaining the energy level distribution of $Ar_3$ and looking at its low lying vibrational wave functions. There is a problem with this calculation as well. The calculations of degenerate states were again incorrect. This time the discrepancy is much larger; of the order of 7 cm$^{-1}$ in the worse case. Cooper, Jain and Hutson [31] compared a variety of methods based on the normal mode, Jacobi and hyperspherical coordinate systems. This study uncovered the problems with the previous calculations. Its aim was to see which of the methods was extendable to a five-dimensional system and to investigate the effects of non-additive intermolecular forces. The calculations of Cooper *et al.* [31] do not provide a benchmark mostly because of the limitations of the methods used and the computer power available at the time.

Two calculations that do provide some possibility for comparison are those of Bryan [32], who used the hyperspherical method of Cooper *et al.* [31] to calculate the lowest 10 vibrational states of $Ar_3$, and the ground state rotational constant calculation of Ernesti and Hutson [7]. Where appropriate comparisons with these two calculations have been made.

CHAPTER

## 2

# Bound state calculations on Van der Waals dimers

The aim of this chapter is to examine the methods available to calculate the bound states of Van der Waals dimers and to investigate their suitability for calculations on Van der Waals trimers. There have been many calculations of the bound states of Van der Waals molecules (and floppy molecules in general) using a variety of different methods in different coordinate systems [5, 19, 24, 29, 33]. To investigate each possible approach in detail would be very time consuming and a little futile if a method could be ruled out from the start. Most methods have three distinct areas in which they can differ: the choice of coordinate system, the method for obtaining the eigenvalues of the Schrödinger equation and the choice of basis functions.

By performing calculations on the $ArCO_2$ Van der Waals molecule, a molecule with only two floppy degrees of freedom, I can identify any weaknesses in the chosen method of calculation that would prevent its extension to a

molecule with three degrees of freedom.

## 2.1  Coordinate Systems

All of the calculations in this thesis have been carried out using a Jacobi co-ordinate system in a body-fixed frame of reference. I will briefly outline the reasons for this choice:

The choice of body-fixed coordinates as opposed to space-fixed ones was quite straightforward. The main advantage is that the vibrational and rotational coordinates, and the Coriolis coupling terms between them, are easily identified, making the resulting equations much simpler than those in the space-fixed frame. Most current methods for calculating bound states of floppy molecules uses a body-fixed frame.

The choice of Jacobi coordinates was a little less clear-cut. There have been several coordinate systems used in rovibrational calculations on floppy molecules. The choice of good coordinates depends very much on the particular molecule considered: there is no coordinate system that is satisfactory for all molecules. Several criteria should be fulfilled by a good coordinate system:

- It must span all the configuration space of interest. i.e. All conformers that the molecule is able to adopt including states where it is rotating ($J > 0$) must be able to be described by the coordinate system.

- It should be able to take advantage of the highest symmetry present in the system. This makes the resulting Hamiltonian matrix as small as possible.

- The coordinates should be orthogonal. This minimises the number of cross terms in the kinetic energy operator, making the Hamiltonian matrix elements simpler to evaluate.

- The coordinates should minimise the interaction between different modes, i.e., make the Hamiltonian as separable as possible.

For the best possible description of a particular molecule all these criteria should be fulfilled however in practice this is not always possible.

There are four coordinate systems commonly used to describe floppy molecules:

- Jacobi coordinates. For a molecule ABC $r$ is the length of the 'diatom' BC bond, $R$ is the distance from A to the centre of mass of BC and $\theta$ is the angle between $r$ and $R$.

- Hyperspherical coordinates [34]. These consist of a hyper-radius $\rho$ that describes the size of the system, and two hyper-angles $\theta$ and $\chi$ that describe its shape.

- Internal (or bond) coordinates [35]. $R_1$ and $R_2$ are the distances from the central atom to the other two atoms. $\theta$ is the angle between them.

- Radau coordinates [36]. These can be loosely thought of as an orthogonal version of internal coordinates. Here $R_1$ and $R_2$ describe the distance from the two lighter atoms to the canonical point which for a light-heavy-light system such as $H_2O$ lies very close to the O atom.

Internal coordinates are designed for strongly bound molecules and are not usually orthogonal. Radau coordinates are designed for light-heavy-light systems (e.g. $H_2O$) and the motions within them make it difficult for them to describe Van der Waals molecules such as $ArCO_2$. (They contravene the last criterion.) The major difference between Jacobi and hyperspherical coordinate systems is that hyperspherical coordinates allow the use of full $D_{3h}$ symmetry. In Jacobi coordinates it is very difficult to take account of symmetries higher than $C_{2v}$. There are two major problems with hyperspherical coordinates: the basis sets used have very poor convergence properties and $J > 0$ calculations are extremely difficult because of the complexity of the equations involved. I will therefore use Jacobi coordinates as they provide the most natural description of the motions within a Van der Waals dimer. Their only failing is an inability to handle higher than twofold symmetry.

## 2.2   Solving the Schrödinger equation

Rotation-vibration energy levels of polyatomic molecules can be calculated accurately by methods which fall into two basic categories. The first of these uses an $L^2$ basis set representation for all the internal degrees of freedom. The second relies on scattering theory, identifying one coordinate $R$ as the scattering coordinate, and expanding the remaining degrees of freedom in a $L^2$ basis. As I use the first method for all the calculations in this thesis I will first briefly outline the second method and the reasons for not using it in the present work.

### 2.2.1   Coupled Channel method

This method is related to those used in molecular scattering theory. One coordinate, in this example $R$, is identified as the scattering coordinate and all the others are expanded in a basis set. The Schrödinger equation can then be written as a set of coupled differential equations in $R$, which are then solved using standard scattering theory techniques. For the systems under consideration the $J = 0$ Hamiltonian can be written as:

$$H = -\frac{\hbar^2}{2\mu_1 R^2}\frac{\partial}{\partial R}\left(R^2\frac{\partial}{\partial R}\right) + F(R, X) \tag{2.1}$$

where $F(R, X)$ represents all the other terms in the Hamiltonian except for the partial derivative in $R$, and $X$ stands for all the other coordinates. I want to find the bound state solutions of the Schrödinger equation

$$(H - E_n)\Psi_n = 0 \tag{2.2}$$

The wave function $\Psi_n$ is expanded as

$$\Psi_n(R, X) = R^{-1}\sum_i g_i^n(R)\Phi_i(X) \tag{2.3}$$

The functions $\Phi_i(X)$ represent a basis set for all the degrees of freedom except $R$, labeled by the collective index $i$. Substitution of Eq. 2.3 into Eq. 2.2, premultiplication by $\Phi_i^*(X)$ and integration over $X$ leads to the standard set of coupled equations. These are written in matrix form as:

$$\left[-\frac{\hbar^2}{2\mu_1}\frac{\partial^2}{\partial R^2}\mathbf{I} + \mathbf{W}(R) - E_n\mathbf{I}\right]\mathbf{g}(R) = 0 \tag{2.4}$$

Here I is the identity matrix and

$$[\mathbf{W}(R)]_{i'i} = \int \Phi_{i'}^{*}(X) F(R, X) \Phi_{i}(X) dX \qquad (2.5)$$

These coupled channel equations can be integrated numerically by a number of methods [37, 38]. The boundary conditions for the problem are that $g(R) \sim 0$ for $R \to 0$ and $R \to \infty$. The trial eigenvalue, $E_n$, is usually varied until the two solutions satisfying the boundary conditions match at some intermediate value of $R$, defining $E_n$ and $\Phi_n$. For the $J > 0$ case the equations are a little more complicated, but the methods for solving them remain the same.

The coupled channel method has only been used so far for a few systems where it is known to be highly accurate and numerically very stable. However it is likely to be computationally expensive when treating highly excited vibrational states or large amplitude motions with several degrees of freedom. The $L^2$ basis functions used to describe the 'remaining' degrees of freedom should be free rotor functions of the monomeric fragment. (i.e. They should diagonalise the monomer Hamiltonian.) For rigid monomers such as $CO_2$ such a representation is very compact. However for systems where the $r$ coordinate is also floppy, such as $Ar_3$, a large number of free rotor functions would be needed making the size of the matrix that needed to be propagated prohibitively large. This is the primary motivation for rejection of this method in the present study.

## 2.2.2  $L^2$ methods

The variational method for calculating the bound states by expanding each internal degree of freedom in a basis set of orthonormal $L^2$ functions is known as the Finite Basis Representation (FBR) because a finite expansion of basis functions is used to represent the wave function. I will now outline the basic principles of a FBR calculation and some of the pitfalls involved. Historically these led to the development of a pointwise representation method, the discrete variable representation (DVR).

## Finite Basis Representation (FBR)

For a one-dimensional system the Schrödinger equation is:

$$\hat{H}\psi = E\psi \tag{2.6}$$

in which:

$$\hat{H} = \frac{-\hbar^2}{2\mu}\frac{\partial^2}{\partial x^2} + V(x) \tag{2.7}$$

This equation is solved by representing the wave function by a basis set expansion. These basis sets are usually (but not always) made up of orthogonal polynomials, e.g. for the one-dimensional problem:

$$\psi = \sum_i^n c_i W_i^{1/2} P_i(x) \tag{2.8}$$

where $W_i$ is a weighting function, $P_i(x)$ is an orthogonal polynomial and $c_i$ is its coefficient. Then the equation is multiplied from the left by $\psi^*$ and integrated over all coordinate space to give a set of algebraic equations:

$$\sum_{j=1}^M \langle \psi_i | H - E | \psi_j \rangle c_i = 0 \text{ for } i = 1, \ldots, M \tag{2.9}$$

which are solved by matrix diagonalisation to yield the required eigenvalues and eigenfunctions. The number of basis functions, $n$, would then be increased systematically until the calculation converges. However the size of the final Hamiltonian matrix, which has to be diagonalised, also increases with $n$. There is therefore a limit, due to the restrictions imparted by the computing, on $n$. (The computation time for matrix diagonalisation scales as $n^3$ and the storage requirement scales as $n^2$.) For systems which exhibit low-amplitude motions, with their wave functions localised in a small region of space, this is not that much of a problem because only relatively small values of $n$ are required to represent the wave function accurately. For systems which exhibit large-amplitude motion, weakly bound or highly excited states for example, the value of $n$ required is much larger because many more basis functions are needed to represent the delocalised wave function, if such a representation is possible at all.

Another problem occurs with the potential term $V(x)$. This has to be integrated over the coordinate space to obtain the FBR matrix elements. For very

simple systems this integral can be done analytically but if the potential func-
tion is complicated this integration must be done numerically, introducing a
possible source of inaccuracy into the calculation. One method commonly
used for hindered rotor problems is to expand the potential as a sum of Leg-
endre polynomials, which enables the integration to be done analytically, but
this is not necessary a compact representation. These considerations lead to
the development of a different approach, one in which these problems could
be addressed.

### Discrete Variable Representation (DVR)

The DVR method was first outlined by Harris *et al.* [39] and was shown by
Dickinson and Certain [40] to have useful equivalences to Gaussian quadra-
ture approximations. Work in this area has taken a sudden upsurge after a
series of studies by Light and co-workers. (For more details see the review by
Bačić and Light [19].)

The basic philosophy of a DVR is to use a pointwise representation of the
wave function rather than a basis function one. This enables the method
to be tailored to the properties of the potential energy surface of the system
under consideration. For example regions which are physically inaccessible
can be removed from the calculation. The theory of the DVR is closely tied in
with that of Gaussian quadrature.

Given an FBR two statements are required to define a DVR. Firstly the DVR
is defined as an orthogonal transformation from an FBR, which means the
two representations are formally isomorphic. The basis functions in a DVR
representation are just linear combinations of those used in an FBR.

Consider the evaluation of an arbitrary one-dimensional operator $\hat{D}$ in a
DVR $|\eta\rangle$ and an FBR representation $|i\rangle$:

$$
\begin{aligned}
{}^{DVR}D_{\eta\eta'} &= \langle\eta'|\hat{D}|\eta\rangle = \sum_{i,i'}^{n} \langle\eta|i\rangle\langle i|\hat{D}|i'\rangle\langle i'|\eta'\rangle \\
&= \sum_{i,i'}^{n} T_{i\eta}\,{}^{FBR}D_{i,i'}\,T_{i',\eta'}
\end{aligned}
\tag{2.10}
$$

in this equation the matrix $T$ defines the transformation between the FBR
and the DVR. The basis functions of the DVR representation are related to

those of the FBR by the **T** matrix:

$$\langle x|\eta\rangle = \sum_{i=1}^{n}\langle x|i\rangle\langle i|\eta\rangle$$

$$= \sum_{i=1}^{n}\phi_i(x)\mathbf{T}_{i,\eta} \tag{2.11}$$

In the DVR, coordinate functions (e.g. $V(x)$) are approximated by their values at the DVR points. This is equivalent to evaluation of these matrix elements in the FBR by $n$-point Gaussian quadrature, providing the FBR basis functions are orthogonal polynomials in $x$ times the square root of their weight function, i.e. they obey the orthogonality relation:

$$\int \phi_i(x)\phi_{i'}(x)\,dx = \delta_{i,i'} \tag{2.12}$$

where $\phi_i(x) = f_i(x)W(x)^{1/2}$. $f_i(x)$ is an orthonormalised polynomial in $x$ and $W(x)$ is its weight function. The transformation matrix **T** is defined as:

$$\mathbf{T}_{i\eta} = \omega_\eta^{1/2}\phi_i(x_\eta) \tag{2.13}$$

where the $x_\eta$ are the Gaussian quadrature points and the $\omega_\eta$ are the corresponding weights at that quadrature point.

Secondly a quadrature approximation is made to the potential matrix elements in a DVR. The assumption that a function is diagonal in the DVR is equivalent to the Gaussian quadrature evaluation of the FBR matrix elements:

$$^{\text{FBR}}V_{i,i'} \approx \sum_{\eta}\omega_\eta\phi_i(x_\eta)V(x_\eta)\phi_{i'}(x_\eta)$$

$$= \sum_{\eta}\mathbf{T}_{i\eta}\cdot V(x_\eta)\cdot\mathbf{T}_{i'\eta}$$

$$= [\mathbf{T}^T\cdot{}^{\text{DVR}}\mathbf{V}\cdot\mathbf{T}]_{ii'} \tag{2.14}$$

One advantage of using a DVR method is that the matrix of the potential energy operator, $\hat{V}$, is diagonal. No multi-dimensional integrals over basis functions are required. Another advantage is the sparsity of the Hamiltonian matrix (the small number of elements which are non-zero). This has often been exploited in the diagonalisation procedure (see chapter 3).

Having defined a DVR for a one-dimensional system, I will now outline its use in calculating the bound states of Van der Waals molecules after an explanation of the potential-optimised method of obtaining basis functions.

## 2.3  Potential-Optimised Basis Functions

To use functions that are optimised with respect to a cut through a potential energy surface as a basis set is not a particularly new idea (for example see the secular equation method described by Le Roy and Carley [41]) but it was first applied in the context of a DVR calculation by Echave and Clary [42].

The basic idea behind the procedure is to use the solutions of a one-dimensional reference Hamiltonian as basis functions. Of course nearly all basis functions are solutions of some model problem (e.g. the hydrogen atom, the Morse oscillator); the difference in this case is the definition of the model problem.

Firstly the one dimensional reference Hamiltonian $^{1D}\hat{H}^x_{\text{ref}}$ is defined:

$$^{1D}\hat{H}^x_{\text{ref}} = -\frac{\hbar^2}{2\mu}\frac{\partial^2}{\partial x^2} + V^x_b(x) \tag{2.15}$$

where $V^x_b(x)$ is the basis-generating potential. The Schrödinger equation (Eq. 2.15) is then solved, either by numerical integration or by expansion of the wave function by a basis set (in a FBR or DVR representation), to obtain a set of potential optimised functions:

$$\psi^{\text{PO}}_i, i = 1, 2, \ldots, N^{\text{PO}} \tag{2.16}$$

In an FBR calculation these functions are then used as basis functions. To obtain a DVR representation of these functions a matrix of the coordinate operator, $x$, in the $\psi^{\text{PO}}(x)$ basis is diagonalised. The resulting eigenvalues correspond to the potential-optimised DVR quadrature points and the matrix of eigenvectors to the DVR-FBR transformation matrix. (The method of obtaining the DVR quadrature points via coordinate operator diagonalisation is known as the HEG method after Harris, Engerholm and Gwinn [39].) The resulting DVR quadrature points are not of Gaussian accuracy because the potential-optimised functions are not a simple polynomial function of $x$. It is known however that the quadrature approximation is very good one [42].

The potential $V^x_b(x)$ will have $N$ bound states. The HEG method produces one quadrature point for each eigenfunction and therefore there is theoretical upper limit on $N^{\text{PO}}$ of $N$. One way of avoiding this problem is to place an infinite potential wall at $R_{\text{max}}$. Then as many functions can be generated as

are required. Obviously a careful choice of the value of $R_{\mathrm{max}}$ must be made. If it is too small a region of the potential energy surface that the molecule samples will be removed from the calculation making it unphysical. If it is too large quadrature points will be placed at unnecessarily large values of $R$ which would be wasteful. The value of $R_{\mathrm{max}}$ can be determined quite straightforwardly from a plot of the potential.

In principle the potential-optimisation procedure could be used to generate basis functions for the radial or the angular degrees of freedom. In this thesis however I have only applied it to the radial degrees of freedom. The mixed nature of the angular kinetic energy operator (which is a function of $R$ as well as $\theta$) makes the procedure rather more difficult to implement.

The quality of the potential-optimised functions that are obtained is dependent upon the choice of the basis generating potential $V_b^x(x)$. This should be a cut through the potential energy surface that takes into account all the regions of configuration space that the molecule can sample. A judicious choice of cut should enable the number $N^{\mathrm{PO}}$ to be a lot smaller than the number of non-potential-optimised functions needed to converge the same calculation.

## 2.4   Calculating the bound states of $ArCO_2$

### 2.4.1   The Hamiltonian operator

A Jacobi co-ordinate system is used (See Fig. 2.1): $R$ is defined as the vector between the centre of mass of B-C and A, $r$ is defined as the B-C bond vector and $\theta$ is defined as the angle between them. Of course for the molecule studied in this chapter the 'diatomic fragment' B-C is in fact triatomic. This makes no practical difference to these calculations however as the length of $r$ is fixed.
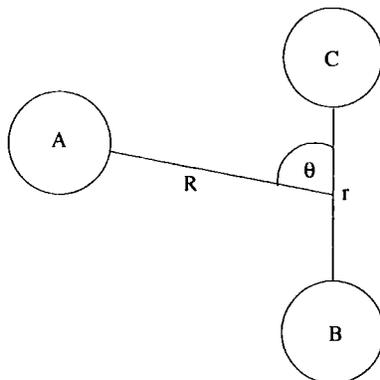
**Figure 2.1:** Jacobi Coordinate System

In this co-ordinate system the Hamiltonian operator has the form [43]

$$
\begin{aligned}
\hat{H}(R,r,\theta) \; = \; & -\frac{\hbar^2}{2\mu_1}\frac{\partial^2}{\partial R^2} - \frac{\hbar^2}{2\mu_2}\frac{\partial^2}{\partial r^2} \\
& + \frac{\hbar^2}{2}\left(\frac{1}{\mu_1 R^2} + \frac{1}{\mu_2 r^2}\right)\left(\frac{-1}{\sin\theta}\frac{\partial}{\partial\theta}\sin\theta\frac{\partial}{\partial\theta}\right) \\
& + \frac{\hbar^2}{2\mu_1 R^2}[J(J+1) - 2K^2] \\
& + \frac{\hbar^2}{2\mu_1 R^2}[J(J+1) + K(K\pm 1)]^{1/2}[j(j+1) - K(K\pm 1)]^{1/2}\delta_{KK\pm 1} \\
& + V(R,r,\theta) \qquad\qquad\qquad\qquad\qquad\qquad\qquad\qquad\qquad (2.17)
\end{aligned}
$$

where:

$$
\mu_1 = \frac{m_A(m_B + m_C)}{m_A + m_B + m_C} \qquad \mu_2 = \frac{m_B + m_C}{m_B m_C} \qquad\qquad (2.18)
$$

For $ArCO_2$ the reduced masses are:

$$
\mu_1 = \frac{m_{Ar}(m_C + 2m_O)}{m_{Ar} + m_C + 2m_O} \qquad \mu_2 = \frac{2m_O + m_C}{2m_O m_C} \qquad\qquad (2.19)
$$

The first three terms are the radial (in $R$ and $r$) and bending kinetic-energy operators, the fourth is the total angular momentum operator, the fifth is the Coriolis coupling term and the final term is the potential energy. As is often the case the simplest looking term, the potential energy, is the one which defines the properties of the system. This version of the Hamiltonian operator corresponds to the projection of the total angular momentum $J$, which is labeled $K$, being along the $R$ axis. In some circumstances it is advantageous
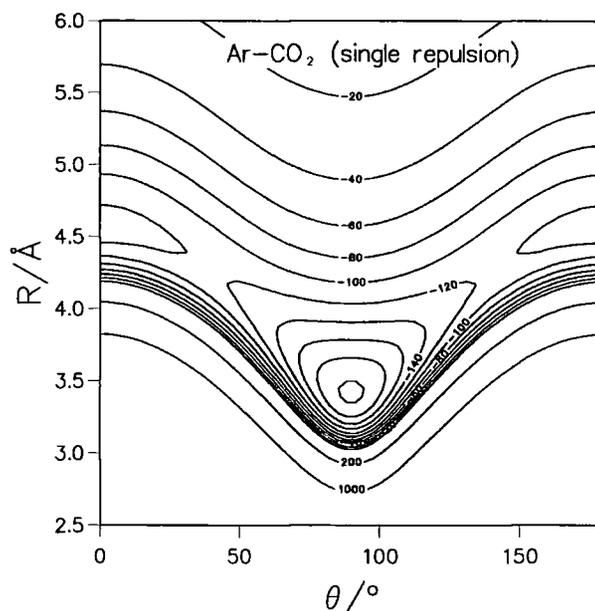
**Figure 2.2:** The 'single repulsion' $ArCO_2$ surface of Hutson *et al.* [45].

to have the projection along the $r$ axis instead. The Hamiltonian operator in this case has the $\mu_1 R^2$ in the fourth and fifth replaced by $\mu_2 r^2$.

In this section I loosely follow the prescription of Choi and Light who performed a DVR calculation on ArHCl [44] and adapt it slightly. The potential energy surface used to describe the interaction between the Ar atom and the $CO_2$ molecule is the 'single repulsion' surface of Hutson *et al.* [45]. It has a well depth of $204.16$ $cm^{-1}$ at the minimum with a T-shaped equilibrium geometry ($\theta=90°$) and Van der Waals bond length (value of $R$) of $3.416$ Å. A contour plot of the potential is shown in figure 2.2.

For $ArCO_2$ the $r$ coordinate is not a 'floppy' one which affects the terms in the Hamiltonian operator (Eq. 2.17) dependent upon it. The vibrational frequency of $CO_2$ is two orders of magnitude greater than its rotational constant and nearly five orders of magnitude larger than the rotational constant of $ArCO_2$. Therefore the effect of the vibrational (i.e. $r$) motion on the Van der Waals stretching (i.e. $R$) and bending (i.e. $\theta$) motions is small. These considerations allow $r$ to be fixed at its expectation value in the vibrational state of the $CO_2$ monomer of interest. The radial kinetic energy operator ($\frac{\partial^2}{\partial r^2}$) is therefore zero and the $\frac{1}{\mu_2 r^2}$ part of the angular kinetic energy operator can be

replaced by the rotational constant of the monomer $b_v$. In this work the rotational constant of $CO_2$ is taken to be 0.39021894 cm$^{-1}$ and the reduced mass of the complex $\mu_1$ is taken to be 20.939751 u.

## 2.4.2  Basis Functions

The $n$th wave function of the system with total angular momentum $J$ and parity denoted by $p$ is expanded as a linear combination of products of orthogonal functions of $R$ [$\phi_i^R(R)$], associated Legendre polynomials [$P_j^K(\cos\theta)$] and parity-adapted rotation functions [ $C_{MK}^{Jp}(\xi, \rho, \eta)$ ] [46]. The wave function is expressed thus

$$\Psi_n^{Jp}(R, \theta, \xi, \rho, \eta) = \sum_{i,j,K} c_{ijK}^{nJp} \phi_i^R(R) P_j^K(\cos\theta) C_{MK}^{Jp}(\xi, \rho, \eta) \tag{2.20}$$

The basis functions are now discussed in more detail:

**Basis functions in $R$**

In the original work of Choi and Light [44] a basis of orthogonalised Sturmian functions was used in the $R$ coordinate. In this work I have investigated two different ways of constructing a basis in $R$, to see which has the best convergence properties.

*Sturmian vibrational functions* [$S_i^{(l)}(R)$]

These are the basis functions used by Choi and Light [44] in the $R$ coordinate [47]. They have the form:

$$S_i^{(l)}(R) = \sqrt{\frac{(i-l-1)!}{(i+l)!}} e^{-R/2} R^{l+1/2} L_{i-l-1}^{2l+1}(R) \tag{2.21}$$

(where $L_{i-l-1}^{2l+1}(R)$ is a Laguerre polynomial) they are orthonormal over the range $R = 0 \rightarrow \infty$ and have the desired boundary conditions of approaching zero at the origin and at infinity.

In this basis the kinetic energy matrix is obtained from the following expression:

$$\mathbf{D}_{ii'}^R = \langle S_{i'}^{(l)} | \frac{-\hbar^2}{2\mu_1} \frac{\partial^2}{\partial R^2} | S_i^{(l)} \rangle$$

$$= \frac{\hbar^2}{2\mu_1}\left[(i - l(l+1) - 3/4)\langle S_{i'}^{(l)}|\frac{1}{R^2}|S_i^{(l)}\rangle + (i - 1/2)\langle S_{i'}^{(l)}|\frac{1}{R}|S_i^{(l)}\rangle\right.$$
$$\left. - \frac{1}{4}\delta_{i'i} - \sqrt{i(i-1) - l(l+1)}\langle S_{i'}^{(l)}|\frac{1}{R^2}|S_{i-1}^{(l)}\rangle\right] \tag{2.22}$$

*Potential-optimised functions* $[\phi_i^R(R)]$

To generate the potential-optimised functions for the $R$ coordinate, solutions of a one-dimensional reference Hamiltonian, $^{1D}\hat{H}_{\text{ref}}^R$, are calculated. For $ArCO_2$, $^{1D}\hat{H}_{\text{ref}}^R$ is taken to be

$$^{1D}\hat{H}_{\text{ref}}^R = -\frac{\hbar^2}{2\mu_1}\frac{\partial^2}{\partial R^2} + V_{\text{cut}}^R(R) \tag{2.23}$$

and $V_{\text{cut}}^R(R)$ is obtained by holding $\theta$ at a constant value (90°). The one dimensional Hamiltonian is then solved numerically using the SCHRQ [48] subroutine. The cut through the potential and the functions derived from it are shown in figure 2.3.

The kinetic energy matrix in this basis is obtained from the following expression:

$$\begin{aligned}\mathbf{D}_{ii'}^R &= \langle\phi_{i'}^R|\frac{-\hbar^2}{2\mu_1}\frac{\partial^2}{\partial R^2}|\phi_i^R\rangle \\ &= \langle\phi_{i'}^R|E_i|\phi_i^R\rangle - \langle\phi_{i'}^R|V_{\text{cut}}^R|\phi_i^R\rangle\end{aligned} \tag{2.24}$$

in which $E_i$ is the $i$'th eigenvalue of the one-dimensional Hamiltonian.

## 2.4.3 Associated Legendre polynomials $[P_j^K(\cos\theta)]$

These are used as the basis functions in $\theta$. They are orthonormal in the range $\theta = 0 \to \pi$ and are defined as the solution of Legendre's differential equation. They occur in many problems involving rotational motion in spherical polar coordinate systems as they form part of the eigenfunctions for such motion which are known as the spherical harmonics [49, 50].

## 2.4.4 Rotation functions $[C_{MK}^{Jp}(\xi, \rho, \eta)]$

These are functions of the Euler angles, $(\xi, \rho, \eta)$. These define the relationship between the body fixed coordinate system which rotates with the system and the space fixed one [49]. The rotation functions used are formed by
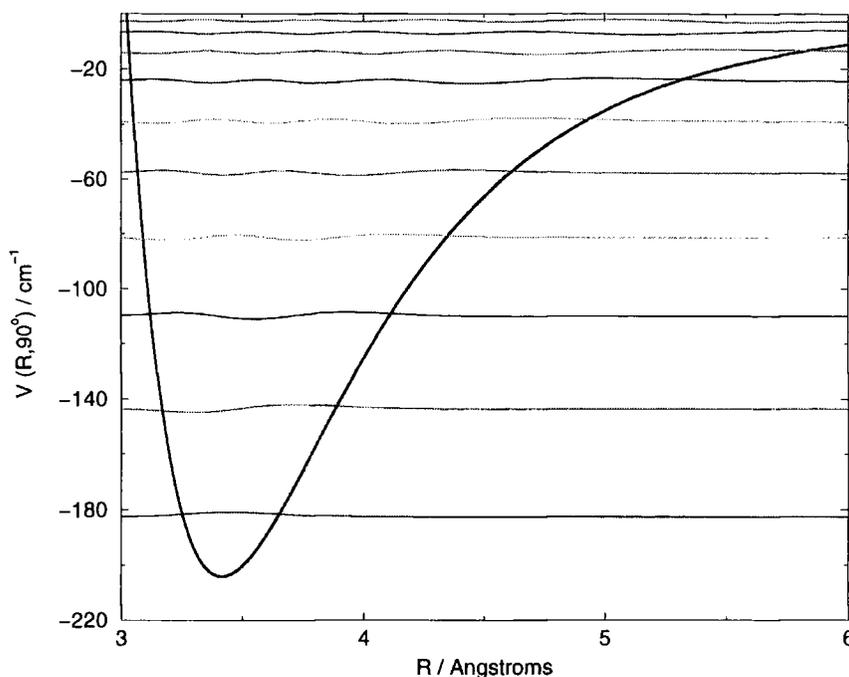
**Figure 2.3:** The cut through the $ArCO_2$ potential at $\theta=90°$ and some of the potential-optimised basis functions derived from it.

combining normalised Wigner rotation functions $[D^{Jp}_{M\pm K}]$ to be orthonormal parity-adjusted eigenfunctions:

$$\int\limits_0^{2\pi}\int\limits_0^{\pi}\int\limits_0^{2\pi} C^{J'p'*}_{M'K'} C^{Jp}_{MK} d\tau = \delta_{JJ'}\delta_{pp'}\delta_{MM'}\delta_{KK'} \tag{2.25}$$

in which

$$C^{Jp}_{MK} = [2(1+\delta_{K0})]^{-1/2}[D^J_{MK} + (-1)^{J+K+p}D^J_{M-K}] \tag{2.26}$$

and

$$\int\limits_0^{2\pi}\int\limits_0^{\pi}\int\limits_0^{2\pi} D^{J'*}_{M'K'} D^J_{MK} d\tau = \delta_{KK'} \tag{2.27}$$

in these equations $d\tau$ denotes the volume element of the Euler angles. As with the $D^J_{MK}$ the $C^{Jp}_{MK}$ are eigenfunctions of the $\hat{J}^2$ and $\hat{J}^2_Z$ operators. However the $C^{Jp}_{MK}$ are also orthonormal eigenfunctions of the parity operator $\hat{p}$. As parity is a rigorously good quantum number it is usually advantageous to choose basis functions that have definite parity as this allows solutions which have different parities to be calculated separately.

## 2.5 Calculating Hamiltonian matrix elements

When doing a DVR calculation its usual to define the isomorphic FBR first:

$$
\begin{aligned}
\mathbf{H}_{ijK'}^{i'j'K'} &= \langle C_{MK'}^{Jp} P_{j'}^{K} S_{i'}^{(l)} | \hat{H} | S_i^{(l)} P_j^K C_{MK}^{Jp} \rangle \\
&= \mathbf{D}_{ii'}^{R} \delta_{j'j} \delta_{K'K} + f_{i'i}^{R} \mathbf{D}_{ii'}^{\theta K} \delta_{K'K} - g_{i'i}^{R}[J(J+1) - 2K^2]\delta_{j'j}\delta_{K'K} \\
&\quad - g_{i'i}^{R}(1+\delta_{K0})^{1/2} \Lambda_{JK}^{+} \Lambda_{JK}^{+} \delta_{j'j} \delta_{K'K+1} \\
&\quad - g_{i'i}^{R}(1+\delta_{K'0})^{1/2} \Lambda_{JK}^{-} \Lambda_{jK}^{-} \delta_{j'j} \delta_{K'K-1} + V_{ij}^{i'j'K} \delta_{K'K}
\end{aligned}
\tag{2.28}
$$

in which:

$$
\mathbf{D}_{j'j}^{\theta K} = \langle P_{j'}^K | \hat{\mathbf{D}}^{\theta \hat{J}_z} | P_j^K \rangle = j(j+1)\delta_{j'j}
\tag{2.29}
$$

$$
V_{ij}^{i'j'K} = \langle P_{j'}^K S_{i'}^{(l)} | V(R,\theta) | S_i^{(l)} P_j^K \rangle
\tag{2.30}
$$

$$
f_{i'i}^{R} = \langle S_{i'}^{(l)} | \left( \frac{1}{\mu_1 R^2} + b_v \right) | S_i^{(l)} \rangle
\tag{2.31}
$$

$$
g_{i'i}^{R} = \frac{\hbar^2}{2\mu_1} \langle S_{i'}^{(l)} | \left( \frac{1}{R^2} \right) | S_i^{(l)} \rangle
\tag{2.32}
$$

$$
\Lambda_{JK}^{\pm} = \sqrt{J(J+1) - K(K \pm 1)}
\tag{2.33}
$$

Only the $\mathbf{D}_{ii'}^{R}$ and $\mathbf{D}_{j'j}^{\theta}$ matrices are evaluated in the FBR. They are then transformed to the DVR via an orthogonal transformation. All other matrix elements are evaluated directly in the DVR. In the above equations $S_i^{(l)}$ is used to represent the basis functions in $R$. The equations for the potential-optimised basis are obtained by replacing $S_i^{(l)}$ with $\phi_i^R$.

The FBR Hamiltonian is transformed via the **T** matrices to a DVR representation:

$$
\begin{aligned}
{}^{\text{DVR}}\mathbf{H}_{\alpha\beta K}^{\alpha'\beta'K'} &= \sum_{i'i} \sum_{j'j} {}^{K\theta}T_{j'\beta'} {}^{R}T_{i'\alpha'} {}^{\text{FBR}}H_{ijK}^{i'j'K'} {}^{K\theta}T_{j\beta} {}^{R}T_{i\alpha} \\
&= {}^{R}d_{\alpha'\alpha}\delta_{\beta'\beta}\delta_{K'K} + \frac{\hbar^2}{2}\left( \frac{1}{\mu_1 R_\alpha^2} + b_v \right) {}^{\theta K}d_{\beta'\beta}\delta_{\alpha'\alpha}\delta_{K'K} \\
&\quad + \frac{\hbar^2}{2\mu R_\alpha^2}[\{J(J+1) - 2K^2\}\delta_{\alpha'\alpha}\delta_{\beta'\beta}\delta_{K'K} \\
&\quad - \{1+\delta_{K0}\}^{1/2}\Lambda_{JK}^{+}B_{\beta'\beta}^{+}\delta_{\alpha'\alpha}\delta_{K'K+1} \\
&\quad - \{1+\delta_{K'0}\}^{1/2}\Lambda_{JK}^{-}B_{\beta'\beta}^{-}\delta_{\alpha'\alpha}\delta_{K'K-1}] + V_{\alpha\beta}^{\alpha'\beta'}\delta_{K'K}
\end{aligned}
\tag{2.34}
$$

$$^{R}d_{\alpha'\alpha} = \sum_{i'i} {}^{R}T_{i'\alpha'}\, {}^{R}D_{i'i}\, {}^{R}T_{i\alpha} \tag{2.35}$$

$$^{K\theta}d_{\beta\beta'} = \sum_{K}^{j_{max}} {}^{K\theta}T_{j\beta'}\, {}^{K\theta}D_{jj}\, {}^{K\theta}T_{j\beta} \tag{2.36}$$

$$B_{\beta\beta'}^{\pm} = \sum_{j=K}^{j_{max}} {}^{K\theta}T_{j\beta'}\Lambda_{jK}^{\pm}\, {}^{K\theta}T_{j\beta} \tag{2.37}$$

The potential energy is now approximated as diagonal in the DVR:

$$V_{\alpha\beta}^{\alpha'\beta'} = V(R_{\alpha}, \theta_{K\beta})\delta_{\alpha'\alpha}\delta_{\beta'\beta} \tag{2.38}$$

as mentioned above, this approximation is the same as evaluating the FBR matrix elements by an $n$-point Gaussian quadrature and then transforming to a DVR representation. The transformation matrices $T$ are labeled by superscripts $R$, $r$ and $K\theta$ to indicate the coordinate that they refer to. Greek suffixes refer to DVR points and Roman suffixes to FBR functions.

## 2.5.1 Successive diagonalisation and truncation

This method involves breaking down the diagonalisation of the full DVR Hamiltonian matrix into a series of lower dimensional problems. Each diagonalisation of the lower dimensional Hamiltonians is followed by a transformation of the successively higher dimensional Hamiltonians of the DVR to a truncated representation in the eigenvectors of the lower dimension. The idea is to make the size of the final Hamiltonian matrix as small as possible to enable the most efficient solution of the given problem.

Here I present the method for diagonalising with respect to the $R$ coordinate first, though it is also possible to diagonalise first with respect to $\theta$.

Firstly the one-dimensional Hamiltonian is constructed from the transformed $\mathbf{D_R}$ and the potential energy:

$$\begin{aligned} ^{1D}H_{\alpha\beta K}^{\alpha'\beta'K'} &= {}^{R}d_{\alpha\alpha'} + V_{\alpha\beta} \cdot \delta_{\alpha\alpha'}\delta_{\beta\beta'}\delta_{KK'} \\ &\equiv {}^{1D}h_{\alpha\alpha'}\delta_{\beta\beta'}\delta_{KK'} \end{aligned} \tag{2.39}$$

each $^{1D}h_{\alpha\alpha'}$ corresponds to one matrix element in the 1D Hamiltonian matrix in a specified $(\beta, K)$ diagonal block of the $^{3D}\mathbf{H}$ matrix. Each pair of $(\beta, K)$

defines the values for the angle $\theta_{\beta K}$, corresponding to the $\beta$th DVR quadrature point in the $P_j^K$ basis set, and $K$ for the projection of $J$ onto the body-fixed axis.

The $^{1D}h$ matrix is then diagonalised to give

$$^{1D}h^{(\beta K)} = {}^{1D}C^{\beta K} \cdot {}^{1D}E^{\beta K} \cdot [{}^{1D}C^{\beta K}]^T \tag{2.40}$$

$^{1D}E^{\beta K}$ is a diagonal matrix containing the eigenvalues of the one dimensional Hamiltonian and $^{1D}C^{\beta K}$ are the corresponding eigenvectors. This basis is then truncated using an energy cutoff condition:

$$^{1D}E_l^{\beta K} \leq E_{\text{cut}}^{1D} \tag{2.41}$$

This energy value $E_{\text{cut}}^{1D}$ can be varied depending on the system being studied and the accuracy of the highest energy eigenvalue required from the calculation. Another method would be to truncate a constant number of eigenvectors for each $^{1D}h$ diagonalised. This is not so effective in reducing the size of the final Hamiltonian matrix to be diagonalised especially if there is a large variation in the potential with $\theta$. (However it is used in the parallel implementation of the SDT algorithm as it ensures the load is evenly distributed across the processors [51].) The truncated $^{1D}C$ matrix is a $N_R \times M_{\beta K}$ rectangular matrix which is denoted $^{1D}\bar{C}$. $M_{\beta K}$ is the number of 1D eigenvectors that satisfy the energy cutoff condition in each $(\beta, K)$ block.

Part A of Fig.1 shows the structure of the DVR Hamiltonian matrix before any truncations. (The individual DVR matrix elements are labeled by the quadrature points they refer to as opposed to an FBR matrix which would be labeled with respect to basis functions.) Part B shows the matrix after the first truncation. The matrix has been transformed to the 1D-eigenvector basis, the 1D-Hamiltonians are all different sizes having been truncated using the energy cut-off condition. Part C shows the matrix after the second truncation, all of the two dimensional Hamiltonians having been truncated.

The three-dimensional $^{DVR}H$ matrix of Eq. 2.34 is then transformed to $^{DVR}\bar{H}$ in the truncated 1D-eigenvector representation:

$$\bar{H}_{l\beta K}^{l'\beta'K'} = \sum_{\alpha\alpha'} {}^{1D}\bar{C}_{\alpha'l'}^{\beta'K'} \cdot {}^{DVR}H_{\alpha\beta K}^{\alpha'\beta'K'} \cdot {}^{1D}\bar{C}_{\alpha l}^{\beta K} \tag{2.42}$$
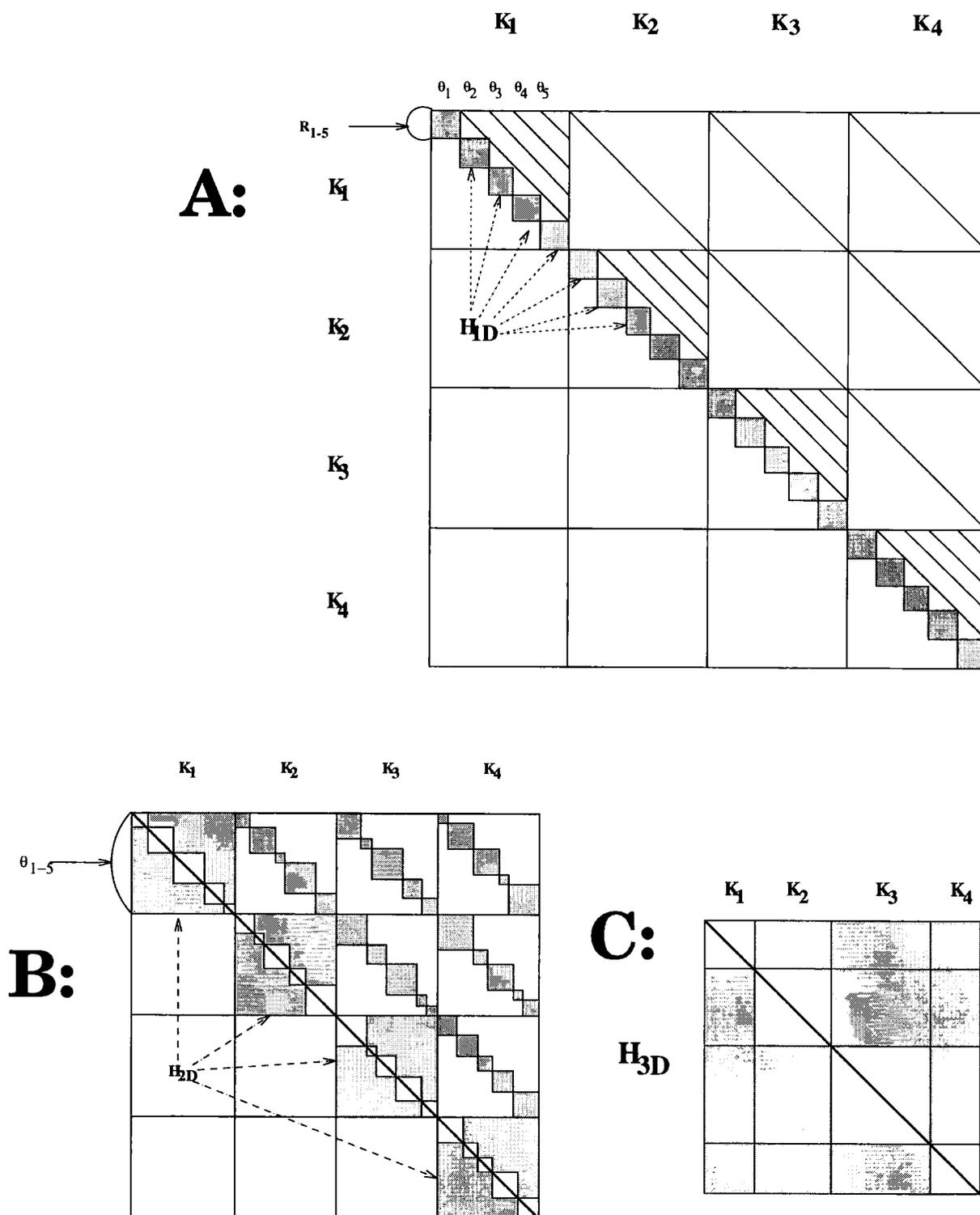
**Figure 2.4:** Solution of DVR Hamiltonian by successive diagonalisation and truncation.  **A:**3D H in DVR;  **B**: H in truncated 1D basis, 2D DVR;  **C**: H in the truncated 2D basis, 1D DVR.

For each $(\beta K)(\beta' K')$ block the transformation reduces the DVR of the $(N_R \times N_R)$ $^{1D}h$ matrix to the $(M_{\beta K} \times M_{\beta K})$ matrix of the 1D-eigenvector basis.

In the truncated $^{1D}h$ eigenvector basis the 2D Hamiltonians, which consist of terms that are diagonal in $K$, are given by:

$$
\begin{aligned}
^{2D}h_{l\beta}^{l'\beta'} &= \sum_{\alpha'\alpha} {}^{1D}\bar{C}_{\alpha'l'}^{\beta'K'} \left\{ {}^{1D}h_{\alpha\alpha'}\delta_{\beta\beta'} + \left( \frac{\hbar^2}{2\mu_1 R_\alpha^2} + \mathrm{b_v} \right) {}^{\theta K}d_{\beta\beta'}\delta_{KK'} \right. \\
&\quad \left. + \frac{\hbar^2}{2\mu_1 R_\alpha^2} \left[ J(J+1) - 2K^2 \right] \delta_{\alpha\alpha'}\delta_{\beta\beta'} \right\} \delta_{KK'} {}^{1D}\bar{C}_{\alpha l}^{\beta K} \\
&= {}^{1D}E_l^{\beta K}\delta_{ll'}\delta_{\beta\beta'}\delta_{KK'} + \left( \Omega_{l\beta K}^{l'\beta'K'} + \Xi_{l\beta K}^{l'\beta'K'} \right) {}^{\theta K}d_{\beta\beta'}\delta_{KK'} \\
&\quad + \frac{\hbar^2}{2\mu_1}\Omega_{l'\beta K}^{l'\beta'K'} \left[ J(J+1) - 2K^2 \right] \delta_{\beta\beta'}\delta_{KK'}
\end{aligned}
\tag{2.43}
$$

where

$$
\Omega_{l\beta K}^{l'\beta'K'} = \frac{\hbar^2}{2\mu_1} \sum_\alpha {}^{1D}\bar{C}_{\alpha'l'}^{\beta'K'} \frac{1}{R_\alpha^2} {}^{1D}\bar{C}_{\alpha l}^{\beta K}
\tag{2.44}
$$

$$
\Xi_{l\beta K}^{l'\beta'K'} = \sum_\alpha {}^{1D}\bar{C}_{\alpha'l'}^{(\beta'K')}\mathrm{b_v}\,{}^{1D}\bar{C}_{\alpha l}^{(\beta K)}
\tag{2.45}
$$

in which $l = 1, 2, \ldots, M_{\beta K}$ $l' = 1, 2, \ldots, M_{\beta'K}$ and $\beta = 1, 2, \cdots, N_\theta$. Of course for a $J = 0$ calculation (or a $J = 1$ $f$) there is only one value of $K$ and the eigenvalues of $^{2D}h_{l\beta}^{l'\beta'}$ are the solutions of the problem. For a $J > 0$ calculation it is possible to diagonalise a different size of $^{2D}h$ for each value of $K$:

$$
{}^{2D}h^{(K)} = {}^{2D}C^{(K)} \cdot {}^{2D}E^{(K)} \cdot [{}^{2D}C^{(K)}]^T
\tag{2.46}
$$

The 2D-eigenvector matrix $^{2D}C^{(K)}$ has dimensions of $P_K \times P_K$ where $P_K = \sum_{\beta=1}^{N_\theta} {}^{1D}M_{\beta K}$. This two dimensional eigenvector basis can be truncated as before either by retaining a constant number of eigenvectors or using an energy cutoff condition:

$$
{}^{2D}E_m^{(K)} \le E_{2D}^{cut}
\tag{2.47}
$$

This truncated 2D-eigenvector basis is denoted $^{2D}\bar{C}^{(K)}$, for each value of $K$ a different number of eigenvectors, $^{2D}N_L$ maybe retained.

The $\bar{H}$ of Eq. 2.42 is now transformed to $\bar{\bar{H}}$ in the truncated 2D-eigenvector representation

$$
\bar{\bar{H}}_{mK}^{m'K'} = \sum_{\beta'\beta} \sum_{ll'} {}^{2D}\bar{C}_{l'\beta'K'm'}^{(K')}\bar{H}_{l\beta K}^{l'\beta'K'}{}^{2D}\bar{C}_{l\beta m}^{(K)}
$$

$$= \sum_{\beta'\beta}\sum_{ll'} {}^{2D}\bar{C}^{(K')}_{l'\beta'm'} \left[ \sum_{\alpha} {}^{1D}\bar{C}^{(\beta'K')}_{\alpha'l'} \frac{\hbar^2}{2\mu_1 R_\alpha^2} [-(1+\delta_{K0})^{1/2}\Lambda^+_{JK}B^+_{\beta\beta'}\delta_{K,K+1} \right.$$

$$\left. -(1+\delta_{K'0})^{1/2}\Lambda^-_{JK}B^-_{\beta\beta'}\delta_{K,K-1} {}^{1D}\bar{C}^{(\beta K)}_{\alpha l}\right] {}^{2D}\bar{C}^{(K)}_{l\beta m}$$

$$+{}^{2D}E^{(K)}_m\delta_{mm'} \tag{2.48}$$

where ${}^{2D}E^{(K)}_m$ are the eigenvalues of the 2D-Hamiltonian matrix. This part of the SDT procedure, solving a set of different vibrational problems that treat $K$ as good quantum number then recoupling them to obtain results for $J > 0$ calculations, was first described by Tennyson and Sutcliffe [52].

## 2.6 Nuclear Spin Statistics

Upon the exchange of two identical particles the total wave function of a molecule $\Psi$, must change to $-\Psi$ if they are fermions and to $+\Psi$ of they are bosons for the system to obey the Pauli principle. This calculation concentrates on the ${}^{12}C^{16}O_2$ isotopic variant of $CO_2$ in which the two oxygen nuclei are identical. The ${}^{16}O$ nucleus has a nuclear spin quantum number of zero and is a boson. The total wave function is restricted therefore to be symmetric. For $CO_2$ in its vibrational ground state the vibrational wave function is symmetric and therefore only states with even values of $j$, the monomer rotation quantum number, exist. Conversely, for the $\nu_3$ antisymmetric stretch only states with odd $j$ exist. The quantum number $j$ denotes the symmetry with respect to a 180° rotation of the $CO_2$ molecule. Therefore the basis set in $\theta$ contains even or odd Legendre polynomials only. (For a more complete discussion see Refs. [53, 54].)

It is therefore possible to perform a symmetry-adapted calculation. The symmetry of the $CO_2$ molecule means the Hamiltonian splits into two independent blocks corresponding to either even or odd symmetry with respect to rotation of the $CO_2$ molecule. In a DVR calculation one uses DVR quadrature points in the range $0° \rightarrow 90°$ and multiplies the corresponding quadrature weights by 2. The basic principle behind this is that the wave function in the range $0° \rightarrow 90°$ uniquely defines the problem.

## 2.7  Results of calculations on $ArCO_2$

All these calculations are for $J = 0$ states. They are designed to test the feasibility of DVR calculations on Van der Waals molecules and to determine the difficulties that may occur when performing the calculation on a system with three degrees of freedom.

### 2.7.1  Non-Truncated Hamiltonian matrix

Initially the full Hamiltonian matrix was constructed, without any successive diagonalisation and truncation, to determine the convergence with respect to the size of basis set and $R_{min}$ and $R_{max}$. After constructing the Hamiltonian matrix it was diagonalised (its eigenvalues and eigenvectors determined) using a standard computational routine from the Nag library [55] to obtain the energy levels and the wave functions of the molecule. The Nag routine uses the Householder method to solve the eigenvalue problem. This works by applying a series of similarity transformations to the Hamiltonian matrix. It therefore requires that the Hamiltonian matrix is stored in full in memory.

Figure 2.5 shows the rate of convergence of the lowest twenty energy levels of $ArCO_2$ as a function of the number of quadrature points, $N_R$, in the $R$ coordinate. The number of quadrature points in $\theta$ was held at 18 for all these calculations, $R_{min} = 2.4$ Å and $R_{max} = 8.0$ Å. The graphs clearly show the superiority of the convergence properties of the potential-optimised DVR quadrature points compared to those obtained from the Sturmian functions. It takes $\sim$30 potential-optimised points and $\sim$40 Sturmian points to converge the energy levels to $4 \times 10^{-5}$ cm$^{-1}$.

The positions of the DVR quadrature points obtained from the two different methods, shown in figure 2.6, illustrate why the potential-optimised points are superior. The Sturmian points are too densely spread in the region of the repulsive wall of the potential which means the total number of points has to be larger for the description at the minimum to be correct.
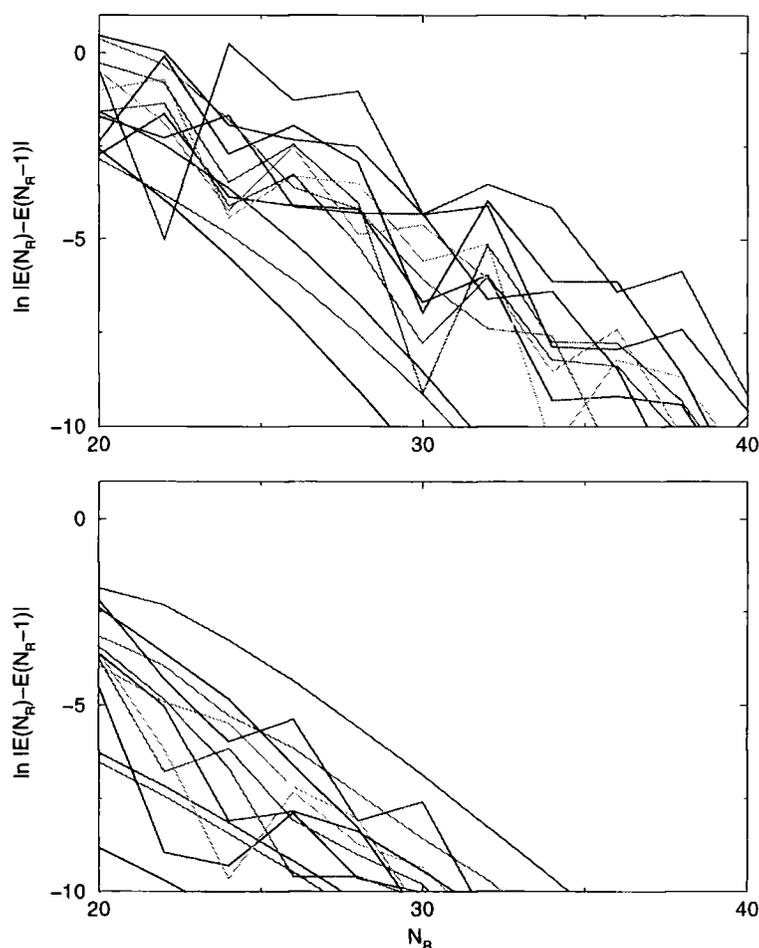
**Figure 2.5:** Convergence in the energy levels of $ArCO_2$ as a function of increasing number of DVR quadrature points. The upper plot shows the convergence of the Sturmian derived points and the lower the convergence of the potential-optimised points.

## 2.7.2  Truncated Hamiltonian matrix

For these calculations the basis set parameters remained the same as those in the non-truncated calculations. The number of quadrature points in $R$ was set to 40. For an SDT calculation the convergence properties with respect to the cut-off energy $E_{cut}^{1D}$ must be determined. With $E_{cut}^{1D}$ set to $\infty$ (or more practically $10^{99}$) the calculation is equivalent to the non-truncated one and would correspond to a matrix of dimension 720. By decreasing $E_{cut}^{1D}$ it is possible to reduce the final the dimensions of the final Hamiltonian matrix to be diagonalised, thus speeding up the calculation. At some point however the
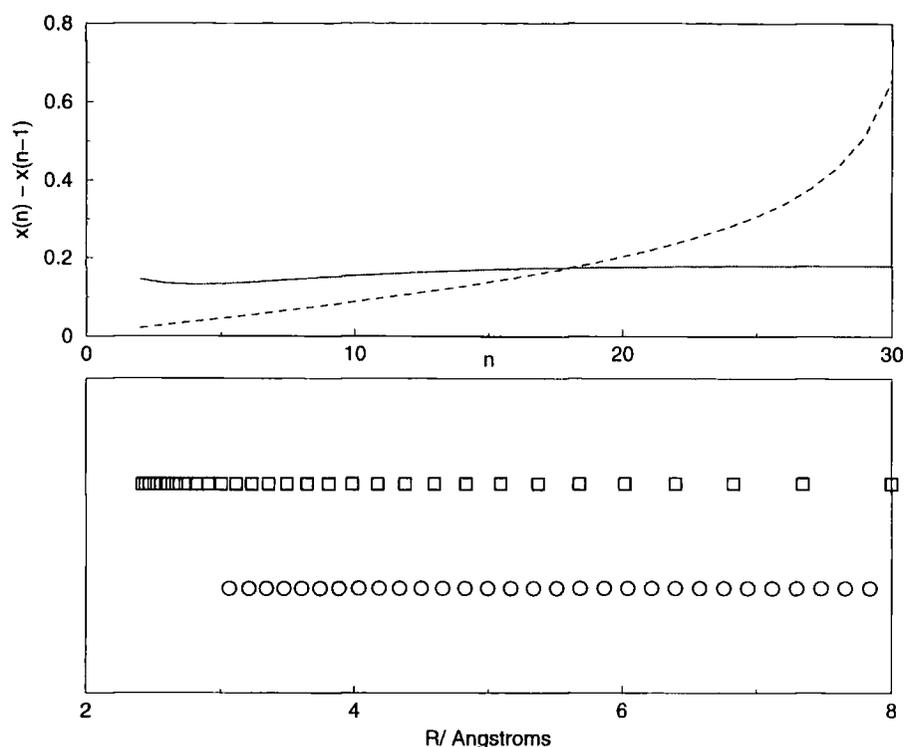
**Figure 2.6:** The DVR quadrature points in $R$ (lower figure). The squares are the Sturmian points and the circles the potential-optimised ones. The upper figure shows their spacing. The solid line corresponds to the potential-optimised functions. The small dip in this around r=2.5Å indicates the increased density of points around the minimum in the potential. The dotted line corresponds to the Sturmian points. The very low values at small values of $R$ show that the spacing of the quadrature points is too dense in this region.

accuracy of the eigenvalues will begin to be affected and this the value of $E_{\text{cut}}^{1D}$ I wish to determine.

Figure 2.7 clearly shows that to achieve the same convergence criteria as that for the other basis set parameters the value of $E_{\text{cut}}^{1D}$ must be 500 cm$^{-1}$ or greater. The calculation with $E_{\text{cut}}^{1D} = 500$ cm$^{-1}$ (which has dimension 359) is about 4-5 times faster than that for a non-truncated matrix. I suspect that there is a large error in the calculation of this factor. The two CPU times were 0.83 seconds and 4.79 seconds for the truncated and untruncated jobs respectively. For such a small amount of time the actual execution time can depend upon many factors not just the theoretical number of floating point
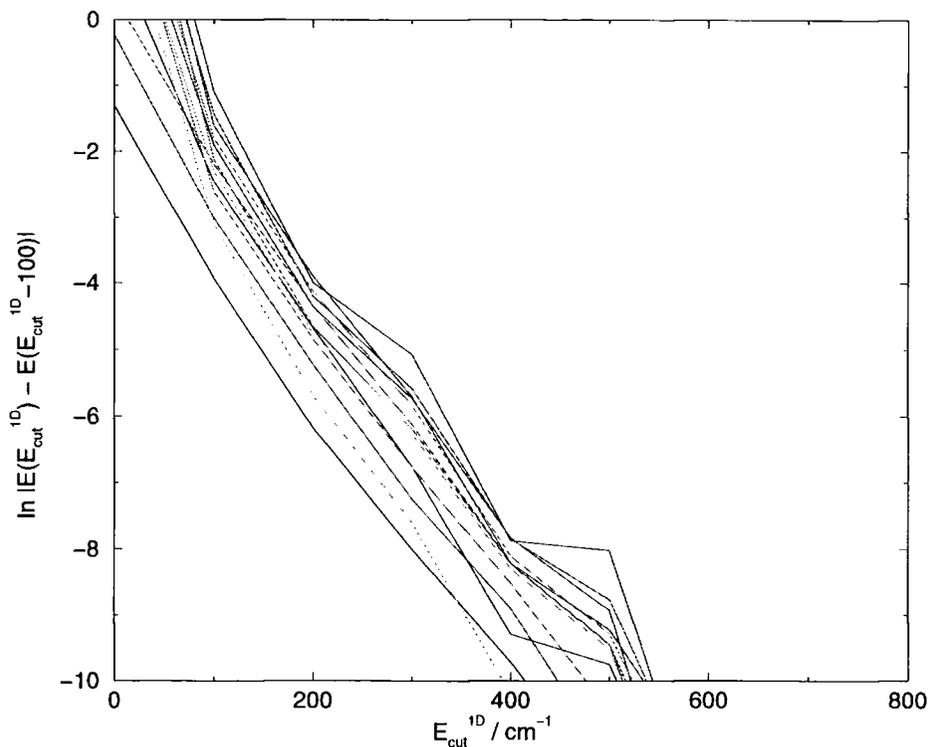
**Figure 2.7:** Convergence in the energy levels of $ArCO_2$ as a function of increasing $E_{cut}^{1D}$. A value of 100 cm$^{-1}$ corresponds to a matrix of dimension 291. A value of 600 cm$^{-1}$ corresponds to a matrix of dimension 359.

operations. Theoretically it should take 8 times longer to diagonalise a matrix of dimension $2n$ compared to a matrix of dimension $n$ ($n^3$ scaling).

## 2.8  Extension to systems with three degrees of freedom

It is possible to use the results of these calculations to obtain an idea of approximately how many DVR quadrature points will be required for a molecule with three degrees of freedom. Roughly 30 quadrature points in the $R$ coordinate and 18 in the $\theta$ coordinate are going to be required. For the $ArCO_2$ molecule this produces a matrix of dimension $540 \times 540$ ($30 \times 18 = 540$) which takes up $540 \times 540 \times 8/2^{20} = 2.22$ MB of memory. Assuming that the third degree of freedom, $r$, needs roughly 30 quadrature points (it will have similar requirements to $R$) I would need $30 \times 30 \times 2.22 = 2002$ MB of memory to store the

matrix!! The SDT scheme can reduce this by approximately a factor of two, but this still represents one gigabyte of storage—a vast amount of memory. To perform such a calculation, by explicit construction of the Hamiltonian matrix, is therefore out of the question.

If anything this approximate calculation is an underestimate of the requirements because there are many more bound states of $Ar_3$ than $ArCO_2$. I must therefore find a different method of diagonalising the Hamiltonian matrix. To construct the matrix, even with the use of SDT, and then pass it to a standard subroutine from a library is not going to be possible for a molecule such as $Ar_3$.

The factor of two reduction in the size of the basis using SDT for $ArCO_2$ is not that much of an advantage. I suspect that if the coordinate ordering were swapped and the first diagonalisation was performed at points in $R$ not points in $\theta$, there may be a change in the size of the final Hamiltonian that needs to be diagonalised. The method used by Choi and Light was optimised for the ArHCl molecule not $ArCO_2$ and the optimum ordering of coordinates is known to be system-dependent [56]. Of course for a molecule with three degrees of freedom a further level of truncation is possible and this may produce a larger reduction in the size of the matrix. However I think this still provides evidence that for some floppy molecules SDT is not very effective. In their study on the $H_3^+$ molecular ion Henderson $et\ al.$ only managed to reduce their Hamiltonian matrix by a factor of less than 3 [21]. The cost of having to deal with the complex structure of the contracted basis seems expensive when compared to the relatively small gain in terms of CPU time. The similarity of $Ar_3$ and $H_3^+$ suggests that the SDT scheme will be similarly inefficient for $Ar_3$.

The solution to this problem has been outlined by Bramley $et\ al.$ [22]. They used an entirely different method to diagonalise the Hamiltonian matrix, which is described in the next chapter.

CHAPTER

———————— 3 ————————

# Diagonalising large matrices.

The aim of this chapter is to describe how to diagonalise the Hamiltonian matrix for molecules with three floppy degrees of freedom. At the end of the previous chapter it was demonstrated that the method used to diagonalise the matrix for the $ArCO_2$ system could not be extended because the matrix would be too big to store in memory.

There are two possible ways of solving this problem. I can either reduce the size of the matrix I wish to diagonalise (whilst retaining the relevant information within it) [24] or I can find another method of obtaining the eigensolutions that does not require the explicit construction of the Hamiltonian matrix [22]. The SDT scheme corresponds to the first possibility and the previous chapter illustrates that on its own it will not reduce the size of the matrix by a large enough amount. This chapter concentrates on the second possibility.

# 3.1   Lanczos method

This is an application of the Arnoldi algorithm which when applied to real, symmetric matrices (as all mine are) is called the Lanczos algorithm [57]. It is a method of obtaining the eigenvalues and eigenvectors of a matrix that differs from the Householder reduction scheme that was used for the calculation on the $ArCO_2$ molecule described in chapter 2.

The Lanczos algorithm is an iterative method. Each iteration involves the calculation of the product of the Hamiltonian matrix with a vector. This produces a matrix element of a tridiagonal matrix $T$ that is orthogonally similar to the matrix, $H$, being diagonalised. To obtain all the eigenvalues of $H$ a large number of iterations would be needed. After only a few iterations however the extreme eigenvalues of $T$ provide extremely good approximations to the extreme eigenvalues of $H$.

Historically the main problem with implementing the Lanczos method was the difficultly of ensuring that the Lanczos vectors remained orthogonal to each other (which can lead to 'ghost' eigenvalues). The development of the Householder reduction method, which is much more stable, meant that the Lanczos method was largely unused for many years. The recent development of a more stable implementation of the algorithm [58] as a freely available set of Fortran subroutines [59, 60] has lead to several calculations upon floppy molecules being performed using the Lanczos method [22, 51, 61, 62].

The key to the success of the Lanczos method when applied to DVR calculations is the sparsity of the Hamiltonian matrix. Many of the matrix elements are known to be identically equal to zero negating the need to store them or compute their product with the Lanczos vector. The diagonalisation of a FBR Hamiltonian matrix using Lanczos, for example, would be difficult because no matrix elements are known to be equal to zero. This would make the computational effort involved in calculating the matrix-vector product very large.

As previously mentioned the extreme eigenvalues of $H$ are obtained after only a few iterations of the algorithm. The rate of convergence of a particular eigenvalue depends upon the distribution of the all the eigenvalues of

the matrix (the eigenvalue spectrum). If the eigenvalue is in a tightly clustered region of the spectrum then more iterations will be needed to obtain it. Also if the range of the eigenvalue spectrum is large (the difference between the smallest and largest eigenvalue) the algorithm will converge much more slowly. Therefore increasing the spacing between the eigenvalues of interest and keeping the range of the eigenvalue spectrum as small as possible will ensure the calculation converges rapidly.

To improve the separation of the eigenvalue spectrum the Chebychev polynomial preconditioning scheme as described by Korambath, Wu and Hayes [61] is used. This involves finding the eigenvectors of a polynomial function of the matrix and then using these to obtain the eigenvalues of the original matrix via Rayleigh quotients, i.e. first obtain the solution of the problem

$$\phi_m(H)q = \mu q \qquad (3.1)$$

and then compute the eigenvalues, $\lambda$,

$$\lambda = \frac{q^T H q}{q^T q} \qquad (3.2)$$

A Chebychev polynomial has been shown [61] to be a good choice for $\phi_m$. The Chebychev preconditioning polynomial is calculated from

$$\phi_m(H) = \prod_{j=1}^{m} \left( I - \frac{H}{\mu_j} \right) \qquad (3.3)$$

where

$$\mu_j = c + b\cos(\eta_j), \qquad \eta_j = \frac{(2j-1)\pi}{2m}, \qquad j = 1, 2, \ldots, m \qquad (3.4)$$

where $c$ is the centre and $b$ is half the length of the interval $(a_0, a_1)$. The effectiveness of the method depends upon the choice of $a_0$, $a_1$ and $m$. $a_1$ and $a_0$ are the range of eigenvalues which do not need to be determined. $a_1$ is set to the highest eigenvalue of the matrix which can be rapidly determined because of its large separation from the rest of the spectrum. $a_0$ is set to an amount slightly greater than the largest eigenvalue to be calculated. The optimal value for $m$ is a little more difficult to decide upon and is problem dependent. When $m$ is too small the spacing of the eigenvalues is not great enough and the matrix is not well conditioned. If it is too great the number of matrix

vector operations becomes unnecessarily large because each iteration of the algorithm requires $m$ matrix-vector multiplications. What this means is that the value of $m$ must be determined empirically by running several small test calculations. Figure 3.1 shows the original and transformed eigenvalue spectrum of $ArCO_2$. The original spectrum is very dense at the lower end whereas the transformed spectrum has much more widely spaced eigenvalues making the convergence of the Lanczos algorithm much more rapid.

## 3.2   Implementing the IRLM

To diagonalise the a matrix using the IRLM method it is necessary to compute the product of the matrix and a vector. The DVR Hamiltonian matrix elements are defined by:

$$
\begin{aligned}
\mathbf{H}_{\alpha\beta\gamma K}^{\alpha'\beta'\gamma'K'} &= \sum_{ii'jj'll'} {}^R T_{i'\alpha'}{}^r T_{j'\beta'}{}^{K\theta} T_{l'\gamma'} H_{ijlK}^{i'j'l'K'} {}^R T_{i\alpha}{}^r T_{j\beta}{}^{K\theta} T_{l\gamma} \\
&= {}^R d_{\alpha'\alpha}\delta_{\beta'\beta}\delta_{\gamma\gamma'}\delta_{K'K} + {}^r d_{\beta'\beta}\delta_{\alpha'\alpha}\delta_{\gamma\gamma'}\delta_{K'K} \\
&\quad + \frac{\hbar^2}{2}\left(\frac{1}{\mu_1 R_\alpha^2} + \frac{1}{\mu_2 r_\beta^2}\right){}^{\theta K} d_{\gamma'\gamma}\delta_{\alpha'\alpha}\delta_{\beta\beta'}\delta_{K'K} \\
&\quad + \frac{\hbar^2}{2\mu R_\alpha^2}\bigg(\left[J(J+1)-2K^2\right]\delta_{\alpha'\alpha}\delta_{\beta'\beta}\delta_{\gamma\gamma'}\delta_{K'K} \\
&\quad - \left[1+\delta_{K0}\right]^{1/2}\Lambda_{JK}^+ B_{\gamma\gamma'K}^+\delta_{\alpha'\alpha}\delta_{\beta'\beta}\delta_{K'K+1} \\
&\quad - \left[1+\delta_{K'0}\right]^{1/2}\Lambda_{JK}^- B_{\gamma\gamma'K}^-\delta_{\alpha'\alpha}\delta_{\beta'\beta}\delta_{K'K-1}\bigg) \\
&\quad + V_{\alpha\beta\gamma}^{\alpha'\beta'\gamma'}\delta_{K'K}
\end{aligned}
\tag{3.5}
$$

The main advantage of using a IRLM diagonaliser combined with a DVR representation is the sparsity of the Hamiltonian matrix. The purpose of this section is to illustrate the algorithm used to compute the matrix-vector products efficiently.

The structure of the Hamiltonian matrix dictates the procedure. A Hamiltonian matrix that is a function of three coordinates can be constructed in six possible ways. These are all equivalent but some orderings make the computation of the matrix-vector product slightly less expensive than others.

I have chosen to construct the matrix in the order $R$, $r$, $\theta$. This facilitates a slight reduction in the number of floating point operations that are required
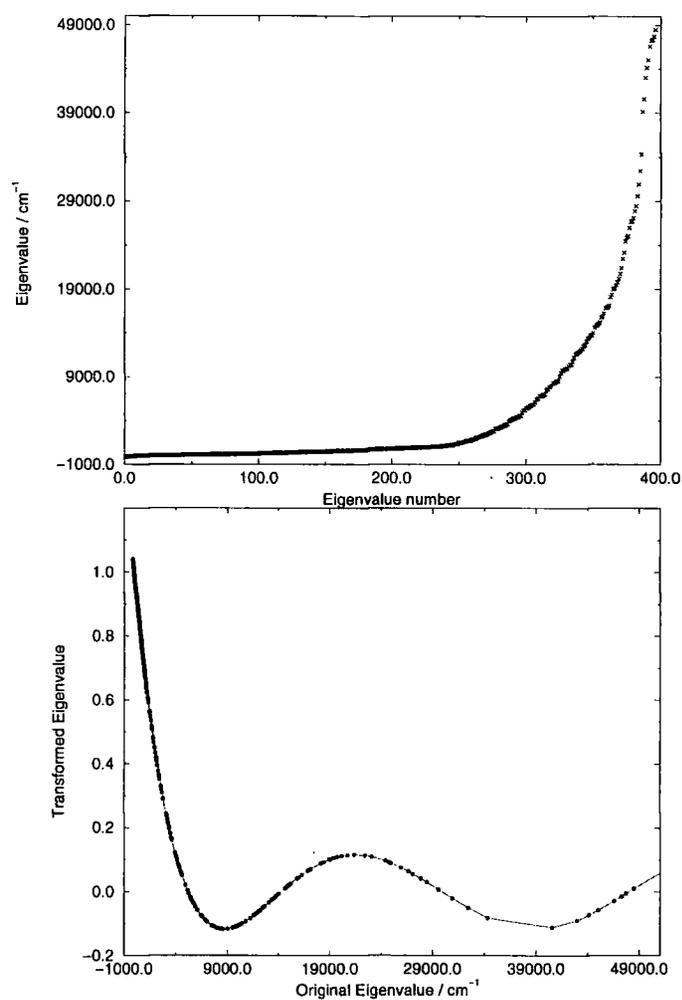
**Figure 3.1:** Original Eigenvalue spectrum of $ArCO_2$ as a function of eigenvalue number and Transformed Eigenvalue spectrum of $ArCO_2$ using a Chebychev polynomial preconditioning function as a function of the original eigenvalues.

to compute the matrix-vector product compared to other orderings.

To outline the algorithm used it is helpful to define three quantities $N_R$, $N_r$ and $N_\theta$ which represent the number of DVR basis functions in each of the three dimensions of the problem. The Hamiltonian matrix is constructed from 4 matrices ($^R d(N_R, N_R)$, $^r d(N_r, N_r)$, $^{\theta K} d(N_\theta, N_\theta)$ and $B^+(N_\theta, N_\theta)$ ) and three vectors ( $\frac{1}{\mu_1 R^2}(N_R)$, $\frac{1}{\mu_2 r^2}(N_r)$ and $V(N_R \times N_R \times N_\theta)$. These represent all the required information, along with numerical factors (such as $\hbar$), needed to define the Hamiltonian matrix. From a knowledge of which elements of these matrices/vectors contribute to which matrix elements of the Hamiltonian it is possible to determine the product of the Hamiltonian matrix with the Lanczos vector without the need for explicit construction of the Hamiltonian matrix.

I shall outline how each of the seven components is used to compute the product of the Hamiltonian matrix with a vector $x$ (of dimension $N_R \times N_r \times N_\theta$).

The $^R d$ matrix is distributed as blocks along the diagonal of the Hamiltonian matrix. There are $N_r \times N_\theta$ such blocks. The multiplication can be written as:

$$
\begin{pmatrix}
^R d & & & \\
& ^R d & & \\
& & \ldots & \\
& & & ^R d
\end{pmatrix}
\begin{pmatrix}
x_{1 \ldots N_R} \\
x_{N_R+1 \ldots 2 \times N_R} \\
\ldots \\
x_{1+(N_r \times N_\theta -1) \times N_R, \ldots (N_r \times N_\theta) \times N_R}
\end{pmatrix}
\tag{3.6}
$$

The $^R d$ matrix is multiplied by a vector of length $N_R$ $N_r \times N_\theta$ times. These matrix-vector operations are handled by a BLAS [63] subroutine in the code.

The $^r d$ matrix is diagonal in $R$ and $\theta$ and is distributed in $N_\theta$ blocks of dimension $N_r \times N_r$:

$$
\begin{pmatrix}
^r d(1,1) & ^r d(1,2) & \ldots & ^r d(1, N_r) \\
^r d(2,1) & ^r d(2,2) & \ldots & ^r d(2, N_r) \\
\ldots & \ldots & \ldots & \ldots \\
^r d(N_r,1) & ^r d(N_r,2) & \ldots & ^r d(N_r, N_r)
\end{pmatrix}
\begin{pmatrix}
x_{1, \ldots, N_R} \\
x_{N_R+1 \ldots 2 \times N_R} \\
\ldots \\
x_{1+(N_r \times N_\theta -1) \times N_R, \ldots (N_r \times N_\theta) \times N_R}
\end{pmatrix}
\tag{3.7}
$$

Each element of the $^r d$ matrix is multiplied by a vector of length $N_R$. For example the elements $^r d(1,1), ^r d(2,1), \ldots, ^r d(N_r,1)$, are all multiplied by the

vector

$$
\begin{pmatrix}
x_1 \\
x_2 \\
\ldots \\
x_{N_R}
\end{pmatrix}
\tag{3.8}
$$

The ${}^{\theta K}d$ matrix is diagonal in $R$ and $r$. The operator this represents involves the vectors $\frac{1}{\mu_1 R^2}(N_R)$, $\frac{1}{\mu_2 r^2}(N_r)$ also which complicates the issue slightly. Firstly the ${}^{\theta K}d$ matrix is multiplied:

$$
\begin{pmatrix}
{}^{\theta K}d(1,1) & {}^{\theta K}d(1,2) & \ldots & {}^{\theta K}d(1,N_\theta) \\
{}^{\theta K}d(2,1) & {}^{\theta K}d(2,2) & \ldots & {}^{\theta K}d(2,N_\theta) \\
\ldots & \ldots & \ldots & \ldots \\
{}^{\theta K}d(N_\theta,1) & {}^{\theta K}d(N_\theta,2) & \ldots & {}^{\theta K}d(N_\theta,N_\theta)
\end{pmatrix}
\begin{pmatrix}
x_{1,\ldots,N_R \times N_r} \\
x_{N_R \times N_r+1 \ldots 2 \times N_R \times N_r} \\
\ldots \\
x_{1+(N_\theta-1) \times N_r \times N_R, \ldots (N_\theta) \times N_r \times N_R}
\end{pmatrix}
\tag{3.9}
$$

The result of this, denoted $x'$, is then multiplied by the vectors $\frac{1}{\mu_1 R^2}(N_R)$ and $\frac{1}{\mu_2 r^2}(N_r)$ :

$$
\begin{pmatrix}
\frac{1}{\mu_1 R^2}(1) + \frac{1}{\mu_2 r^2}(1) \\
\frac{1}{\mu_1 R^2}(2) + \frac{1}{\mu_2 r^2}(1) \\
\ldots \\
\frac{1}{\mu_1 R^2}(N_R) + \frac{1}{\mu_2 r^2}(1) \\
\frac{1}{\mu_1 R^2}(1) + \frac{1}{\mu_2 r^2}(2) \\
\ldots \\
\frac{1}{\mu_1 R^2}(N_R) + \frac{1}{\mu_2 r^2}(N_r)
\end{pmatrix}
\begin{pmatrix}
x'_1 \\
x'_2 \\
\ldots \\
x'_{N_R} \\
x'_{N_R+1} \\
\ldots \\
x'_{N_R \times (N_r \times N_\theta-1), \ldots, N_R \times N_r \times N_\theta}
\end{pmatrix}
\tag{3.10}
$$

The computation of the product of the $B^+(N_\theta, N_\theta)$ matrix and the vector is similar to that of the ${}^{\theta K}d(N_\theta, N_\theta)$ matrix, the only difference coming from it being off-diagonal in $K$. The potential energy is of course diagonal in a DVR Hamiltonian matrix and the computation of its product with the vector is straightforward.

## 3.3  Combining successive diagonalisation and truncation with the IRLM

It is possible to combine the two approaches described in this chapter [51, 62]. The 1D and 2D Hamiltonian matrices in the SDT approach could be di-

agonalised conventionally with the final 3D matrix being diagonalised by the Lanczos method. This matrix is not sparse, in fact it will be very dense, so the matrix vector multiplication step in such an approach is not that efficient. However with the use of a state-of-the-art supercomputer and a parallel implementation of the combined SDT + Lanczos algorithm several studies have been performed [51,62].

In a study of several floppy molecules Bramley *et al.* [64] contrasted the efficiency of a Lanczos approach with a combined SDT Lanczos approach. They found that the relative efficiency of the two methods was system dependent and was related to the amount of truncation it was possible to perform. In their work they found that for $H_3^+$, where truncation only produced a factor of three reduction in the size of the Hamiltonian matrix, the uncontracted Lanczos method was more efficient. The similarity between $Ar_3$ and $H_3^+$ makes it reasonable to believe the same will be true for $Ar_3$ as well. Therefore I will attempt to obtain the energy levels of $Ar_3$ by diagonalising an uncontracted Hamiltonian matrix using the algorithm outlined in section 3.2.

In fact the above conclusion is the wrong one. The combined-SDT Lanczos approach is the most efficient for $Ar_3$. However the reason for this did not become clear until some uncontracted Lanczos calculations had been performed. These are described in chapter 5.

CHAPTER

<div style="border:1px solid black;">

## 4

# The potential energy surface and symmetry properties of $Ar_3$

</div>

In this chapter the potential energy surface used to describe the interactions in $Ar_3$ is outlined. Cuts through the surface are then used to determine the potential optimised basis functions. Finally the symmetry properties of $Ar_3$ are discussed with special reference to the boundary conditions they impose upon the basis functions.

## 4.1 The potential energy surface of $Ar_3$

The potential energy surface for a trimer, ABC, such as $Ar_3$ may be decomposed into pairwise-additive and nonadditive contributions,

$$V_{\text{trimer}} = V_{\text{AB}}(r_{\text{AB}}) + V_{\text{BC}}(r_{\text{BC}}) + V_{\text{AC}}(r_{\text{AC}}) + V_{\text{nonadd}} \tag{4.1}$$

where $r_{\text{AB}}$, $r_{\text{BC}}$ and $r_{\text{AC}}$ are the interatomic distances. At this stage I have used the pairwise-additive approximation which neglects the relatively small term
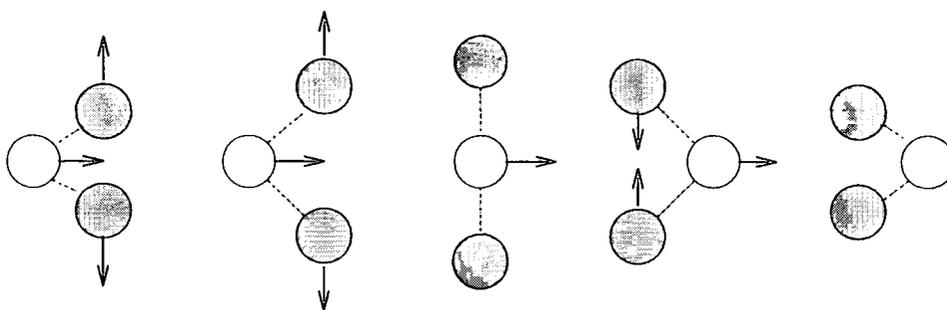
**Figure 4.1:** Cartoon showing the isomerisation pathway of a triangular tri-atomic molecule via a linear transition state.

$V_{nonadd}$. The resulting pairwise-additive surface is close enough to the true surface for my current needs. In the present work, the zero of energy corresponds to infinitely separated atoms.

The three interatomic distances can be obtained from the Jacobi coordinates by application of the cosine rule. A little trigonometry applied to figure 2.1 yields the following relations:

$$r_{AB} = (R^2 + r^2/4 + Rr\cos\theta)^{1/2} \tag{4.2}$$

$$r_{BC} = r \tag{4.3}$$

$$r_{AC} = (R^2 + r^2/4 - Rr\cos\theta)^{1/2} \tag{4.4}$$

The potential energy surface for $Ar_3$ is constructed using the HFD1D1 Ar–Ar pair potential of Aziz [13]. The resulting $Ar_3$ surface has a well depth of 299 $cm^{-1}$. Any pairwise-additive surface for an atomic trimer has a barrier to linearity that is very close to one third of the well depth, about 100 $cm^{-1}$ in this case. The lowest dissociation channel, to $Ar + Ar_2$ ($v = 0$) lies 85 $cm^{-1}$ below the separated atoms, and thus 214 $cm^{-1}$ above the equilibrium geometry.

The low energy of the linear configuration causes several difficulties with the bound state calculations as we shall see later. It means the molecule isomerises quite readily, passing from one triangular conformation to another, via a linear transition state. A cartoon of this motion is shown in figure 4.1.

Figures 4.2 and 4.3 show cuts through the pairwise additive surface at various values of $\theta$ along with the Jacobi coordinate system. The pathway of the isomerisation motion shown in figure 4.1 occurs with $\theta$ held at 90° and can quite clearly be seen on that cut through the potential. When $R = 0$ the
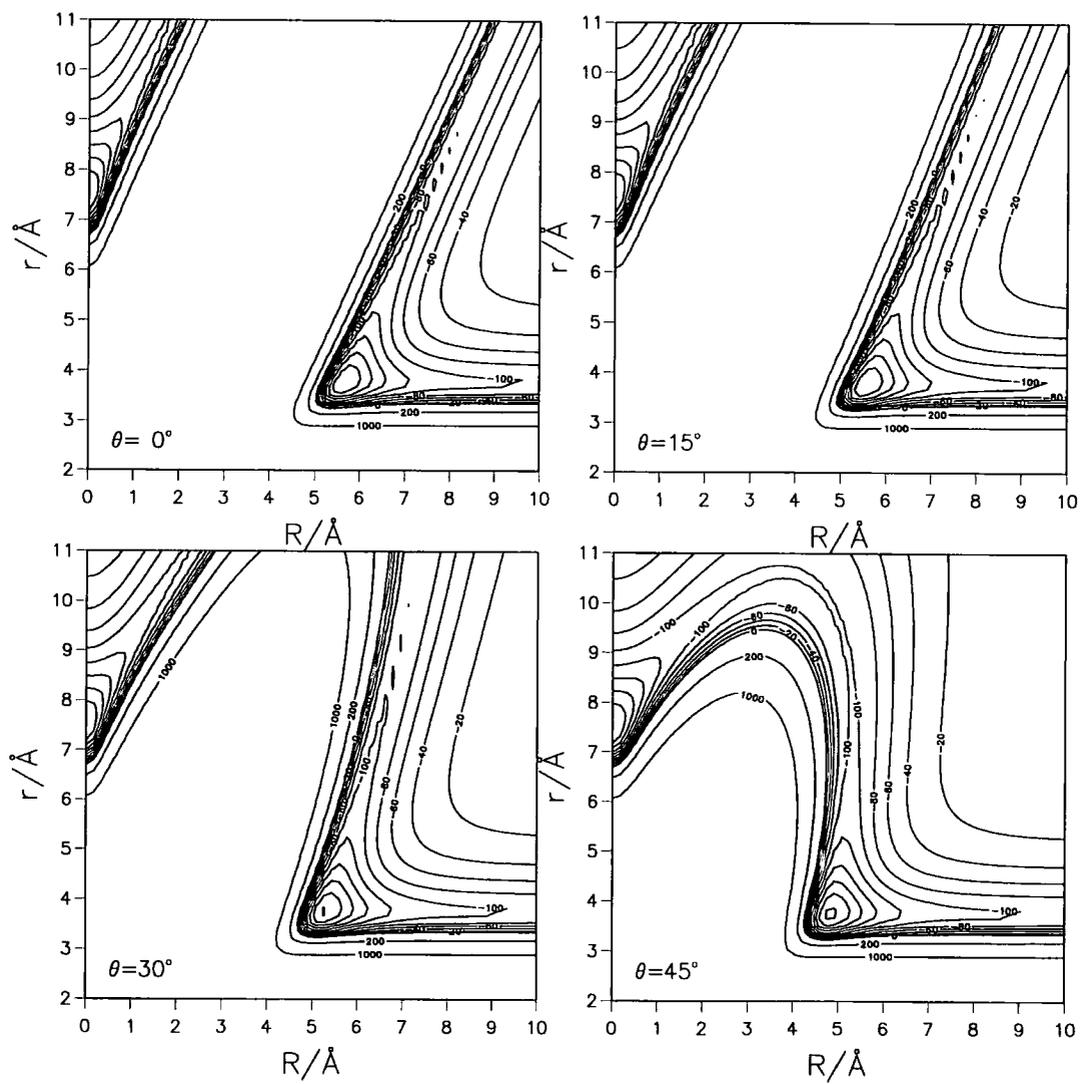
**Figure 4.2:** Contour plots of the potential energy surface of $Ar_3$ at various values of $\theta$.
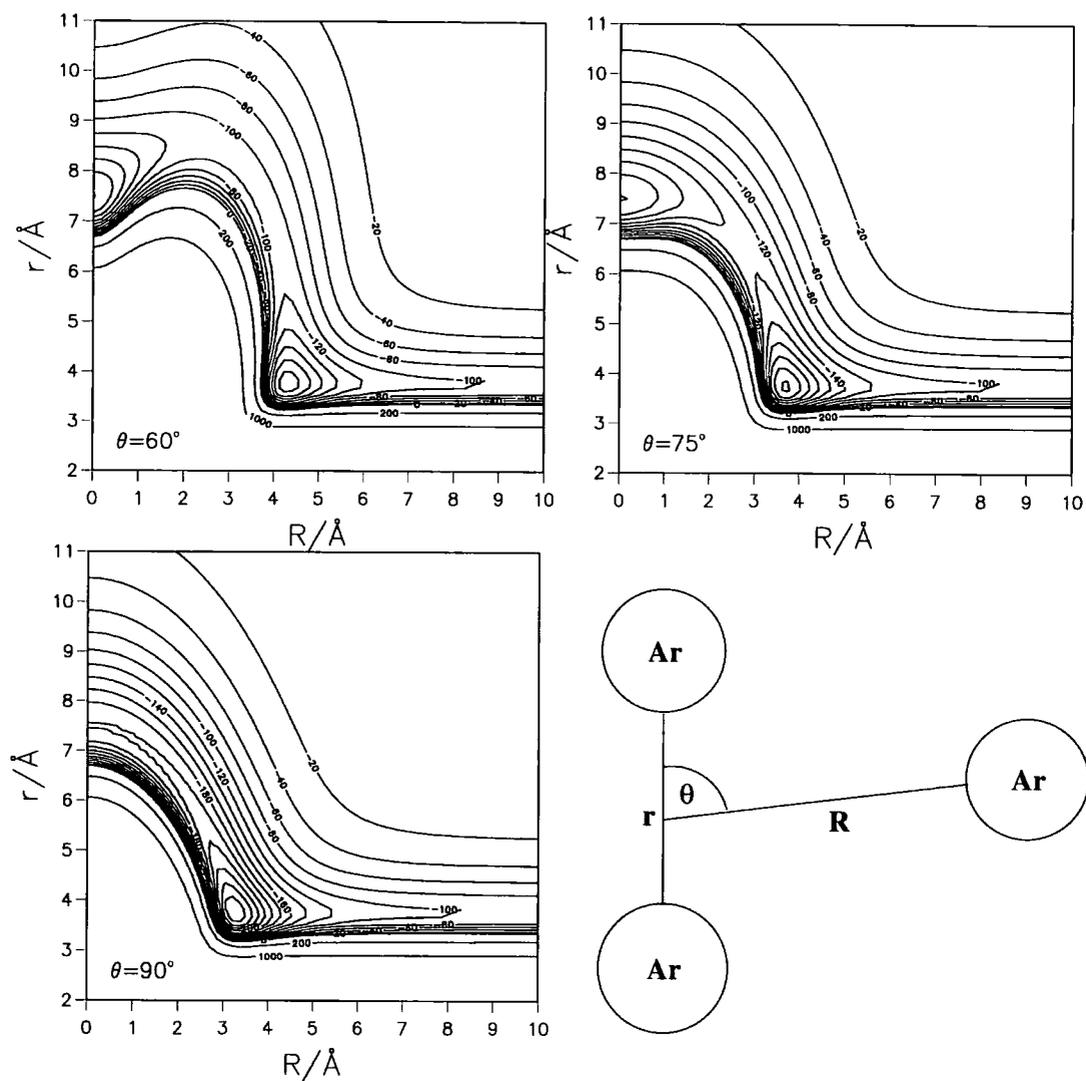
**Figure 4.3:** Contour plots of the potential energy surface of Ar$_3$ at various values of $\theta$ and the Jacobi coordinate system.

molecule is linear and the value of $\theta$ is undefined making all the cuts through the surface equivalent at that point.

## 4.2 Potential-Optimised Basis Functions

In chapter 2 the benefits of using a potential-optimised basis set were outlined. For Ar₃ I am going to use a potential-optimised basis in both the $R$ and the $r$ coordinates and therefore need to represent the wave function and define a one-dimensional Hamiltonian and two one-dimensional cuts.

The $n$th wave function of the system, with parity $p$ and total angular momentum $J$, may be expanded in a finite basis representation as

$$\Psi_n^{Jp}(R, r, \theta) = R^{-1} r^{-1} \sum_{ijlK} c_{ijlK}^n \, \phi_i^R(R) \phi_j^r(r) P_l^K(\cos \theta) \tag{4.5}$$

where the functions $P_l^K(\cos \theta)$ are associated Legendre polynomials. The functions $\phi_i^R(R)$ and $\phi_j^r(r)$ are potential-optimized basis functions in $R$ and $r$ (described below).

The one-dimensional Hamiltonian, $^{1D}\hat{H}_{\text{ref}}^R$ is taken to be

$$^{1D}\hat{H}_{\text{ref}}^R = -\frac{\hbar^2}{2\mu_1} \frac{\partial^2}{\partial R^2} + V_b^R(R) \tag{4.6}$$

where

$$V_b^R(R) = \frac{\hbar^2}{2\mu_1} \frac{L_m(L_m + 1)}{R^2} + V_{\text{min}}^R(R) \tag{4.7}$$

and $V_{\text{min}}^R(R)$ is obtained by minimising $V(R, r, \theta)$ with respect to $r$ at $\theta = 90°$. For the $R$ coordinate the cut follows the isomerisation pathway. This cut is shown in figure 4.4 along with the configuration of the molecule at a few points along it. The definition of $V_b^R(R)$ in Eq. (4.7) includes $L_m$, which is the minimum value of $L$ (the quantum number corresponding to end-over-end rotation in a space-fixed representation) for each symmetry block. The symmetry blocks are explained in more detail in section 4.3, but for now we note that for the even $(A_1/E)$ symmetry block $L$ is always even and therefore $L_m$ is 0. For the odd $(A_2/E)$ block $L$ is always odd and $L_m$ is 1. The $L_m(L_m + 1)$ term prevents any DVR points for the odd symmetry block being placed in the unsampled region of space near $R = 0$, where they would be wasted. It

also ensures the basis functions have the correct symmetry properties as discussed in section 4.3.

The procedure used to define the basis functions $\phi_j^r(r)$ for the $r$ coordinate is similar except that $V_{\min}^r(r)$ is obtained by minimising $V(R, r, \theta)$ with respect to $R$, at both $\theta = 90°$ and $0°$, and taking the lower of the two results. The cut follows the isomerisation pathway ($\theta$=90°) until the molecule becomes linear, after which it traces the path towards dissociation ($\theta$=0°). Figure 4.5 shows the cut through the potential along with the configurations of the molecule at a few points along it. Also shown in this figure are the potential-optimised basis functions derived from the cut. No $L_m(L_m+1)$ term is included in $V_{\min}^r(r)$ because the limit $r = 0$ corresponds to nuclear coalescence and is excluded by $V(R, r, \theta)$.

The basis-generating potentials $V_b^R(R)$ and $V_b^r(r)$ are designed to ensure that the basis sets span all values of one coordinate that are accessible at any value of another. Numerical functions obtained by solving the corresponding one-dimensional Hamiltonians are used in a calculation based on the HEG [39] method to obtain potential-optimized DVR (PO-DVR) [42] points in the required range.

## 4.3  Symmetry

The molecular symmetry group of Ar₃ is $D_{3h}(M)$. However, the only symmetry operation that appears naturally in Jacobi coordinates is permutation of the labels of the 'diatom' nuclei, which has the effect $\theta \to \pi - \theta$. Use of the Jacobi coordinate system effectively reduces the molecular symmetry group to $C_{2v}(M)$. The Hamiltonian matrix splits into two blocks, symmetric and antisymmetric with respect to the permutation. In terms of labels of $D_{3h}(M)$, the even block contains $A_1$ and $E$ (component 1) and the odd block contains $A_2$ and $E$ (component 2). The symmetric block contains only functions with $l$ even in Eq. (4.5) and the odd block contains only functions with $l$ odd.

Since the linear geometry with $R = 0$ is accessible in Ar₃, some care is needed to establish the boundary conditions that apply there [22, 23, 65]. Since $\Psi(R, r, \theta)$ must be finite or zero at $R = 0$, the basis functions $\phi_i^R(R)$ must
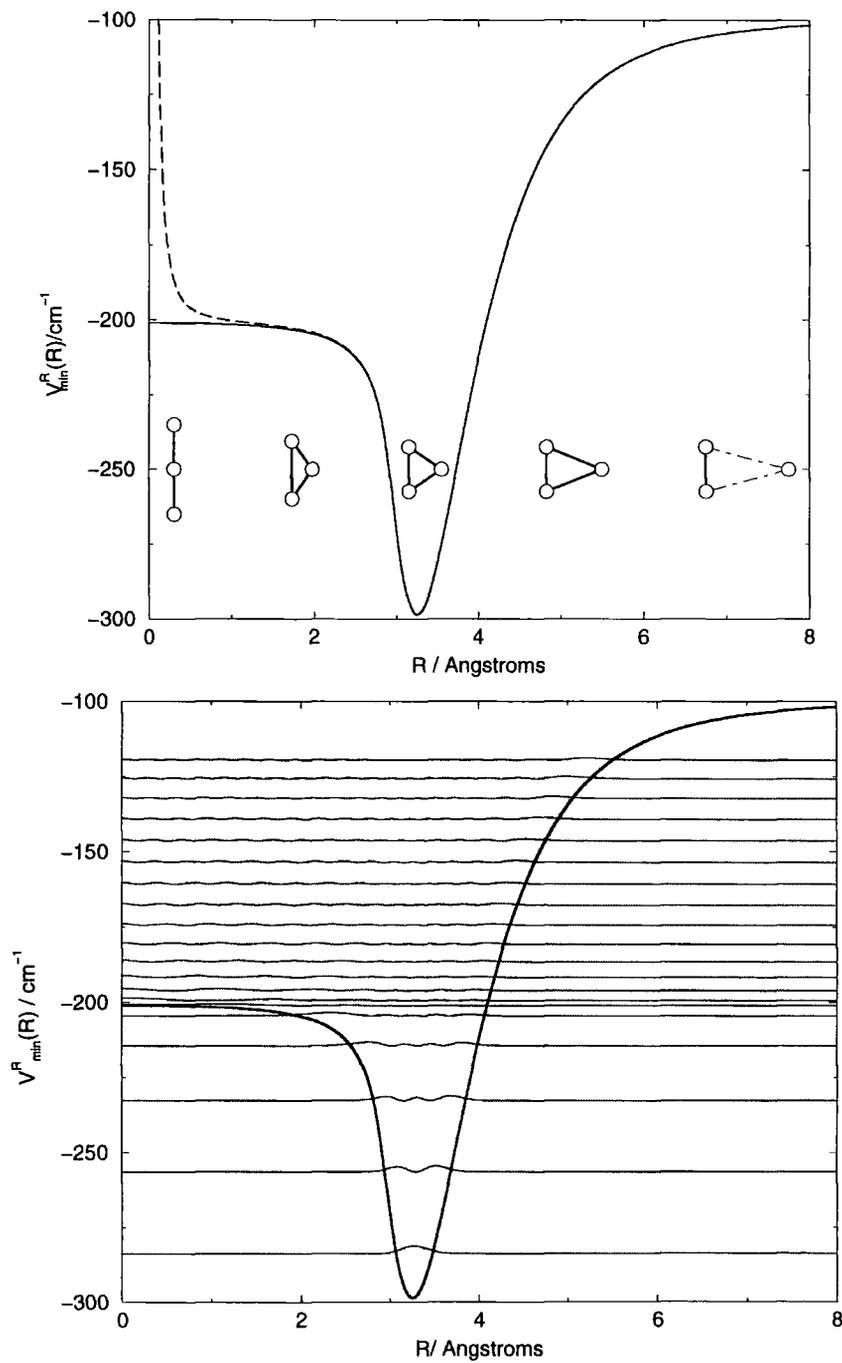
**Figure 4.4:** The cuts through the potential for generating the potential-optimised functions in $R$. The lower panel shows the functions derived from the potential with $L_m=0$.
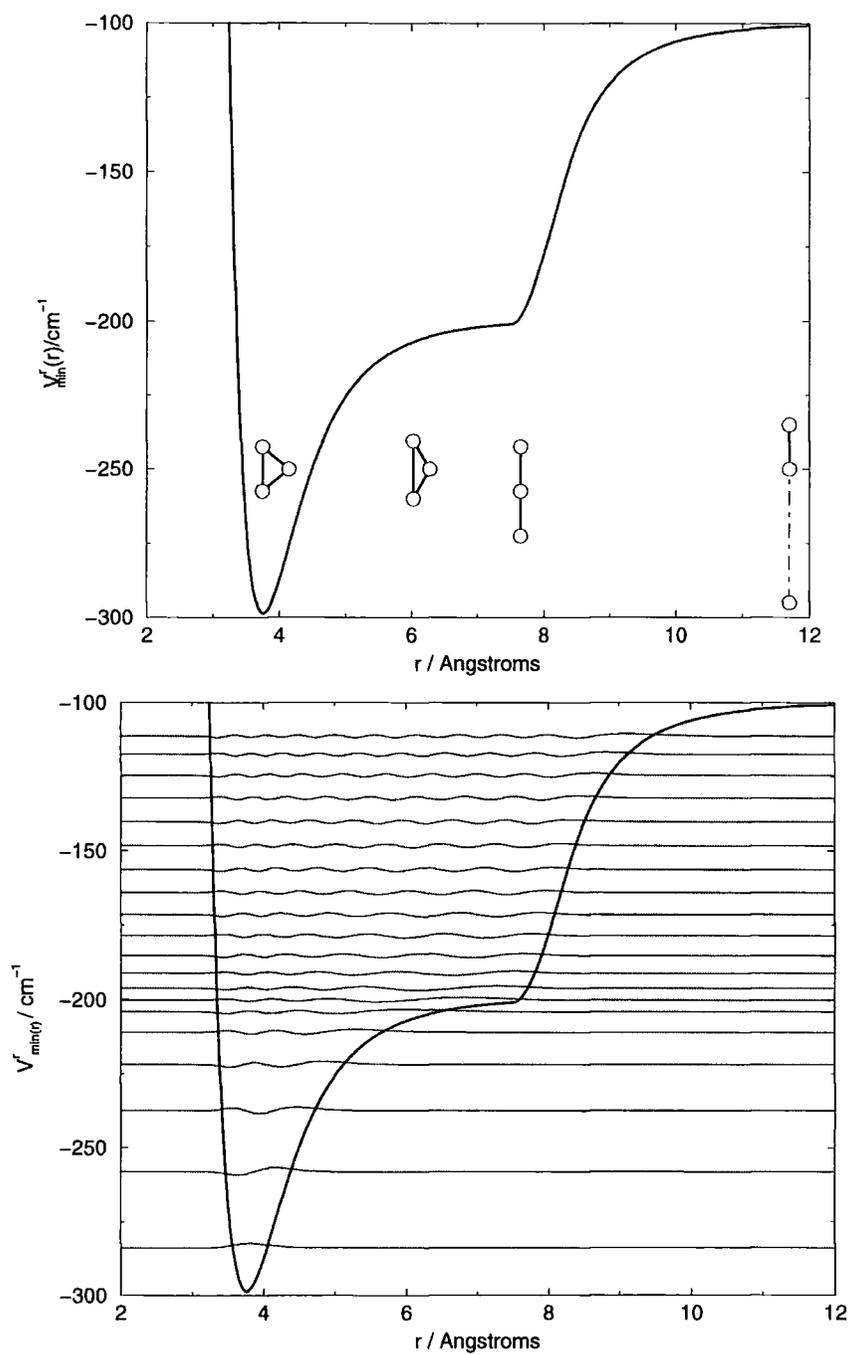
**Figure 4.5:** The cut through the potential for generating the potential-optimised functions in $r$ and some of the functions derived from it.

be zero at the origin. The only way for $R^{-1}\phi_i^R(R)$ to be finite or zero at $R = 0$ is if $\phi_i^R(R)$ is zero. It is possible to generate such functions that are either even or odd with respect to the transformation "$R \to -R$" [23] (though the concept of $R < 0$ is not meaningful for Jacobi coordinates as defined here). Mandelshtam and Taylor [23] found empirically that odd parity functions give the best convergence for the even $(A_1/E_s)$ symmetry block and even parity functions give the best convergence for the odd $(A_2/E_a)$ symmetry block.

The pairings may be explained as follows. In the even symmetry block, $\Psi(R, r, \theta)$ is finite at $R = 0$. To achieve this, $\lim_{R \to 0} R^{-1}\phi_i^R(R)$ must be finite, so that $\phi_i^R(R)$ itself must be linear in $R$ near the origin. This is achieved by generating basis functions $\phi_i^R(R)$ with a node at $R = 0$ but a finite derivative. These correspond to functions that are odd with respect to the transformation "$R \to -R$". Conversely, in the antisymmetric block, $\Psi(R, r, \theta)$ is zero at $R = 0$. To achieve this, $\lim_{R \to 0} R^{-1}\phi_i(R)$ must be zero, so that $\phi_i^R(R)$ itself must have a zero value *and derivative* at the origin. The simplest such functions are those that are quadratic in $R$ near the origin, which are even with respect to the transformation "$R \to -R$". The purpose of our 'centrifugal potential' now becomes clear. Apart from excluding an unwanted region of space it ensures that the basis functions in $R$ for the odd symmetry block have the correct properties. This is illustrated by figure 4.6. The transformation "$R \to -R$" appears to be the same as $\theta \to \pi - \theta$ and at first it is a little puzzling that the odd functions in $R$ should be paired with the even functions in $\theta$. However if one remembers that it is the symmetry properties of $R^{-1}\phi_i(R)$ that should be considered it becomes apparent that the pairings really are even/even and odd/odd.
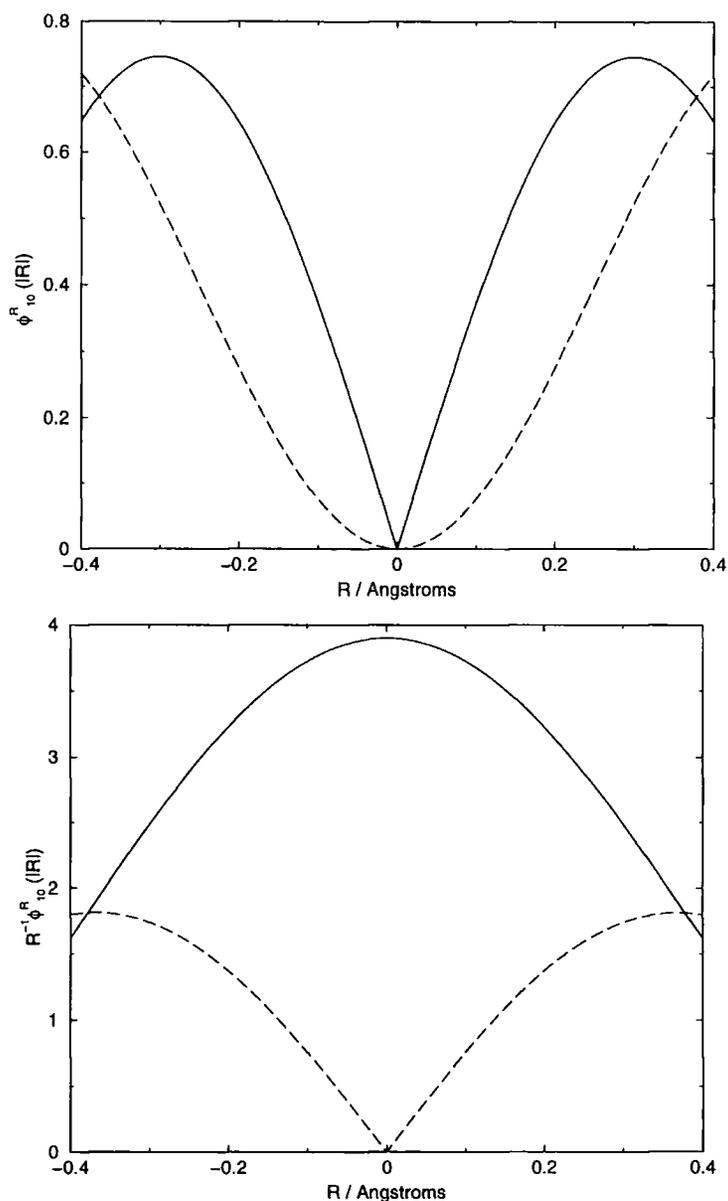
**Figure 4.6:** Graphs showing the 10th basis functions for the even and odd symmetry blocks. The solid line is the one for the even symmetry block and the dotted line is the one for the odd block. The solid line shows linear behaviour near the origin in the upper plot and in the lower plot has the correct properties of being finite with zero derivative. The dotted line shows quadratic behaviour in the upper plot and has zero value and finite derivative in the lower plot.

CHAPTER

---

# 5

# Calculating the bound states of Ar$_3$

---

The aim of this chapter is to describe the method used in this thesis to determine the bound states of the Ar$_3$ triatomic Van der Waals molecule. By testing my procedure for a converged calculation (to 0.01 cm$^{-1}$) of the first 30 or so energy levels in each symmetry block I hope to extend the method so that it will be able to calculate all the $J = 0$ energy levels of Ar$_3$.

## 5.1   Results

Having defined the potential-energy surface, the basis functions and the method of diagonalising the Hamiltonian matrix in chapters 3 and 4, the method of calculating the energy levels of Ar$_3$ can now be tested.

Firstly several parameters that are input to the program need to be determined by performing small test runs. The tests showed that the optimum value for $m$, the order of the polynomial used to precondition the matrix was 4, and the optimum value of $a_0$ was 800 cm$^{-1}$. The values of $R_{\min}$ and $R_{\max}$

| State Number | $A_1$ state/cm$^{-1}$ | | $E$ state/cm$^{-1}$ | |
|:---:|:---:|:---:|:---:|:---:|
| | NJW | RB | NJW | RB |
| 1 | $-254.895$ | $-254.891$ | $-232.378$ | $-232.373$ |
| 2 | $-224.294$ | $-224.290$ | $-211.833$ | $-211.826$ |
| 3 | $-211.955$ | $-211.950$ | $-205.044$ | $-205.036$ |
| 4 | $-198.254$ | $-198.242$ | $-195.398$ | $-195.389$ |
| 5 | $-193.528$ | $-185.992$ | $-187.604$ | $-184.268$ |

**Table 5.1:** A comparison of the calculations of the energy levels of Ar$_3$ obtained by me (NJW) and R. Bryan (RB) who performed coupled-channel calculations in a basis set of hyperspherical harmonics [32].

used in these trial runs were 0 Å and 7 Å respectively and the values of $r_{\mathrm{min}}$ and $r_{\mathrm{max}}$ were 3 Å and 9 Å respectively. These do not span a large enough range to converge all the energy levels but should be sufficient for my current purposes. To converge the lowest 29 energy levels to 0.01 cm$^{-1}$ the number of quadrature points required is 33 in $R$, 34 in $r$ and 30 in $\theta$.

My first aim was to reproduce the calculation of the lowest 10 energy levels of the even symmetry block performed on Ar$_3$ on the same potential energy surface by Bryan [32]. The comparison is shown in table 5.1 where there is generally good agreement except for the highest two states. The previous calculations were performed using the coupled channel method in a hyperspherical coordinate system. The tenth energy above the minimum is the roughly the limit of the hyperspherical method. To converge these energy levels to 0.1 cm$^{-1}$ 84 basis functions were need in the angular hyperspherical coordinate.

The convergence of the energy levels with respect to the number of quadrature points in each degree of freedom is described below. What should be observed here is a smooth decrease in the difference between the energy level and the previous one calculated with a smaller number of quadrature points. The energy levels may not converge towards a solution from above because a DVR calculation is not strictly variational, as explained by Wei [66].

| State No. | $\Gamma$ | Number of quadrature points in $\theta$ | | | | |
|---|---|---|---|---|---|---|
| | | 12 | 14 | 18 | 24 | 28 |
| 1 | $A_1$ | −254.681 | −254.855 | −254.894 | −254.895 | −254.895 |
| 1 | $E_s$ | −231.968 | −232.277 | −232.375 | −232.378 | −232.378 |
| | $E_a$ | −233.750 | −232.382 | −232.382 | −232.378 | −232.378 |
| 2 | $A_1$ | −223.716 | −224.146 | −224.290 | −224.294 | −224.294 |
| 3 | $A_1$ | −211.502 | −211.863 | −211.953 | −211.955 | −211.955 |
| 2 | $E_s$ | −211.043 | −211.662 | −211.829 | −211.833 | −211.833 |
| | $E_a$ | −214.624 | −211.860 | −211.860 | −211.834 | −211.834 |
| 3 | $E_s$ | −203.667 | −204.551 | −205.022 | −205.044 | −205.044 |
| | $E_a$ | −207.025 | −205.050 | −205.050 | −205.042 | −205.042 |
| 4 | $A_1$ | −196.555 | −197.690 | −198.239 | −198.254 | −198.254 |
| 4 | $E_s$ | −194.413 | −195.204 | −195.395 | −195.398 | −195.398 |
| | $E_a$ | −196.814 | −195.435 | −195.435 | −195.399 | −195.399 |
| 5 | $A_1$ | −192.666 | −193.333 | −193.524 | −193.528 | −193.528 |
| 1 | $A_2$ | −193.091 | −190.266 | −190.266 | −190.215 | −190.216 |
| 5 | $E_s$ | −187.009 | −187.476 | −187.598 | −187.604 | −187.604 |
| | $E_a$ | −190.778 | −187.637 | −187.637 | −187.609 | −187.610 |
| 6 | $A_1$ | −184.920 | −185.675 | −186.269 | −186.310 | −186.310 |
| 6 | $E_s$ | −182.036 | −183.410 | −184.267 | −184.306 | −184.306 |
| | $E_a$ | −186.245 | −184.353 | −184.353 | −184.306 | −184.306 |
| 7 | $A_1$ | −181.075 | −181.912 | −182.263 | −182.277 | −182.277 |
| 7 | $E_s$ | −178.380 | −179.324 | −179.941 | −179.984 | −179.984 |
| | $E_a$ | −182.219 | −180.020 | −180.020 | −179.984 | −179.984 |
| 8 | $A_1$ | −176.671 | −176.913 | −177.123 | −177.139 | −177.139 |
| 8 | $E_s$ | −176.102 | −176.724 | −176.978 | −176.983 | −176.983 |
| | $E_a$ | −178.621 | −177.001 | −177.001 | −176.982 | −176.982 |
| 9 | $A_1$ | −173.250 | −173.418 | −173.518 | −173.526 | −173.526 |
| 9 | $E_s$ | −173.175 | −173.364 | −173.427 | −173.435 | −173.435 |
| | $E_a$ | −175.028 | −173.440 | −173.440 | −173.433 | −173.433 |
| 10 | $A_1$ | −171.769 | −172.255 | −172.728 | −172.749 | −172.749 |
| 10 | $E_s$ | −171.691 | −171.991 | −172.420 | −172.426 | −172.426 |

| State No. | $\Gamma$ | Number of quadrature points in $\theta$ | | | | |
|---|---|---|---|---|---|---|
| | | 12 | 14 | 18 | 24 | 28 |
| | $E_a$ | −174.084 | −172.522 | −172.522 | −172.424 | −172.424 |
| 11 | $E_s$ | −170.633 | −171.646 | −171.789 | −171.794 | −171.794 |
| | $E_a$ | −173.173 | −171.804 | −171.804 | −171.793 | −171.793 |
| 11 | $A_1$ | −170.466 | −171.388 | −171.613 | −171.624 | −171.624 |
| 2 | $A_2$ | −172.055 | −171.338 | −171.338 | −171.208 | −171.208 |
| 12 | $E_s$ | −169.619 | −170.049 | −170.177 | −170.185 | −170.185 |
| | $E_a$ | −170.697 | −170.225 | −170.225 | −170.187 | −170.187 |
| 12 | $A_1$ | −169.343 | −169.679 | −169.812 | −169.826 | −169.826 |
| 13 | $E_s$ | −167.396 | −167.956 | −168.212 | −168.220 | −168.220 |
| | $E_a$ | −169.159 | −168.329 | −168.329 | −168.226 | −168.226 |
| 13 | $A_1$ | −166.967 | −167.677 | −167.876 | −167.882 | −167.882 |

**Table 5.2:** Convergence of the lowest 29 energy levels of Ar$_3$
with respect to the number of quadrature points in $\theta$.

The results for the $\theta$ coordinate show smooth convergence. The energy
levels from the even symmetry block of the Hamiltonian converge variation-
ally, from above, and those for the odd symmetry block converge from below.
As the calculations for the two symmetry blocks converge to the same place
the non-variational behaviour does not appear to affect the outcome of the
converged calculations. All of the energy levels in table 5.2 are converged
to the number of decimal places shown with 24 quadrature points in $\theta$. The
slight disagreement in the last decimal place between the odd and even block
calculations is probably due to the values of $R_{min}$, $R_{max}$, $r_{min}$ and $r_{max}$ chosen
which do not span a large enough range.

The results for the $r$ coordinate, shown in table 5.3, show smooth conver-
gence as a function of the number of quadrature points as well. However in
this case the energy levels from both symmetry blocks converge from below,
in a non-variational manner.

| State No. | $\Gamma$ | Number of quadrature points in $r$ | | | | |
|---|---|---|---|---|---|---|
| | | 18 | 20 | 22 | 26 | 30 |
| 1 | $A_1$ | −254.900 | −254.897 | −254.895 | −254.895 | −254.895 |
| 1 | $E_s$ | −232.414 | −232.393 | −232.383 | −232.379 | −232.378 |
| | $E_a$ | −232.383 | −232.380 | −232.379 | −232.378 | −232.378 |
| 2 | $A_1$ | −224.305 | −224.298 | −224.295 | −224.2938 | −224.294 |
| 3 | $A_1$ | −212.087 | −211.999 | −211.969 | −211.956 | −211.955 |
| 2 | $E_s$ | −211.890 | −211.867 | −211.849 | −211.835 | −211.833 |
| | $E_a$ | −211.856 | −211.844 | −211.838 | −211.835 | −211.835 |
| 3 | $E_s$ | −205.070 | −205.055 | −205.048 | −205.044 | −205.044 |
| | $E_a$ | −205.077 | −205.057 | −205.048 | −205.043 | −205.043 |
| 4 | $A_1$ | −198.321 | −198.281 | −198.265 | −198.256 | −198.254 |
| 4 | $E_s$ | −195.770 | −195.543 | −195.452 | −195.405 | −195.399 |
| | $E_a$ | −195.412 | −195.405 | −195.401 | −195.399 | −195.399 |
| 5 | $A_1$ | −193.646 | −193.577 | −193.546 | −193.530 | −193.528 |
| 1 | $A_2$ | −190.329 | −190.264 | −190.234 | −190.218 | −190.216 |
| 5 | $E_s$ | −187.836 | −187.698 | −187.640 | −187.608 | −187.604 |
| | $E_a$ | −187.676 | −187.638 | −187.621 | −187.611 | −187.610 |
| 6 | $A_1$ | −186.473 | −186.378 | −186.336 | −186.313 | −186.310 |
| 6 | $E_s$ | −184.645 | −184.435 | −184.352 | −184.311 | −184.306 |
| | $E_a$ | −184.352 | −184.324 | −184.313 | −184.307 | −184.305 |
| 7 | $A_1$ | −182.422 | −182.330 | −182.295 | −182.279 | −182.277 |
| 7 | $E_s$ | −180.039 | −180.005 | −179.992 | −179.985 | −179.985 |
| | $E_a$ | −180.026 | −180.001 | −179.990 | −179.985 | −179.984 |
| 8 | $A_1$ | −178.183 | −177.463 | −177.216 | −177.144 | −177.139 |
| 8 | $E_s$ | −177.095 | −177.079 | −177.048 | −176.993 | −176.984 |
| | $E_a$ | −176.999 | −176.989 | −176.985 | −176.982 | −176.982 |
| 9 | $A_1$ | −174.200 | −173.787 | −173.601 | −173.532 | −173.527 |
| 9 | $E_s$ | −173.504 | −173.489 | −173.473 | −173.442 | −173.435 |
| | $E_a$ | −173.457 | −173.441 | −173.436 | −173.434 | −173.433 |
| 10 | $A_1$ | −172.796 | −172.770 | −172.757 | −172.750 | −172.749 |
| 10 | $E_s$ | −172.485 | −172.451 | −172.436 | −172.427 | −172.426 |

| State No. | Γ | Number of quadrature points in $r$ | | | | |
|---|---|---|---|---|---|---|
| | | 18 | 20 | 22 | 26 | 30 |
| | $E_a$ | −172.937 | −172.628 | −172.500 | −172.433 | −172.425 |
| 11 | $E_s$ | −172.004 | −171.887 | −171.828 | −171.798 | −171.795 |
| | $E_a$ | −171.802 | −171.797 | −171.795 | −171.793 | −171.793 |
| 11 | $A_1$ | −171.662 | −171.646 | −171.634 | −171.625 | −171.624 |
| 2 | $A_2$ | −171.356 | −171.276 | −171.235 | −171.211 | −171.209 |
| 12 | $E_s$ | −170.476 | −170.315 | −170.233 | −170.191 | −170.186 |
| | $E_a$ | −170.197 | −170.191 | −170.188 | −170.187 | −170.187 |
| 12 | $A_1$ | −169.924 | −169.880 | −169.849 | −169.829 | −169.826 |
| 13 | $E_s$ | −168.393 | −168.281 | −168.244 | −168.223 | −168.220 |
| | $E_a$ | −168.245 | −168.234 | −168.229 | −168.226 | −168.226 |
| 13 | $A_1$ | −167.991 | −167.934 | −167.904 | −167.885 | −167.882 |

**Table 5.3:** Convergence of the lowest 29 energy levels of Ar₃ with respect to the number of quadrature points in $r$.

For both of these coordinates it is reasonable to expect smooth convergence for the higher lying states and apart from checking that this is the case no further attention needs to be paid to them.

For the $R$ coordinate things are a little more complicated. For small numbers of quadrature points in $R$, typically less than 30, the convergence is not a smooth function of the number of quadrature points. At some values of $N_R$ the energy is above the energy at convergence and at some points it is below. This behaviour occurs for all the states examined in this section but gets worse the higher the energy of the state. For larger numbers of quadrature points the convergence is much smoother. Figure 5.1 shows the convergence of some of the energy levels graphically.

This is quite a large problem. The unsmooth convergence means it will be very difficult to tell when a calculation has converged as it is not possible to determine whether the point is a 'blip' or not. In the calculations described here it is easy to extend the number of quadrature points until the 'blips' disappear. However for the final calculation of all the bound states this would
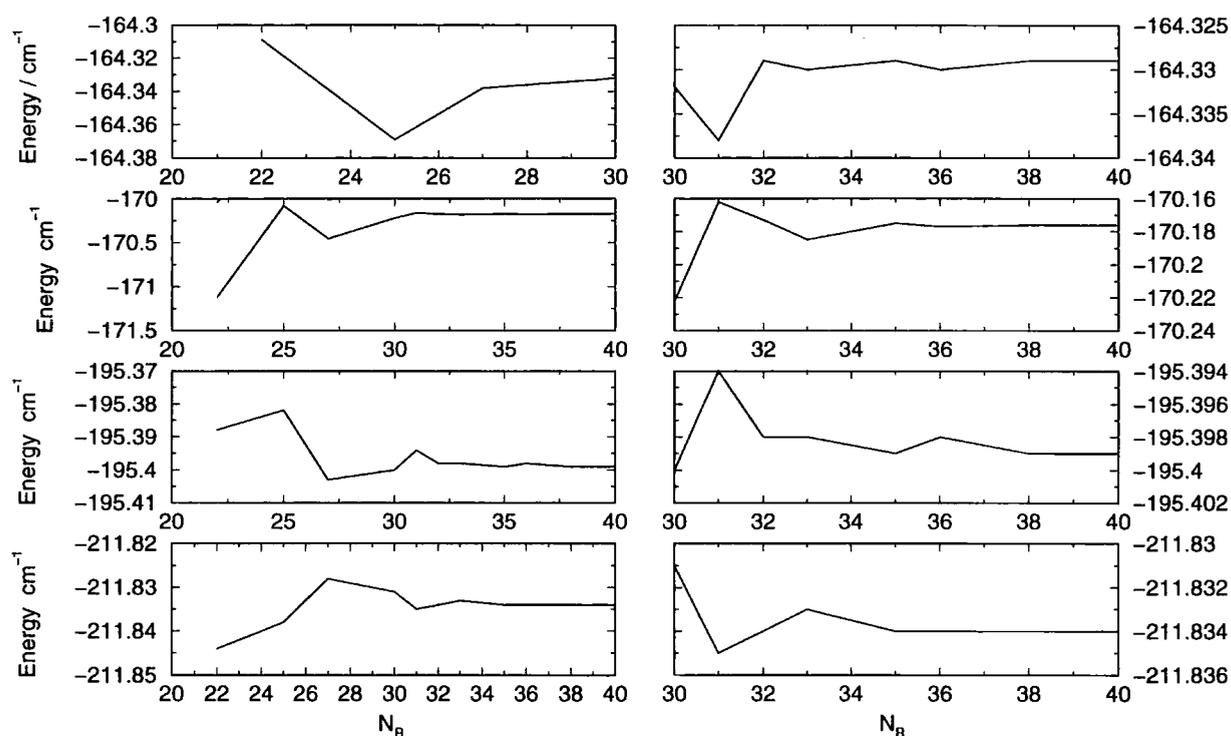
**Figure 5.1:** The convergence of four energy levels from the even block of the Hamiltonian matrix. The levels from the odd block show very similar properties. The left-hand column shows the convergence for 20-40 quadrature points, the right-hand column for 30-40. Note the different vertical scales on the graphs in the two columns.

very expensive computationally.

It transpired that this problem had been previously observed in calculations on the $H_3^+$ molecular ion [21, 67, 68]. In this study shifts of energy levels and unsmooth, non-variational convergence with increasing size of quadrature grid in $R$ was observed. The problem was traced to the DVR quadrature approximation to the $R^{-2}$ term in the angular kinetic energy operator, Eq. 3.5. To correct for this, the DVR representation of the $R^{-2}$ term was replaced in the calculation by its exact matrix elements which were obtained from an analytical formula. This produced a matrix that was not even nearly diagonal in the DVR. Once this had been done the calculation converged smoothly if a little more slowly. The basis functions used in the $H_3^+$ work, spherical oscillator functions, are based on Laguerre polynomials making it straightforward to derive an analytical formula for the integrals required [33]. In my calculation the basis functions are defined numerically and no such analytical formula will exist. The next section describes my solution to this problem.

## 5.2    The failure of the DVR quadrature approximation

The failure of the DVR quadrature approximation, which appears to be the cause of the unsmooth convergence described above, is a serious problem. To understand why the error occurs it is necessary to examine the nature of the quadrature approximation involved. A matrix element of the form is required

$$^{\text{DVR}}\tilde{R}_{\alpha'\alpha}^{-2} = \sum_{jj'} \langle x_{\alpha'}|\phi_{j'}\rangle\langle\phi_{j'}|\frac{\hbar^2}{2\mu_1 R^2}|\phi_j\rangle\langle\phi_j|x_\alpha\rangle \tag{5.1}$$

where $x_\alpha$ represents a DVR function, $\phi_j$ an FBR function and the $^{\text{DVR}}\tilde{R}_{\alpha'\alpha}^{-2}$ refers to the exact matrix elements of $R^{-2}$ in a DVR representation. In a DVR calculation this is approximated by the values of $\hbar^2/2\mu_1 R^2$ at the DVR grid points by substituting the following completeness relation into Eq. 5.1

$$\sum_{j=1}^{N} |\phi_j\rangle\langle\phi_j| = 1 \tag{5.2}$$

giving

$$^{\text{DVR}}\tilde{R}^{-2}_{\alpha'\alpha} = \langle x'_\alpha | \frac{\hbar^2}{2\mu_1 R^2} | x_\alpha \rangle$$

$$^{\text{DVR}}R^{-2}_{\alpha\alpha} \simeq \frac{\hbar^2}{2\mu_1 R^2_\alpha} \delta_{\alpha\alpha'} \tag{5.3}$$

The approximation is made in Eq. 5.3. The value of the matrix element is assumed to be equal to its value at the DVR quadrature point and is denoted $R^{-2}_{\alpha\alpha}$. It is at this point the error lies. The approximation made in Eq. 5.3 is simply invalid for small values of $R$. To prove this statement a series of calculations to examine the nature of the quadrature error have been performed. What should be compared is the difference between $\tilde{R}^{-2}_{\alpha'\alpha}$ and $R^{-2}_{\alpha\alpha}$. The matrix that represents the $R^{-2}$ operator in the DVR approximation, $R^{-2}_{\alpha\alpha}$, is diagonal by construction. The matrix that represents the exact solution, $\tilde{R}^{-2}_{\alpha'\alpha}$, will not be. Therefore the eigenvalues of this matrix will need to be determined to obtain a quantitative picture of the error and to compare the two methods. The magnitude of the off-diagonal elements of $\tilde{R}^{-2}_{\alpha'\alpha}$ can also be used as a guide. The larger they are the greater the deviation from the diagonal representation.

The numerical basis functions used here make the determination of the matrix elements of the exact solution quite straightforward. Firstly the FBR representation of the $R^{-2}$ operator must be computed,

$$^{\text{FBR}}\tilde{R}^{-2}_{j'j} = \langle \phi_{j'} | \frac{\hbar^2}{2\mu_1 R^2} | \phi_j \rangle. \tag{5.4}$$

This can be easily determined by numerical integration. The program already knows the value of the basis functions on a very fine grid in $R$ which makes the computation of the matrix elements of $^{\text{FBR}}\tilde{R}^{-2}_{j'j}$ simple. This matrix is then transformed to the DVR representation,

$$^{\text{DVR}}\tilde{R}^{-2}_{\alpha'\alpha} = {}^R T_{\alpha'j'} \cdot {}^{\text{FBR}}\tilde{R}^{-2}_{j'j} \cdot {}^R T_{\alpha j}, \tag{5.5}$$

and its eigenvalues determined.

The procedure used in the present work was as follows. Firstly a set of 40 basis functions of odd symmetry, i.e., with $L_{\min} = 0$, were generated in the range $2 \rightarrow 7$Å. These were used to obtain 40 DVR basis functions and their associated quadrature points. These were generated to see if it is the
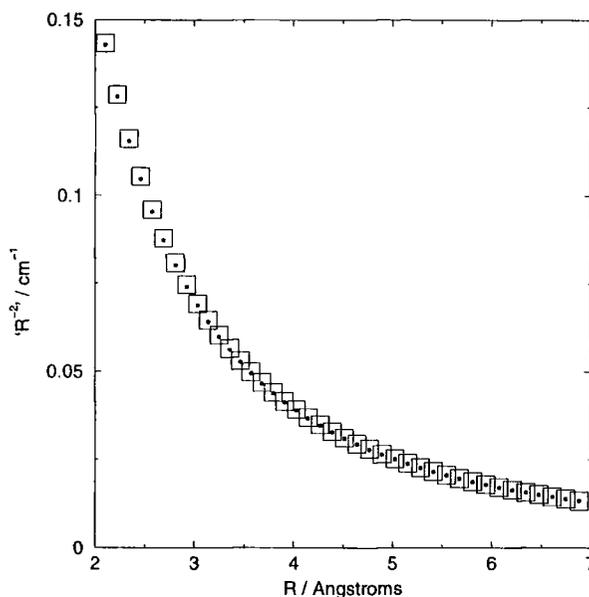
**Figure 5.2:** The eigenvalues of $^{\text{DVR}}\tilde{R}^{-2}$ (open squares) and the values of $^{\text{DVR}}R^{-2}$ (closed circles) in the range $R = 2 \rightarrow 7\text{Å}$.

area $R > 2\text{Å}$ that is causing the problem. The results of this calculation are shown in Fig. 5.2. The points lie almost exactly on top of each other which indicates that in this region the DVR quadrature approximation is a valid one. In this case the off-diagonal matrix elements of $^{\text{DVR}}\tilde{R}^{-2}$ are less than 0.1% of the diagonal elements.

The calculation was repeated, this time producing 40 quadrature points in the range $0 \rightarrow 7\text{Å}$. Figure 5.3 shows the results. The deviation of the exact result from the approximate one is quite obvious; the approximate result is always an underestimate. The disagreement gets larger for smaller values of $R$. At the quadrature point at $R = 0.06\text{Å}$ the exact result is a factor of three larger than the approximate one. The off-diagonal matrix elements of $^{\text{DVR}}\tilde{R}^{-2}_{\alpha\alpha'}$ reflect the error involved in assuming that the operator is diagonal. Part of the matrix is reproduced in table 5.4. The off-diagonal elements are of comparable magnitude to the diagonal ones, indicating that in this region the DVR quadrature approximation is failing.

All the above discussion relates to the basis functions in $R$ for the even symmetry block of the Hamiltonian. The $1/R^2$ potential that is used to generate the basis functions for the odd symmetry block ensures that they will not have as much amplitude as the functions for the even symmetry block in the
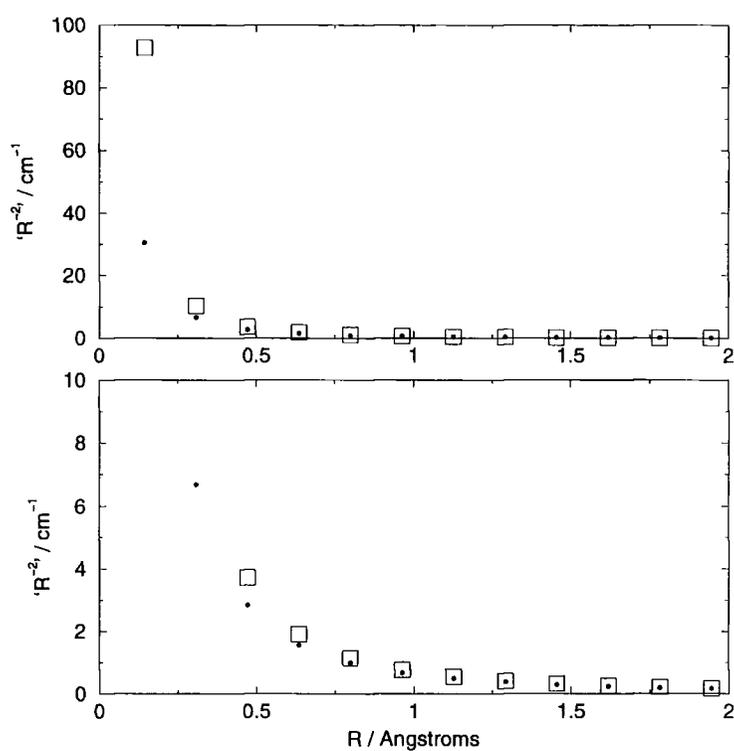
**Figure 5.3:** The eigenvalues of $^{\mathrm{DVR}}\tilde{R}^{-2}$ (open squares) and the values of $^{\mathrm{DVR}}R^{-2}$ (closed circles) in the range $R = 0 \rightarrow 2\text{Å}$. Note the different vertical scales on the two plots.

| $\alpha$ | $\alpha'$ | $^{\text{DVR}}\tilde{R}^{-2}_{\alpha\alpha'}$ | $^{\text{DVR}}R^{-2}_{\alpha\alpha'}$ |
|---|---|---|---|
| 1 | 1 | 30.56 | 78.91 |
| 1 | 2 | 0.00 | 20.97 |
| 1 | 3 | 0.00 | 13.31 |
| 1 | 4 | 0.00 | 9.72 |
| 1 | 5 | 0.00 | 7.65 |
| 2 | 2 | 6.68 | 15.62 |
| 2 | 3 | 0.00 | 5.63 |
| 2 | 4 | 0.00 | 4.10 |
| 2 | 5 | 0.00 | 3.21 |
| 3 | 3 | 2.84 | 6.38 |
| 3 | 4 | 0.00 | 2.57 |
| 3 | 5 | 0.00 | 2.01 |
| 4 | 4 | 1.57 | 3.43 |
| 4 | 5 | 0.00 | 1.46 |
| 5 | 5 | 0.99 | 2.13 |

**Table 5.4:** A comparison of the elements of the two symmetric matrices $^{\text{DVR}}\tilde{R}^{-2}_{\alpha\alpha'}$ and $^{\text{DVR}}R^{-2}_{\alpha\alpha'}$
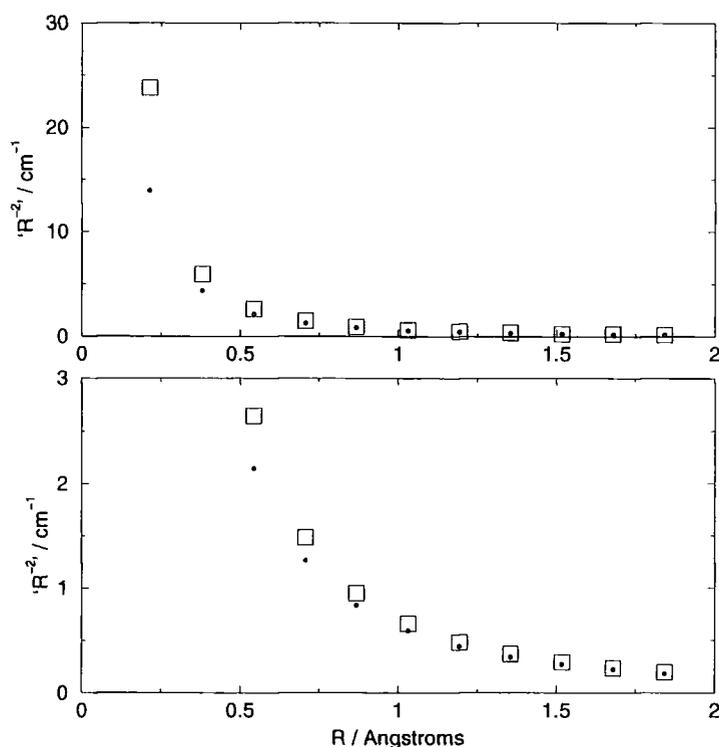
**Figure 5.4:** The same graph as 5.3 for the odd symmetry block. The eigenvalues of $^{\mathrm{DVR}}\tilde{R}^{-2}$ (open squares) and the values of $^{\mathrm{DVR}}R^{-2}$ (closed circles) in the range $R = 0 \to 2\text{Å}$. Note the different vertical scales on the two plots.

region close to $R = 0$. Therefore the potential-optimised quadrature points will not end up as close to $R = 0$ and the quadrature error will be smaller. This is illustrated by figure 5.4. The error is not negligible however and therefore calculations of the states in the odd symmetry block will be affected as well.

To correct for this effect the DVR approximation to the $R^{-2}$ operator must be replaced in the Hamiltonian by its exact form. The operator will no longer be diagonal in a DVR representation. The multiplication scheme for the Hamiltonian with the trial Lanczos vector, described in section 3.2, has to be modified to take account of this. Although the modification is very easy to implement, one do loop becomes two, it will slow the calculation down a little as some additional matrix elements are no longer identically equal to zero.

The convergence of the same four energy levels that were shown in figure 5.1 is illustrated for the corrected Hamiltonian in figure 5.5. Unsmooth convergence for small values of $N_R$ is still present. However for larger values of
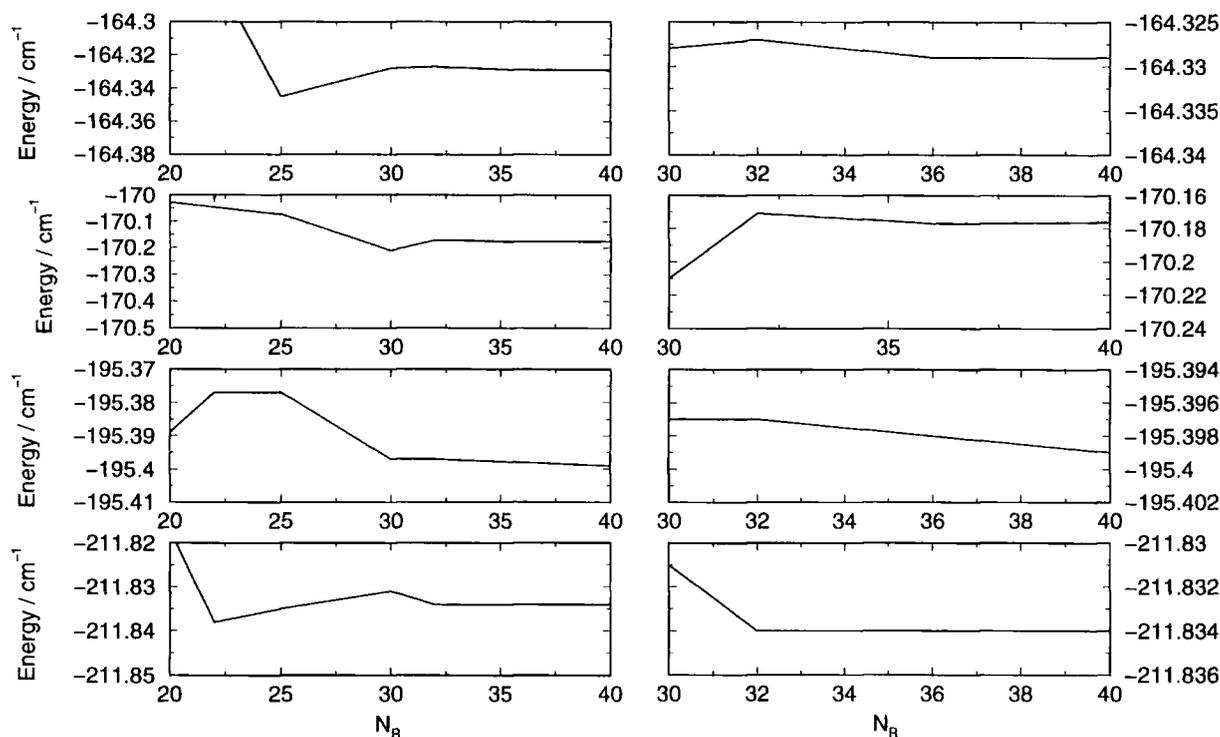
**Figure 5.5:** The convergence of four energy levels from the even block of the corrected Hamiltonian matrix.

$N_R$, nearer to convergence, the oscillatory behaviour has disappeared. This confirms that the source of my problem is the failure of the DVR quadrature approximation.

## 5.3  Linearity problem and large spectral range

As described in chapter 3 the rate of convergence of the Lanczos process towards a solution of the eigenvalue problem is inversely proportional to the range of the eigenvalue spectrum. The range of the eigenvalue spectrum is the difference between the largest and smallest eigenvalues. The smallest eigenvalue is, of course, the lowest energy level for that particular symmetry block. The highest eigenvalue however has no physical significance. It will be related to very large, unphysical, Hamiltonian matrix elements. These either correspond to a highly repulsive region of the potential-energy surface being included in the quadrature grid or to a very large value of one of the kinetic energy operators.

The obvious way to reduce the spectral range of the Hamiltonian matrix is to put an upper limit on the value of matrix elements. This has been implemented for the potential by Bramley et al. [22] and for the kinetic energy matrix elements by Mandelshtam and Taylor [23]. This upper limit must be chosen carefully. It must truncate the matrix elements so as to reduce the spectral range of the Hamiltonian matrix as much as possible without affecting the eigenvalues of interest.

To establish the best way to reduce the range of the eigenvalue spectrum for $Ar_3$, matrix elements contributing to the largest eigenvalues must first be identified. The potential energy operator is the most apparent source of large matrix elements. One solution to the problem is to define a upper limit for the potential energy matrix elements, $V_{ceil}$. Any matrix element that is calculated to be greater than $V_{ceil}$ is set equal to it. In their study on $H_3^+$, Bramley et al. [22] managed to reduce the highest eigenvalue from 958 000 $cm^{-1}$ to 326 000 $cm^{-1}$ by using a value of $V_{ceil}$ of 100 000 $cm^{-1}$. This affected the band origins by no more than 0.01 $cm^{-1}$ and speeded up the calculation by a factor of 1.7. Although the actual numbers for my $Ar_3$ calculation will be different this provides a rough guide to what is achievable using $V_{ceil}$.

The major difference between the calculation of Bramley et al. and mine is the type of Lanczos diagonaliser used. Their work was performed before the ARPACK [59, 60] codes were developed and they used an older set of routines due to Cullum and Willoughby [69]. These routines are only efficient at determining the eigenvalues of a matrix, not its eigenvectors. The determination of eigenvectors is a more expensive process computationally. However it is essential as it enables the calculation of the wave functions of $Ar_3$. Therefore it would be advantageous to be able to reduce the range of the eigenvalue spectrum much more than Bramley et al. to compensate for the extra expense involved in the computation of the eigenvectors.

The nature of the $Ar_3$ potential energy surface is such that for some values of $\theta$ a point defined by $R$ and $r$ is attractive whereas at another value of $\theta$ it is highly repulsive. In the Jacobi coordinate system both these points are treated equally but one of them will contribute a large unphysical energy to the Hamiltonian matrix. This aspect is well illustrated by considering the val-

| $V_{ceil}$/cm$^{-1}$ | Highest eigenvalue/$10^5$cm$^{-1}$ | CPU time | Error/cm$^{-1}$ |
|---|---|---|---|
| 50 | 1.209 | 1.00 | 0.039 |
| 100 | 1.209 | 1.00 | 0.038 |
| 1000 | 1.218 | 1.01 | 0.024 |
| 10000 | 1.308 | 1.02 | 0.008 |
| 100000 | 2.200 | 1.47 | 0.000 |
| 1000000 | 10.00 | 2.70 | 0.000 |
| no truncation | 72.10 | 8.72 | 0.000 |

**Table 5.5:** The effect of increasing the value of $V_{ceil}$, the potential energy cut-off parameter, upon the highest eigenvalue of the Hamiltonian matrix, the time taken to obtain the lowest 30 eigenvalues and the largest error in those eigenvalues.

ues of $R$ and $r$ at an equilateral triangle geometry where $\theta = 90°$. If the value of $\theta$ is gradually decreased, while $R$ and $r$ remain fixed, the potential gets more and more repulsive until at $0°$ two of the Ar atoms are almost on top of each other. Obviously this is a highly repulsive configuration and will produce a very large matrix element.

The effect of various values of $V_{ceil}$ upon the highest eigenvalue of the Hamiltonian matrix is shown in table 5.5. These test calculations were performed by determining the lowest thirty eigenvalues of the even symmetry block. The gain in the amount of computer time from the use of the $V_{ceil}$ parameter is very large. It takes over 8 times longer to obtain the eigenvalues of the Hamiltonian matrix constructed without its use compared to one that obtains essentially the same result.

The effect of $V_{ceil}$ on the eigenvalues shown here can only be used as a rough guide. It will have a greater effect upon the higher lying energy levels. However the results shown here do indicate that for the high lying states the value of $V_{ceil}$ should be varied in the range $10^5 \rightarrow 10^6$ cm$^{-1}$ to determine the optimum value.

As table 5.5 makes clear there is a certain value of $V_{ceil}$, around $10^5$ cm$^{-1}$, below which no significant decrease in the highest eigenvalue is observed.

The range of the eigenvalue spectrum at this point is comparable with that of Bramley *et al.* [22]. The very much slower decrease in the range of the eigenvalue spectrum from around $10^5$ cm$^{-1}$ onwards indicates that the remaining high-lying eigenvalues must be being influenced by the kinetic energy terms in the Hamiltonian. No further reduction in the spectral range is possible using $V_{\text{ceil}}$.

By examining the magnitude of the matrix elements it is possible to get an idea of which of the operators is causing the large eigenvalues. Such an examination indicated that it is the angular kinetic energy operator that is causing the problem. A Hamiltonian matrix element of the operator has the following form

$$\mathbf{H}_{\alpha\beta\gamma K}^{\alpha'\beta'\gamma'K'} = \frac{\hbar^2}{2}\left(\frac{1}{\mu_1 R_\alpha^2} + \frac{1}{\mu_2 r_\beta^2}\right)\sum_{j=0}^{N_\theta-1} j(j+1)^{\theta K}T_{\gamma',j}{}^{\theta K}T_{\gamma,j}\delta_{\alpha'\alpha}\delta_{\beta\beta'}\delta_{K'K} \quad (5.6)$$

The large matrix elements are generated when the value of $R$ is very small and the value of $j$ that was transformed to the DVR representation is very large. Such a high angular kinetic energy is obviously unphysical. As the $R$ coordinate becomes smaller the density of the quadrature points becomes greater. The very dense grid is able to represent very high angular momentum values and this is where the large matrix elements come from. A method of treating this problem has been implemented by Mandelshtam and Taylor [23] who based the idea on one used in a scattering calculation by Gögtas *et al.* [70].

The basic principle is the same as that implemented for the potential energy. An upper bound to the matrix elements of the kinetic energy operator is defined. Any matrix element above this limit is defined to be equal to it. To implement the cut off is a little more tricky than for the potential though. The truncation is done in the FBR by defining an $R$ and $r$ dependent variable $j_{\text{max}}(R,r)$. At each pair of values of $R$ and $r$ the summation in Eq. 5.6 is only carried out as far as $j_{\text{max}}(R,r)$.

Although this approach worked very well in the work of Mandelshtam and Taylor [23] it is even more difficult to apply in this work because of the non-diagonal nature of the $1/R^2$ operator, due to the correction outlined in the previous section. The application of it would destroy the separability of the

angular kinetic energy operator. For this reason it appears to be a bad idea to try to apply this method of truncation to the particular form of the Hamiltonian matrix used in this thesis.

What needs to be done therefore is to try and find a different way of reducing the spectral range of the Hamiltonian matrix. It seems however that any approach based upon limiting the values of the Hamiltonian matrix elements can only reduce the spectral range so far or will be very complex to implement.

The simplest and most elegant way to solve this problem is to use successive diagonalisation and truncation (SDT). By truncating the lower-dimensional Hamiltonians it should be possible to reduce the spectral range of the final Hamiltonian matrix as much as possible. To test this hypothesis an SDT algorithm has to be formulated. It should be designed bearing in mind the need for as small as possible spectral range and as small as possible final Hamiltonian matrix.

## 5.4   A combined SDT-Lanczos Algorithm

An SDT algorithm is defined by the coordinate ordering used and by whether a one or a two-stage truncation procedure is invoked. If a one-stage truncation procedure is chosen there is the additional possibility of diagonalising a series of 1D or 2D Hamiltonians.

The choice between a one-stage or a two-stage truncation procedure is relatively straightforward. For a two-stage procedure the matrix-vector multiplication step will involve a double transformation of the kinetic energy operator of the final coordinate to be diagonalised with respect to. For a one-stage procedure only one transformation is required. As the matrix-vector multiplication needs to be as efficient as possible, a single-stage transformation is preferred. This also appears to be the consensus in the literature. Both the study by Mussa *et al.* [51] and that by Wu and Hayes [62] use a one-stage truncation procedure.

Having chosen a one step truncation procedure the next choice is whether to diagonalise a 1D or a 2D Hamiltonian. If we diagonalise a 1D Hamilto-

nian the truncation procedure will only remove high-lying solutions of a one-dimensional operator and the potential. However this is likely to be less effective in reducing the final dimensions of the Hamiltonian matrix. The aim must be to try and truncate the matrix as much as possible before passing it to the Lanczos diagonaliser. If a series of 2D Hamiltonians are diagonalised it is possible to truncate the basis used in another degree of freedom leading to an greater reduction over all in the size of the final Hamiltonian. These considerations suggest that diagonalising a set of 2D Hamiltonians is the best approach.

At this point the procedures of Mussa *et al.* [51] and Wu and Hayes [62] diverge. Mussa *et al.* diagonalise a series of 2D Hamiltonians whereas Wu and Hayes diagonalise a series of 1D Hamiltonians. Neither set of authors gives a reason for their choice but are probably related to the memory available on each processor of the parallel machines the calculations were performed upon. This calculation is a serial one and therefore such matters do not need to be considered.

In their study of the choice of coordinate ordering for an SDT-DVR calculation Henderson *et al.* [56] found that for $H_3^+$ the optimum choice was $\theta$ first followed by $r$ then $R$. The fact that this choice performed best was attributed to the $R$ coordinate needing the largest amount of grid points. The similarities between $H_3^+$ and Ar₃ suggest that this will also be the optimum choice for Ar₃. However there is another factor involved in the decision.

The off-diagonal nature of the modified angular kinetic energy operator means that the operators associated with each coordinate are no longer diagonal in the other two coordinates. This complicates matters when constructing the Hamiltonian matrix using SDT. The angular kinetic energy matrix is now off-diagonal in $R$. This means if the scheme outlined by Henderson *et al.* was used only the diagonal terms (in $R$) of the angular kinetic energy operator could be included before any truncations were performed. Obviously this is an undesirable situation. The off-diagonal terms will contribute almost as much towards the large eigenvalue spectrum as the diagonal ones. Therefore not to be able to include them until after the truncation is performed will have a detrimental effect upon the efficiency of the Lanczos diagonaliser. A

major reason for introducing the SDT scheme is to truncate the large unphysical components of the angular kinetic energy matrix. It is essential therefore that the whole of the angular kinetic energy operator is present in the matrix that is truncated.

These considerations suggest that the matrix should be constructed in the order $\theta$, $R$ and $r$. At each grid point in $r$, a matrix of dimension $N_R \times N_\theta$ is constructed, diagonalised and truncated. This matrix is constructed from the kinetic energy matrices in the $R$ and $\theta$ coordinates and the potential,

$$
\begin{aligned}
^{2D}H_{\alpha\beta\gamma K}^{\alpha'\beta'\gamma'K'} &= {}^{R}d_{\alpha\alpha'}\delta_{\alpha\alpha'}\delta_{\beta\beta'}\delta_{KK'} + V_{\alpha\beta\gamma K}\delta_{\alpha\alpha'}\delta_{\beta\beta'}\delta_{\gamma\gamma'}\delta_{KK'} \\
&\quad + \frac{\hbar^2}{2}\left(\frac{1}{\mu_1 R_{\alpha\alpha'}^2} + \frac{1}{\mu_2 r_\beta^2}\right){}^{\theta K}d_{\gamma\gamma'}\delta_{\beta\beta'}\delta_{KK'} \\
&\equiv {}^{2D}h_{\alpha\alpha'\gamma\gamma'}\delta_{\beta\beta'}\delta_{KK'}.
\end{aligned}
\tag{5.7}
$$

The matrix $^{2D}\mathbf{h}$ is then diagonalised at each quadrature point in $r$ to give

$$
^{2D}\mathbf{h} = {}^{2D}C^{\beta K} \cdot {}^{2D}E^{\beta K} \cdot [{}^{2D}C^{\beta K}]^T
\tag{5.8}
$$

$^{2D}E^{\beta K}$ is a diagonal matrix containing the eigenvalues of $^{2D}\mathbf{h}$ and $^{2D}C^{\beta K}$ are the corresponding eigenvectors. The basis is then truncated using an energy cut-off condition, where $^{2D}E_l^{\beta K}$ represents the $l$th eigenvalue of $^{2D}\mathbf{h}$

$$
^{2D}E_l^{\beta K} < E_{\text{CUT}}^{2D}
\tag{5.9}
$$

In a SDT calculation such as the one described in chapter 2, the 3D Hamiltonian matrix would now be constructed from the kinetic energy matrix in $r$ and the truncated 2D eigenvectors $^{2D}\hat{C}^{\beta K}$

$$
^{3D}H_{l\beta K}^{l'\beta'K'} = {}^{2D}E_l^{\beta K}\delta_{\beta\beta'}\delta_{ll'} + \sum_{\alpha\alpha'\gamma\gamma'} {}^{2D}\hat{C}_{\alpha'\gamma'l'}^{\beta'K} \, {}^{r}d_{\beta\beta'} \, {}^{2D}\hat{C}_{\alpha\gamma l}^{\beta K}
\tag{5.10}
$$

However this matrix would be far too large to diagonalise in memory therefore a Lanczos diagonaliser is used. This requires only the computation of $y$, the product of the Hamiltonian matrix and a vector, $x$. This is achieved by multiplying the RHS of Eq. 5.10 by a vector $x$ sequentially

$$
u = {}^{2D}\hat{C}x
\tag{5.11}
$$

$$
v = {}^{r}\hat{d}u
\tag{5.12}
$$

$$
y = {}^{2D}\hat{C}v + {}^{2D}Ex
\tag{5.13}
$$

This procedure avoids the explicit construction of the 3D Hamiltonian matrix. The truncation procedure reduces the range of eigenvalue spectrum of $^{3D}H$ as much as possible which ensures the efficient operation of the Lanczos diagonaliser.

Having outlined an algorithm for combining SDT with a Lanczos diagonaliser the value of $E_{\text{CUT}}^{2D}$ must be determined. This has to be chosen with the same criteria used for the cut-off parameters described earlier. It must truncate the size of the Hamiltonian matrix as much as possible without affecting the eigenvalues.

For the $ArCO_2$ calculation presented in chapter 2, the value of the cut-off energy was determined to be approximately 400 cm$^{-1}$ to produce eigenvalues converged to 0.01 cm$^{-1}$. For the $Ar_3$ calculation the value needed is likely to be larger as there are many more bound states. To determine the value via a series of trial runs, similar to those used to determine $V_{\text{ceil}}$, to determine the lowest thirty energy levels proved rather difficult. Unfortunately the lowest 30 energy levels were stable to $1 \times 10^{-8}$ cm$^{-1}$ upon decreasing $E_{\text{CUT}}^{2D}$ from 10000 cm$^{-1}$ all the way down to 200 cm$^{-1}$. The results from the $ArCO_2$ calculation suggest that for the higher lying levels of $Ar_3$ a value of 200 cm$^{-1}$ will be way too small. What these calculations did illustrate however was the efficiency of the combined SDT Lanczos approach when compared with the diagonalisation of an uncontracted Hamiltonian matrix. The calculation with $E_{\text{CUT}}^{2D} = 400$ cm$^{-1}$ took two-thirds of the time of the uncontracted calculation. For a calculation of all the bound states the saving should be even greater.

Although the work is presented in this chapter as if it was performed in the order described this is not actually the case. All of the results described in the remainder of this thesis were obtained using an untruncated Hamiltonian matrix. It was not realised that the solution to the problem with the large range of the eigenvalue spectrum would be to use a truncated Hamiltonian matrix until very near the end of my PhD studies. So the actual way the value of $E_{\text{CUT}}^{2D}$ was determined was by comparison of the eigenvalues determined using the uncontracted calculations.

Although the results described in the following chapters were not obtained in an optimum manner it does not invalidate them in anyway. All that should

be remembered is that they could have been obtained far more efficiently using a combined SDT Lanczos approach.

CHAPTER

---
# 6

# Energy levels and wave functions of Ar₃
---

This chapter presents the results of my calculation of all the $J = 0$ wave functions and energy levels of $Ar_3$. The energy levels are classified in terms of a symmetry label and the wave functions are examined to reveal some of the dynamics of the $Ar_3$ Van der Waals molecule.

I have attempted to calculate the energy levels and wave functions for all $J = 0$ bound states of $Ar_3$. The DVR basis set was constructed using 34 points in $\theta$, 46 points in $R$ and 38 points in $r$. The 34 angular points with $\theta < 90°$ were taken from a 68-point Gauss-Legendre quadrature. The quadrature points in $R$ were obtained by applying the HEG procedure to 46 numerical basis functions, which were in turn obtained by integrating the one-dimensional Schrödinger equation (Eq. (4.6)) from $R = 0$ to 8 Å. The quadrature points in $r$ were obtained similarly, propagating from $r = 3$ to 10 Å.

# 6.1   Assigning the energy levels

Classification of the energy levels with a symmetry label is a relatively straightforward task to perform, especially for the first 100 or so levels. The symmetry-adapted calculation splits the Hamiltonian into two blocks. States that have $A_1$ symmetry appear in the even symmetry block and states that have A$_2$ symmetry appear in the odd symmetry block. The states of $E$ symmetry appear as a degenerate pair, one in the even symmetry block and one in the odd. Of course the calculation does not produce eigenvalues that are degenerate to machine precision. The agreement is of the order of 0.0001 cm$^{-1}$ for the lowest $E$ state and gets progressively worse the higher the energy level until at the dissociation limit it is about 0.05 cm$^{-1}$.

The states and their symmetry assignment are shown in table 6.1. Not all of the states can be unambiguously assigned with a symmetry label. If there is an $E$ state and an $A_1$ or $A_2$ state in one symmetry block that are degenerate to within the convergence limit of the calculation it is not possible to assign either of them definitively on the basis of energies alone. Under these circumstances a ? is placed by the assignment in the table. Close to the dissociation limit the high density of states makes the situation even worse and at this point the symmetry labelling of the states almost certainly contains some errors. It is possible to use the wavefunction plots shown later in this chapter to assist the symmetry assignments but this has not been attempted here.

| $\Gamma$ | $n$ | $A_1/E$ $E_n$/cm$^{-1}$ | $A_2/E$ $E_n$/cm$^{-1}$ | $n$ |
|---|---|---|---|---|
| $A_1$ | 1 | −254.89 | | |
| $E$ | 2 | −232.38 | −232.38 | 1 |
| $A_1$ | 3 | −224.29 | | |
| $A_1$ | 4 | −211.95 | | |
| $E$ | 5 | −211.83 | −211.83 | 2 |
| $E$ | 6 | −205.04 | −205.04 | 3 |
| $A_1$ | 7 | −198.25 | | |
| $E$ | 8 | −195.40 | −195.40 | 4 |

| $\Gamma$ | $n$ | $A_1/E$ $E_n/\mathrm{cm}^{-1}$ | $A_2/E$ $E_n/\mathrm{cm}^{-1}$ | $n$ |
|---|---|---|---|---|
| $A_1$ | 9 | −193.53 | | |
| $A_2$ | | | −190.22 | 5 |
| $E$ | 10 | −187.61 | −187.61 | 6 |
| $A_1$ | 11 | −186.31 | | |
| $E$ | 12 | −184.31 | −184.31 | 7 |
| $A_1$ | 13 | −182.28 | | |
| $E$ | 14 | −179.98 | −179.98 | 8 |
| $A_1$ | 15 | −177.14 | | |
| $E$ | 16 | −176.98 | −176.98 | 9 |
| $A_1$ | 17 | −173.52 | | |
| $E$ | 18 | −173.43 | −173.43 | 10 |
| $A_1$ | 19 | −172.75 | | |
| $E$ | 20 | −172.42 | −172.42 | 11 |
| $E$ | 21 | −171.79 | −171.79 | 12 |
| $A_1$ | 22 | −171.61 | | |
| $A_2$ | | | −171.21 | 13 |
| $E$ | 23 | −170.18 | −170.18 | 14 |
| $A_1$ | 24 | −169.81 | | |
| $E$ | 25 | −168.21 | −168.21 | 15 |
| $A_1$ | 26 | −167.88 | | |
| $A_1$ | 27 | −166.56 | | |
| $E$ | 28 | −166.17 | −166.17 | 16 |
| $E$ | 29 | −164.33 | −164.33 | 17 |
| $A_1$ | 30 | −163.60 | | |
| $E$ | 31 | −163.25 | −163.25 | 18 |
| $A_1$ | 32 | −161.81 | | |
| $E$ | 33 | −161.14 | −161.14 | 19 |
| $A_1$ | 34 | −160.01 | | |
| $A_2$ | | | −159.64 | 20 |
| $E$ | 35 | −159.50 | −159.50 | 21 |
| $E$ | 36 | −158.26 | −158.27 | 22 |

| $\Gamma$ | $n$ | $A_1/E$ $E_n/\text{cm}^{-1}$ | $A_2/E$ $E_n/\text{cm}^{-1}$ | $n$ |
|---|---|---|---|---|
| $A_1$ | 37 | −157.06 | | |
| $E$ | 38 | −155.53 | −155.53 | 23 |
| $A_1$ | 39 | −154.80 | | |
| $E$ | 40 | −154.50 | −154.50 | 24 |
| $A_2$ | | | −153.41 | 25 |
| $E$ | 41 | −153.33 | −153.33 | 26 |
| $A_1$ | 42 | −152.26 | | |
| $E$ | 43 | −152.09 | −152.09 | 27 |
| $A_1$ | 44 | −151.99 | | |
| $E$ | 45 | −151.87 | −151.87 | 28 |
| $E$ | 46 | −151.05 | −151.05 | 29 |
| $A_1$ | 47 | −150.42 | | |
| $E$ | 48 | −150.37 | −150.37 | 30 |
| $A_2$ | | | −149.98 | 31 |
| $A_1$ | 49 | −149.43 | | |
| $E$ | 50 | −149.08 | −149.08 | 32 |
| $A_1$ | 51 | −148.02 | | |
| $E$ | 52 | −147.74 | −147.75 | 33 |
| $A_1$ | 53 | −147.67 | | |
| $E$ | 54 | −146.58 | −146.58 | 34 |
| $A_1$ | 55 | −146.51 | | |
| $E$ | 56 | −145.85 | −145.85 | 35 |
| $A_2$ | | | −145.82 | 36 |
| $A_1$ | 57 | −145.37 | | |
| $E$ | 58 | −144.64 | −144.64 | 37 |
| $A_1$ | 59 | −144.12 | | |
| $E$ | 60 | −144.07 | −144.07 | 38 |
| $E$ | 61 | −143.23 | −143.24 | 39 |
| $A_2$ | | | −142.79 | 40 |
| $E$ | 62 | −142.61 | −142.61 | 41 |
| $A_1$ | 63 | −141.92 | | |

| Γ | n | $A_1/E$ $E_n/\text{cm}^{-1}$ | $A_2/E$ $E_n/\text{cm}^{-1}$ | n | |
|---|---|---|---|---|---|
| $E$ | 64 | −141.15 | −141.15 | 42 | |
| $A_2$ | | | −140.93 | 43 | |
| $E$ | 65 | −140.88 | −140.88 | 44 | |
| $A_1$ | 66 | −140.13 | | | |
| $E$ | 67 | −139.92 | −139.92 | 45 | |
| $A_2$ | | | −139.26 | 46 | |
| $A_1$ | 68 | −139.18 | | | |
| $E$ | 69 | −139.16 | −139.17 | 47 | ? |
| $E$ | 70 | −138.94 | −138.94 | 48 | |
| $A_1$ | 71 | −138.52 | | | |
| $E$ | 72 | −138.14 | −138.14 | 49 | |
| $A_2$ | | | −137.51 | 50 | |
| $E$ | 73 | −136.96 | −136.96 | 51 | |
| $E$ | 74 | −135.96 | −135.96 | 52 | |
| $A_1$ | 75 | −135.57 | | | |
| $E$ | 76 | −135.52 | −135.52 | 53 | |
| $A_2$ | | | −135.45 | 54 | |
| $A_1$ | 77 | −134.78 | | | |
| $E$ | 78 | −134.29 | −134.29 | 55 | |
| $E$ | 79 | −134.17 | −134.16 | 56 | |
| $A_1$ | 80 | −134.14 | | | |
| $A_1$ | 81 | −133.51 | | | |
| $E$ | 82 | −132.88 | −132.88 | 57 | |
| $E$ | 83 | −132.80 | −132.80 | 58 | |
| $E$ | 84 | −132.48 | −132.48 | 59 | |
| $E$ | 85 | −132.20 | −132.20 | 60 | |
| $E$ | 86 | −131.73 | −131.72 | 61 | |
| $A_1$ | 87 | −131.43 | | | |
| $A_1$ | 88 | −130.84 | | | |
| $E$ | 89 | −130.76 | −130.75 | 62 | ? |
| $A_2$ | | | −130.75 | 63 | |

| $\Gamma$ | $n$ | $A_1/E$ $E_n/\mathrm{cm}^{-1}$ | $A_2/E$ $E_n/\mathrm{cm}^{-1}$ | $n$ | |
|---|---|---|---|---|---|
| $E$ | 90 | −130.16 | −130.17 | 64 | |
| $A_1$ | 91 | −129.68 | | | |
| $E$ | 92 | −128.85 | −128.85 | 65 | |
| $E$ | 93 | −128.72 | −128.68 | 66 | |
| $E$ | 94 | −128.64 | −128.63 | 67 | |
| $A_2$ | | | −128.23 | 68 | |
| $E$ | 95 | −128.07 | −128.08 | 69 | |
| $A_1$ | 96 | −127.75 | | | |
| $E$ | 97 | −127.13 | −127.13 | 70 | |
| $E$ | 98 | −126.76 | −126.77 | 71 | |
| $A_1$ | 99 | −126.70 | | | |
| $E$ | 100 | −126.47 | −126.46 | 72 | |
| $A_2$ | | | −126.36 | 73 | |
| $A_1$ | 101 | −125.86 | | | |
| $E$ | 102 | −125.81 | −125.81 | 74 | |
| $A_2$ | | | −125.65 | 75 | |
| $E$ | 103 | −125.57 | −125.57 | 76 | |
| $A_1$ | 104 | −125.47 | | | |
| $E$ | 105 | −125.06 | −125.06 | 77 | |
| $A_2$ | | | −124.80 | 78 | |
| $E$ | 106 | −124.61 | −124.62 | 79 | |
| $E$ | 107 | −124.37 | −124.36 | 80 | ? |
| $A_1$ | 108 | −124.35 | | | |
| $A_2$ | | | −124.17 | 81 | |
| $E$ | 109 | −123.83 | −123.83 | 82 | |
| $A_1$ | 110 | −123.53 | | | |
| $E$ | 111 | −123.20 | −123.22 | 83 | |
| $A_2$ | | | −122.88 | 84 | |
| $E$ | 112 | −122.77 | −122.77 | 85 | |
| $A_1$ | 113 | −122.00 | | | |
| $E$ | 114 | −121.81 | −121.82 | 86 | |

| $\Gamma$ | $n$ | $A_1/E$ $E_n/\text{cm}^{-1}$ | $A_2/E$ $E_n/\text{cm}^{-1}$ | $n$ |
|---|---|---|---|---|
| $E$ | 115 | –121.33 | –121.33 | 87 |
| $A_1$ | 116 | –121.06 | | |
| $A_2$ | | | –120.86 | 88 |
| $E$ | 117 | –120.83 | –120.84 | 89 |
| $A_1$ | 118 | –119.97 | | |
| $E$ | 119 | –119.66 | –119.65 | 90 |
| $E$ | 120 | –119.57 | –119.58 | 91 |
| $A_2$ | | | –119.55 | 92 |
| $A_1$ | 121 | –119.44 | | |
| $E$ | 122 | –119.16 | –119.15 | 93 |
| $E$ | 123 | –119.08 | –119.08 | 94 |
| $A_1$ | 124 | –118.92 | | |
| $E$ | 125 | –118.68 | –118.69 | 95 |
| $A_1$ | 126 | –118.52 | | |
| $E$ | 127 | –117.79 | –117.80 | 96 |
| $A_2$ | | | –117.61 | 97 |
| $E$ | 128 | –117.42 | –117.41 | 98 |
| $A_1$ | 129 | –117.39 | | |
| $A_1$ | 130 | –117.27 | | |
| $E$ | 131 | –117.05 | –117.05 | 99 |
| $E$ | 132 | –116.30 | –116.28 | 100 |
| $A_1$ | 133 | –116.26 | | |
| $A_2$ | | | –116.15 | 101 |
| $E$ | 134 | –115.98 | –116.00 | 102 |
| $A_1$ | 135 | –115.47 | | |
| $E$ | 136 | –115.26 | –115.27 | 103 |
| $A_2$ | | | –115.21 | 104 |
| $E$ | 137 | –115.17 | –115.16 | 105 |
| $A_1$ | 138 | –114.93 | | |
| $E$ | 139 | –114.75 | –114.76 | 106 |
| $E$ | 140 | –114.04 | –114.04 | 107 |

| $\Gamma$ | $n$ | $A_1/E$ $E_n/\mathrm{cm}^{-1}$ | $A_2/E$ $E_n/\mathrm{cm}^{-1}$ | $n$ | |
|---|---|---|---|---|---|
| $A_1$ | 141 | −113.85 | | | |
| $E$ | 142 | −113.72 | −113.71 | 108 | |
| $E$ | 143 | −113.62 | −113.62 | 109 | |
| $A_2$ | | | −113.62 | 110 | ? |
| $E$ | 144 | −113.53 | | | |
| $E$ | 145 | −113.22 | −113.22 | 111 | |
| $E$ | 146 | −113.11 | −113.14 | 112 | |
| $E$ | 147 | −112.67 | −112.67 | 113 | |
| $A_1$ | 148 | −112.48 | | | |
| $E$ | 149 | −112.46 | −112.46 | 114 | |
| $E$ | 150 | −112.17 | −112.17 | 115 | |
| $E$ | 151 | −112.08 | −112.08 | 116 | |
| $E$ | 152 | −112.07 | −112.07 | 117 | |
| $A_1$ | 153 | −112.05 | | | |
| $E$ | 154 | −111.77 | −111.77 | 118 | |
| $A_2$ | | | −111.66 | 119 | |
| $A_1$ | 155 | −111.28 | | | |
| $E$ | 156 | −111.18 | −111.16 | 120 | |
| $A_1$ | 157 | −110.95 | | | |
| $E$ | 158 | −110.86 | −110.87 | 121 | |
| $E$ | 159 | −110.46 | −110.46 | 122 | |
| $A_2$ | | | −110.37 | 123 | |
| $E$ | 160 | −110.11 | −110.11 | 124 | |
| $E$ | 161 | −109.90 | −109.89 | 125 | |
| $A_1$ | 162 | −109.86 | | | |
| $E$ | 163 | −109.70 | −109.71 | 126 | |
| $A_2$ | | | −109.33 | 127 | |
| $A_1$ | 164 | −109.20 | | | |
| $E$ | 165 | −108.78 | −108.78 | 128 | |
| $E$ | 166 | −108.58 | −108.58 | 129 | |
| $A_2$ | | | −108.58 | 130 | ? |

| $\Gamma$ | $n$ | $A_1/E$ $E_n/\text{cm}^{-1}$ | $A_2/E$ $E_n/\text{cm}^{-1}$ | $n$ | |
|---|---|---|---|---|---|
| $A_1$ | 167 | −108.50 | | | |
| $E$ | 168 | −107.96 | −107.98 | 131 | |
| $E$ | 169 | −107.79 | −107.79 | 132 | |
| $E$ | 170 | −107.75 | −107.73 | 133 | |
| $E$ | 171 | −107.36 | −107.36 | 134 | |
| $A_1$ | 172 | −107.31 | | | |
| $E$ | 173 | −107.24 | −107.25 | 135 | |
| $E$ | 174 | −106.48 | −106.48 | 136 | |
| $A_1$ | 175 | −106.45 | | | |
| $A_2$ | | | −106.31 | 137 | |
| $E$ | 176 | −106.29 | −106.29 | 138 | |
| $A_1$ | 177 | −106.19 | | | |
| $E$ | 178 | −106.17 | −106.17 | 139 | |
| $A_1$ | 179 | −105.98 | | | |
| $E$ | 180 | −105.90 | −105.91 | 140 | |
| $A_2$ | | | −105.82 | 141 | |
| $E$ | 181 | −105.80 | −105.82 | 142 | ? |
| $E$ | 182 | −105.52 | −105.51 | 143 | |
| $A_1$ | 183 | −105.30 | | | |
| $A_2$ | | | −105.05 | 144 | |
| $E$ | 184 | −104.83 | −104.84 | 145 | |
| $A_1$ | 185 | −104.72 | | | |
| $E$ | 186 | −104.40 | −104.42 | 146 | |
| $E$ | 187 | −104.34 | −104.34 | 147 | |
| $A_1$ | 188 | −104.27 | | | |
| $A_2$ | | | −104.13 | 148 | |
| $E$ | 189 | −104.01 | −103.99 | 149 | |
| $A_1$ | 190 | −103.97 | | | |
| $E$ | 191 | −103.56 | −103.58 | 150 | |
| $E$ | 192 | −103.30 | −103.31 | 151 | |
| $A_1$ | 193 | −103.25 | | | |

| Γ | n | $A_1/E$ $E_n/\mathrm{cm}^{-1}$ | $A_2/E$ $E_n/\mathrm{cm}^{-1}$ | n |
|---|---|---|---|---|
| $A_2$ | | | −103.10 | 152 |
| $E$ | 194 | −103.08 | −103.07 | 153 |
| $A_1$ | 195 | −102.95 | | |
| $E$ | 196 | −102.33 | −102.34 | 154 |
| $A_1$ | 197 | −102.16 | | |
| $E$ | 198 | −102.07 | −102.06 | 155 |
| $E$ | 199 | −102.01 | −102.00 | 156 |
| $A_2$ | | | −101.93 | 157 |
| $A_1$ | 200 | −101.77 | | |
| $E$ | 201 | −101.66 | −101.67 | 158 |
| $E$ | 202 | −101.37 | −101.38 | 159 |
| $A_2$ | | | −101.36 | 160 |
| $E$ | 203 | −101.17 | −101.16 | 161 |
| $A_1$ | 204 | −101.01 | | |
| $A_2$ | | | −100.93 | 162 |
| $E$ | 205 | −100.82 | −100.82 | 163 |
| $E$ | 206 | −100.53 | −100.53 | 164 |
| $E$ | 207 | −100.31 | −100.30 | 165 |
| $E$ | 208 | −100.28 | −100.28 | 166 |
| $E$ | 209 | −100.03 | −100.05 | 167 |
| $E$ | 210 | −99.89 | −99.90 | 168 |
| $E$ | 211 | −99.75 | −99.74 | 169 |
| $A_1$ | 212 | −99.54 | | |
| $E$ | 213 | −99.49 | −99.49 | 170 |
| $E$ | 214 | −99.39 | −99.38 | 171 |
| $E$ | 215 | −99.29 | −99.30 | 172 |
| $A_1$ | 216 | −99.25 | | |
| $A_2$ | | | −99.20 | 173 |
| $E$ | 217 | −98.87 | −98.87 | 174 |
| $A_1$ | 218 | −98.76 | | |
| $E$ | 219 | −98.58 | −98.60 | 175 |

| | | $A_1/E$ | $A_2/E$ | | |
|---|---|---|---|---|---|
| $\Gamma$ | $n$ | $E_n$/cm$^{-1}$ | $E_n$/cm$^{-1}$ | $n$ | |
| $A_2$ | | | −98.35 | 176 | |
| $E$ | 220 | −98.25 | −98.26 | 177 | |
| $E$ | 221 | −98.04 | −98.04 | 178 | |
| $E$ | 222 | −98.00 | −98.00 | 179 | |
| $A_1$ | 223 | −97.96 | | | |
| $E$ | 224 | −97.89 | −97.86 | 180 | |
| $A_1$ | 225 | −97.62 | | | |
| $E$ | 226 | −97.61 | −97.61 | 181 | |
| $E$ | 227 | −97.41 | −97.41 | 182 | |
| $A_2$ | | | −97.40 | 183 | ? |
| $A_1$ | 228 | −97.10 | | | |
| $E$ | 229 | −97.02 | −97.03 | 184 | |
| $E$ | 230 | −96.66 | −96.64 | 185 | |
| $E$ | 231 | −96.60 | −96.59 | 186 | |
| $E$ | 232 | −96.57 | −96.56 | 187 | |
| $A_1$ | 233 | −96.28 | | | |
| $E$ | 234 | −96.24 | −96.23 | 188 | |
| $E$ | 235 | −96.08 | −96.07 | 189 | |
| $A_1$ | 236 | −96.06 | | | ? |
| $A_1$ | 237 | −95.93 | | | |
| $E$ | 238 | −95.75 | −95.77 | 190 | |
| $A_2$ | | | −95.62 | 191 | |
| $E$ | 239 | −95.54 | −95.56 | 192 | |
| $E$ | 240 | −95.35 | −95.39 | 193 | |
| $A_1$ | 241 | −95.19 | | | |
| $A_2$ | | | −95.07 | 194 | |
| $E$ | 242 | −94.97 | −94.98 | 195 | |
| $A_2$ | | | −94.94 | 196 | |
| $E$ | 243 | −94.83 | −94.82 | 197 | |
| $A_1$ | 244 | −94.81 | | | ? |
| $A_2$ | | | −94.75 | 198 | |

| $\Gamma$ | $n$ | $A_1/E$<br>$E_n/\text{cm}^{-1}$ | $A_2/E$<br>$E_n/\text{cm}^{-1}$ | $n$ | |
|---|---|---|---|---|---|
| $A_1$ | 245 | –94.74 | | | |
| $E$ | 246 | –94.68 | –94.64 | 199 | |
| $A_1$ | 247 | –94.61 | | | |
| $A_1$ | 248 | –94.48 | | | |
| $E$ | 249 | –94.28 | –94.30 | 200 | |
| $E$ | 250 | –93.69 | –93.63 | 201 | ? |
| $A_1$ | 251 | –93.69 | | | |
| $A_2$ | | | –93.63 | 202 | |
| $E$ | 252 | –93.54 | –93.56 | 203 | |
| $A_2$ | | | –93.55 | 204 | ? |
| $A_1$ | 253 | –93.49 | | | |
| $A_2$ | | | –93.45 | 205 | |
| $A_2$ | | | –93.41 | 206 | |
| $E$ | 254 | –93.13 | –93.13 | 207 | |
| $A_1$ | 255 | –93.06 | | | |
| $E$ | 256 | –92.93 | –92.93 | 208 | |
| $A_2$ | | | –92.91 | 209 | |
| $A_1$ | 257 | –92.84 | | | |
| $E$ | 258 | –92.69 | –92.68 | 210 | |
| $E$ | 259 | –92.55 | –92.56 | 211 | |
| $E$ | 260 | –92.39 | –92.38 | 212 | |
| $A_1$ | 261 | –92.27 | | | |
| $E$ | 262 | –92.07 | –92.03 | 213 | |
| $E$ | 263 | –91.90 | –91.91 | 214 | |
| $E$ | 264 | –91.85 | –91.88 | 215 | |
| $A_2$ | | | –91.77 | 216 | |
| $E$ | 265 | –91.74 | –91.72 | 217 | |
| $E$ | 266 | –91.38 | –91.34 | 218 | |
| $E$ | 267 | –91.27 | –91.29 | 219 | |
| $E$ | 268 | –91.26 | –91.26 | 220 | |
| $A_1$ | 269 | –91.04 | | | |

| $\Gamma$ | $n$ | $A_1/E$ $E_n/\text{cm}^{-1}$ | $A_2/E$ $E_n/\text{cm}^{-1}$ | $n$ | |
|---|---|---|---|---|---|
| $E$ | 270 | −91.03 | −91.03 | 221 | |
| $A_1$ | 271 | −90.99 | | | |
| $A_2$ | | | −90.90 | 222 | |
| $E$ | 272 | −90.83 | −90.83 | 223 | |
| $A_1$ | 273 | −90.75 | | | |
| $E$ | 274 | −90.73 | −90.71 | 224 | |
| $A_1$ | 275 | −90.62 | | | |
| $E$ | 276 | −90.58 | −90.57 | 225 | |
| $A_2$ | | | −90.43 | 226 | |
| $A_1$ | 277 | −90.36 | | | |
| $E$ | 278 | −90.29 | −90.22 | 227 | |
| $A_1$ | 279 | −90.19 | | | |
| $E$ | 280 | −90.17 | −90.17 | 228 | |
| $A_2$ | | | −90.11 | 229 | |
| $A_2$ | | | −90.09 | 230 | |
| $E$ | 281 | −90.03 | −90.01 | 231 | |
| $A_1$ | 282 | −89.81 | | | |
| $E$ | 283 | −89.77 | −89.76 | 232 | |
| $E$ | 284 | −89.67 | −89.66 | 233 | |
| $A_2$ | | | −89.65 | 234 | ? |
| $E$ | 285 | −89.48 | −89.48 | 235 | |
| $A_1$ | 286 | −89.27 | | | |
| $E$ | 287 | −89.25 | −89.23 | 236 | |
| $A_1$ | 288 | −89.14 | | | |
| $E$ | 289 | −89.07 | −89.07 | 237 | |
| $A_2$ | | | −89.05 | 238 | |
| $E$ | 290 | −88.99 | −89.01 | 239 | |
| $A_1$ | 291 | −88.95 | | | |
| $E$ | 292 | −88.69 | −88.67 | 240 | |
| $E$ | 293 | −88.63 | −88.64 | 241 | |
| $A_1$ | 294 | −88.43 | | | |

| $\Gamma$ | $n$ | $A_1/E$ $E_n/\text{cm}^{-1}$ | $A_2/E$ $E_n/\text{cm}^{-1}$ | $n$ |
|---|---|---|---|---|
| $E$ | 295 | −88.38 | −88.38 | 242 |
| $E$ | 296 | −88.18 | −88.21 | 243 |
| $A_2$ | | | −88.12 | 244 |
| $E$ | 297 | −87.96 | −87.95 | 245 |
| $E$ | 298 | −87.85 | −87.89 | 246 |
| $E$ | 299 | −87.83 | −87.85 | 247 |
| $E$ | 300 | −87.75 | −87.71 | 248 |
| $A_1$ | 301 | −87.67 | | |
| $E$ | 302 | −87.49 | −87.57 | 249 |
| $E$ | 303 | −87.41 | −87.40 | 250 |
| $E$ | 304 | −87.31 | −87.32 | 251 |
| $E$ | 305 | −87.25 | −87.25 | 252 |
| $E$ | 306 | −87.15 | −87.17 | 253 |
| $A_1$ | 307 | −87.11 | | |
| $E$ | 308 | −86.94 | −86.94 | 254 |
| $E$ | 309 | −86.93 | −86.89 | 255 |
| $E$ | 310 | −86.81 | −86.82 | 256 |
| $E$ | 311 | −86.62 | −86.58 | 257 |
| $E$ | 312 | −86.60 | −86.56 | 258 |
| $E$ | 313 | −86.50 | −86.48 | 259 |
| $A_1$ | 314 | −86.47 | | |
| $E$ | 315 | −86.35 | −86.34 | 260 |
| $E$ | 316 | −86.28 | −86.27 | 261 |
| $E$ | 317 | −86.26 | −86.21 | 262 |
| $E$ | 318 | −86.11 | −86.13 | 263 |
| $E$ | 319 | −86.07 | −86.09 | 264 |
| $E$ | 320 | −86.01 | −86.04 | 265 |
| $E$ | 321 | −85.95 | −85.88 | 266 |
| $E$ | 322 | −85.81 | −85.73 | 267 |
| $E$ | 323 | −85.74 | −85.69 | 268 |
| $E$ | 324 | −85.54 | −85.57 | 269 |

| Γ | n | $A_1/E$ $E_n/$cm$^{-1}$ | $A_2/E$ $E_n/$cm$^{-1}$ | n |
|---|---|---|---|---|
| $A_1$ | 325 | −85.45 | | |
| $A_1$ | 326 | −85.39 | | |
| $E$ | 327 | −85.34 | −85.30 | 270 |
| $E$ | 328 | −85.20 | −85.14 | 271 |
| $E$ | 329 | −85.10 | −85.08 | 272 |
| $A_1$ | 330 | −85.08 | | |
| $E$ | 331 | −84.97 | −84.98 | 273 |
| $E$ | 332 | −84.92 | −84.86 | 274 |
| $A_1$ | 333 | −84.79 | | |
| $E$ | 334 | −84.73 | −84.73 | 275 |
| $E$ | 335 | −84.61 | −84.62 | 276 |
| $E$ | 336 | −84.54 | −84.59 | 277 |

**Table 6.1:** All the $J = 0$ vibrational band origins of Ar₃ up to 85.5 cm$^{-1}$. The symmetry assignment is in terms of the irreducible representations of $D_{3h}$(M) nuclear permutation group.

The cumulative energy level distribution is shown in Fig. 6.1; the density of states is the gradient of this. The density of states shows a sharp increase near the barrier to linearity, where a significant amount of extra phase space becomes accessible. The density then increases fairly steadily from about 2 states/cm$^{-1}$ at the barrier maximum to about 8 states/cm$^{-1}$ at $E = -100$ cm$^{-1}$.

## 6.2 Interpretation of the wave functions.

The wave functions presented here have not been assigned a definitive symmetry label, only one that indicates their position in the symmetry block they come from. The plots shown represent cuts through the wave functions at a fixed value of $r$ or $\theta$. The quantity plotted is that shown in Eq. 6.1. This is an
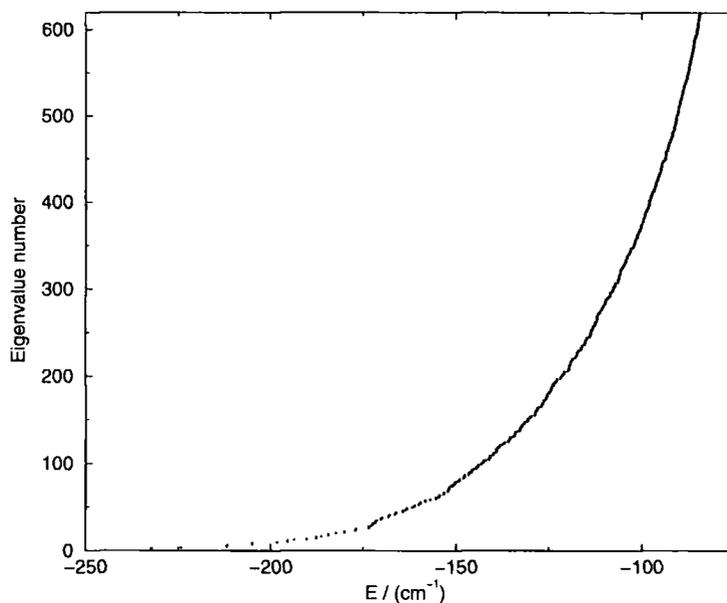
**Figure 6.1:** The eigenvalue distribution of $Ar_3$. The density of states is the gradient of the curve. The increase in the density of states above the barrier to linearity is clearly visible around $-170$ cm$^{-1}$.

FBR representation of the wave function. The FBR coefficients are obtained by transforming the DVR coefficients which in turn are the eigenvectors of the DVR Hamiltonian matrix.

$$\Psi_n^{pJ}(R, r, \theta) = R^{-1} r^{-1} \sum_{ijlK} c_{ijlKn}^{Jp} \, \phi_i^R(R) \phi_j^r(r) P_l^K(\cos \theta) \tag{6.1}$$

The wave functions from the even symmetry block are usually shown with either $\theta$ fixed at 90° or 0° or $r$ fixed at 3.757 Å. The states from the odd symmetry block have a node at 90° so a value of 80° is used instead. These representations of the wave functions appear to be the most helpful for present purposes although many others can also be envisaged.

Traditionally, quantum numbers would be assigned to vibrational wave functions using a normal mode approach. If the equilibrium geometry is known, group theory can be used to determine the normal modes of the molecule. It is then possible to determine the degree of excitation in each mode by examining each wave function in turn, starting with the ground state and working upwards. For $Ar_3$ this approach does work; it is described in section 6.3, but only for the very lowest lying levels. For the energy levels lying at higher energies the normal mode approximation rapidly breaks down.

The approximation that it is based upon, that of small amplitude uncoupled vibrations, is no longer valid for a molecule that is as floppy as $Ar_3$. Under these circumstances the wave functions are expected to show no discernible structure and to fill all the available space of possible nuclear configurations. However as section 6.4 illustrates this is far from being the case. Several of the states of $Ar_3$ show localisation features. The wave functions fill only a distinct subset of the space of possible nuclear configurations and show regular nodal patterns.

The localised states can be thought of as a series of regular states lying amongst a dense bath of states that show no regular features in their wave functions. The localised states will couple to the dense bath of states. The degree of coupling (relative to the spacing of the bath states) will determine the visibility of the localisation feature. The greater the coupling the more likely the localisation feature is to be smeared out over several bath states, making it invisible in the wave function plots.

To be able to identify these localisation features it is important to recognise how $Ar_3$ is described by a Jacobi coordinate system.

## 6.2.1 Equivalent geometries.
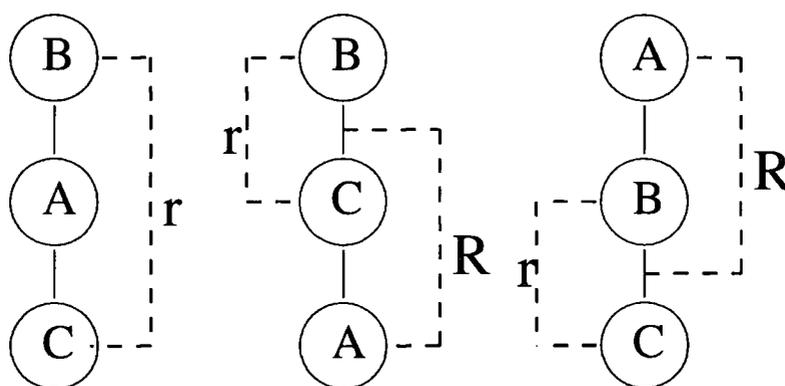


Figure 6.2: The three equivalent $Ar_3$ geometries. The atom labeled A can be either between the atoms of the diatomic fragment or at either end of it. If all the atoms are identical these geometries are all equivalent but have different descriptions in a Jacobi coordinate system.

A triatomic molecule can be described in terms of an atom A and a diatom
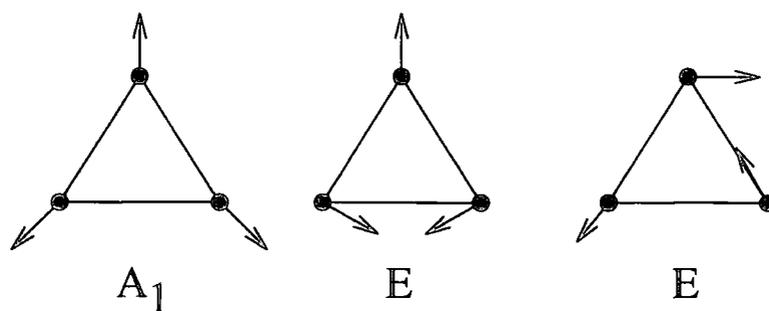
**Figure 6.3:** The normal modes of a $D_{3h}$ molecule. The figures show (L to R) the symmetric stretch $\nu_1$, the asymmetric stretch $\nu_{2a}$ and the asymmetric bend $\nu_{2b}$.

BC in three different ways. Each $Ar_3$ geometry can thus be described by three different sets of Jacobi coordinates. For example, the symmetric linear geometry with $r_{AB} = r_{BC} = r_m$ can be described by $(R, r, \theta) = (0, 2r_m, \text{undefined})$, $(1.5r_m, r_m, 0°)$ and $(1.5r_m, r_m, 180°)$. (See figure 6.2.) It is important to remember this when interpreting the wave functions. Features that occur at totally different values of $R$, $r$ and $\theta$ may correspond to exactly the same configurations of the molecule.

What this also means is that any localisation features observed in the wave functions should occur as a linear combination of localisation features at the three equivalent geometries. The pattern of three states showing localisation features is repeated throughout the remainder of this chapter.

## 6.3   The low lying levels of $Ar_3$

The equilibrium geometry of $Ar_3$ is an equilateral triangle. It has $D_{3h}$ symmetry. Its normal modes of vibration are shown pictorially in figure 6.3. The symmetric stretch has $A_1$ symmetry. The asymmetric bend and the asymmetric stretch form a degenerate $E$ pair. A symmetric stretch state will have a node in the $R = -\sqrt{3}r/2$ plane, $R$ and $r$ will increase in phase with each other. An antisymmetric stretch state will have a node in the $R = \sqrt{3}r/2$ plane, as $R$ and $r$ increase out of phase. An antisymmetric bend state will have a node in the $\theta$ plane.

The assignment of the energy levels of floppy molecules in terms of normal modes is often only possible for the low lying energy levels. Above the

| State | $\Gamma$ | $(\nu_1, \nu_2, l_2)$ | Energy/cm$^{-1}$ | Assignment | Figure 6.4: |
|-------|----------|------------------------|-------------------|------------|-------------|
| 1 | $A_1$ | (0,0,0) | $-254.895$ | Ground state | a |
| 2 | $E$ | (0,1,1) | $-232.378$ | Asymmetric stretch (A.S.) | b |
|   |   |   |   | Asymmetric bend (A.B.) | c |
| 3 | $A_1$ | (1,0,0) | $-224.284$ | Symmetric stretch (S.S) | d |
| 4 | $A_1$ | (0,2,0) | $-211.955$ |  | e,f |
| 5 | $E$ | (0,2,2) | $-211.834$ |  | g,h |
|   |   |   |   |   | i,j |

Table 6.2: Table showing the lowest energy levels of Ar$_3$ and their assignment.

barrier to isomerisation such an assignment would be invalid. To try to classify the vibrations of a molecule that can sample linear configurations in terms of the vibrations of one that has a triangular geometry is clearly an futile thing to do.

There are only six vibrational levels of Ar$_3$ that lie below the classical barrier to isomerisation. The effective barrier is raised somewhat by zero-point energy at the transition state, but nevertheless only the lowest five levels can be assigned in terms of normal modes. Figures 6.4 b-j show various cuts through the wave functions of these states. By considering the positions of the nodes in wave function the assignment in terms of normal mode quantum numbers is possible and is shown in table 6.2.

With two exceptions none of the other states of Ar$_3$ are assignable in terms of normal modes. Figures 6.4 k-l show wave functions for two of these energy levels. They are clearly unassignable in terms of normal modes. The relatively large amplitude motions of the atoms at these energies mean the normal-mode approximation breaks down.

## 6.4  Levels above the barrier to linearity

The classical isomerisation barrier occurs at $-199$ cm$^{-1}$. At the linear geometry, Ar$_3$ is expected to have about twice the zero-point energy of Ar$_2$ (15 cm$^{-1}$),
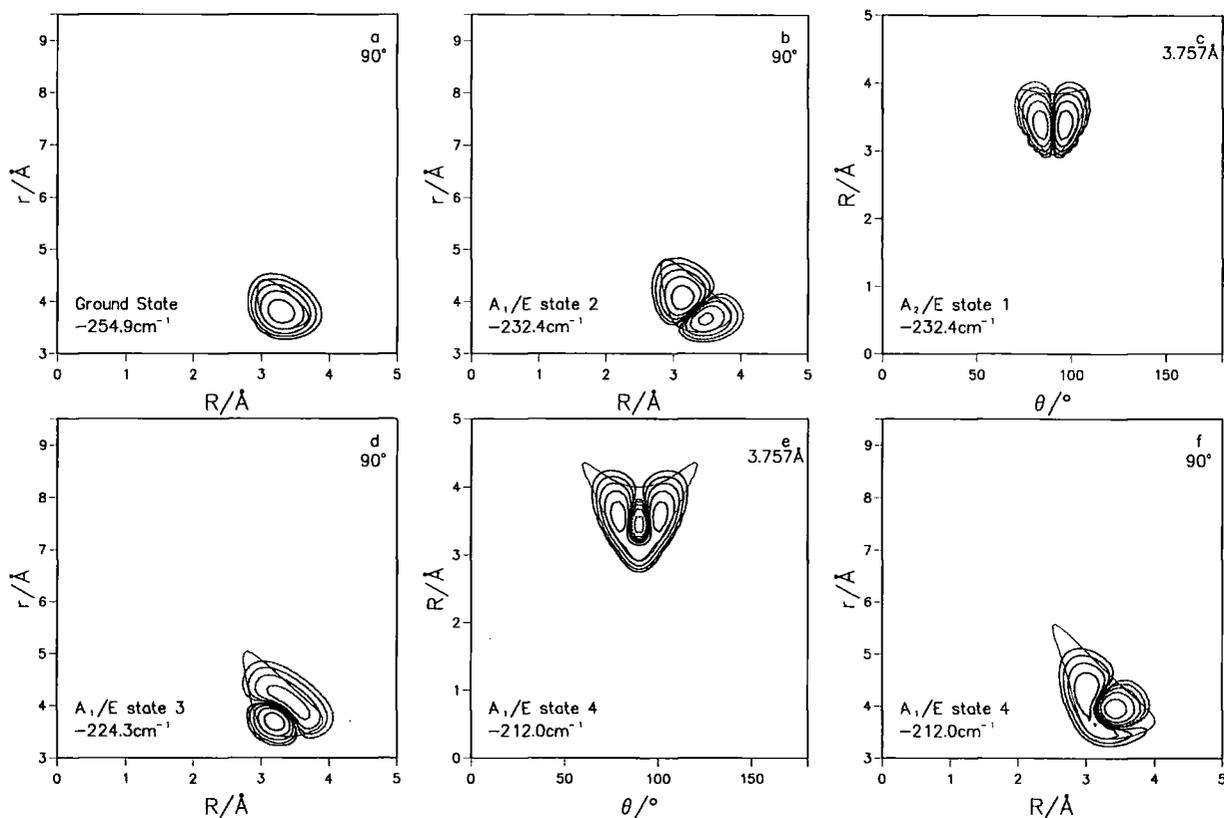
**Figure 6.4:** Two-dimensional cuts through the wave functions of the lowest states of $Ar_3$ plotted in Jacobi coordinates at $\theta = 90°$ or $r = 3.757$Å. The dotted line shows the boundary of the classically allowed region of configuration space at the energy concerned. Solid and dashed contours show positive and negative values of the wave function respectively. Contours are for 0.64, 0.32, 0.16, 0.08 and 0.04 of the maximum amplitude. The maximum amplitude is determined by comparing cuts at several values of $\theta$.
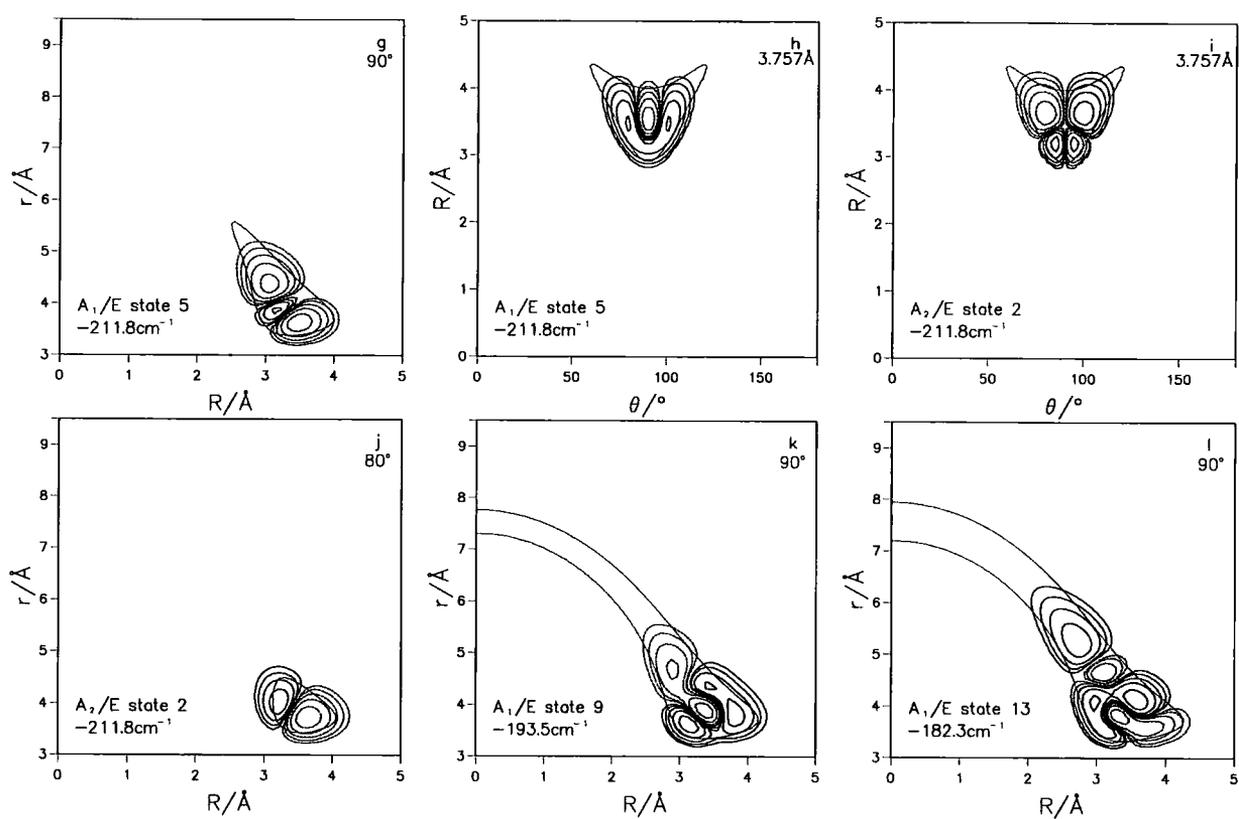
**Figure 6.4:** continued.
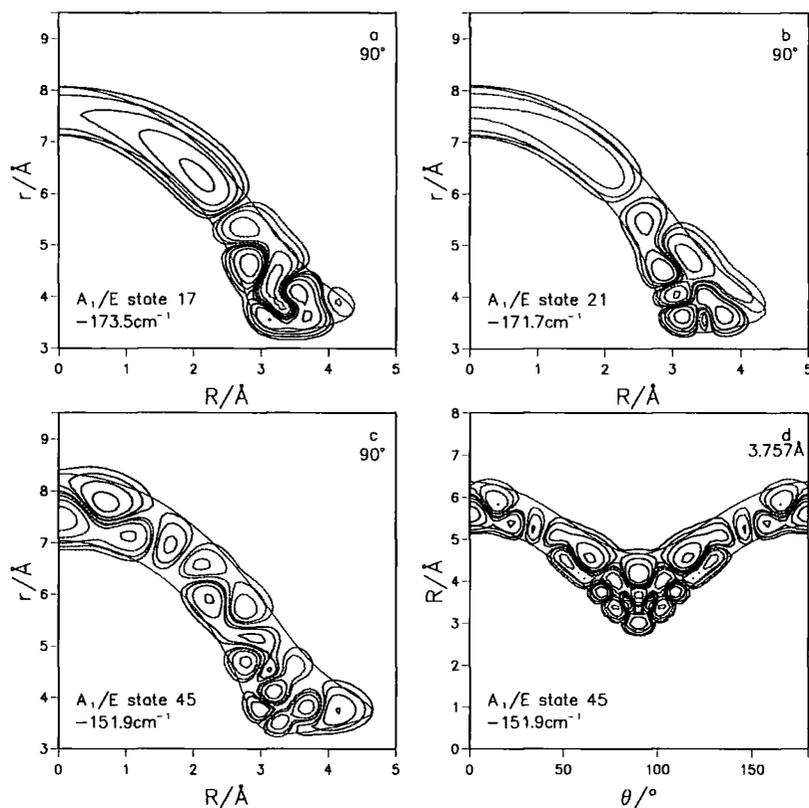
**Figure 6.5:** Wave functions of $Ar_3$ plotted as in figure 6.4. These states are the first to show amplitude above the barrier to linearity (a and b) and a typical bath state (c and d).

so the first level to sample the region around linearity significantly is expected near $-170$ cm$^{-1}$. The first state that has any amplitude around $R = 0$ is the 17th $A_1/E$ state at $-173.5$ cm$^{-1}$. The first state to show a maximum in wave function amplitude is the 21st $A_1/E$ state at $-171.7$ cm$^{-1}$. These states are shown in figures 6.5 a and b respectively.

Above the barrier to linearity the molecule does not show any structure in most of its wave functions. A typical example is $A_1/E$ state 45 shown in figures 6.5 c and d. Neither cut, at fixed $\theta$ or fixed $r$ shows any discernible structure. However this is far from true for every state.

## 6.4.1 Horseshoe states

In their studies on the $H_3^+$ molecular ion [26–28, 71], LiCN [72] and KCN [73] Tennyson and co-workers observed extensive localization effects in the wave functions of states lying above the barrier to linearity. In particular, they observed [26, 27, 71] a progression of "horseshoe" states in $H_3^+$. The wave functions of these states showed localisation features that suggested the molecule was predominately undergoing motion along the minimum energy pathway for isomerisation, shown in figure 4.1. One H atom moves between the other two (and out the other side), with the two "outer" atoms moving apart to make way for it. The horseshoe states are so-called because their wave functions show a regular nodal pattern that follows a horseshoe-shaped curve when plotted as a function of $R$ and $r$ such as in figure 6.6 a, including the reflection to negative $R$.

In $Ar_3$ there are also horseshoe states. One of the most prominent examples is shown in figure 6.6. The figure shows three consecutive states that are separated by less than 0.1 cm$^{-1}$. The horseshoe state is shown in figure 6.6 b. The localisation is very apparent upon comparison with the two other states in figures 6.6 a and c. The nodal structure is concentrated along a thin strip in the middle of the energetically allowed region of configuration space. The lower plots of figure 6.6 show the wave functions at a fixed value of $r$. The horseshoe state shows very little wave function amplitude in this plot, indicating that it is mostly localised in, or very close to, the $\theta = 90°$ plane. The localised nature of this state is very well illustrated by these plots.

Horseshoe states corresponding to localisation about the two equivalent geometries are visible as well. The horseshoe motion can also be visualised as an Ar atom rotating around the end of a $Ar_2$ diatom or, equivalently, as one of the atoms of the diatom pair moving through the middle of the other two. Figure 6.7 shows the two states that are the 'equivalent horseshoes' to that in figure 6.6. Figures 6.7 a and c show a state in the even symmetry block of the Hamiltonian. Figures 6.7 b and d show a state in the odd symmetry block. The states in figure 6.7 show some influence of the horseshoe trajectory outlined above but are basically horseshoe states of the 'equivalent' geometries.
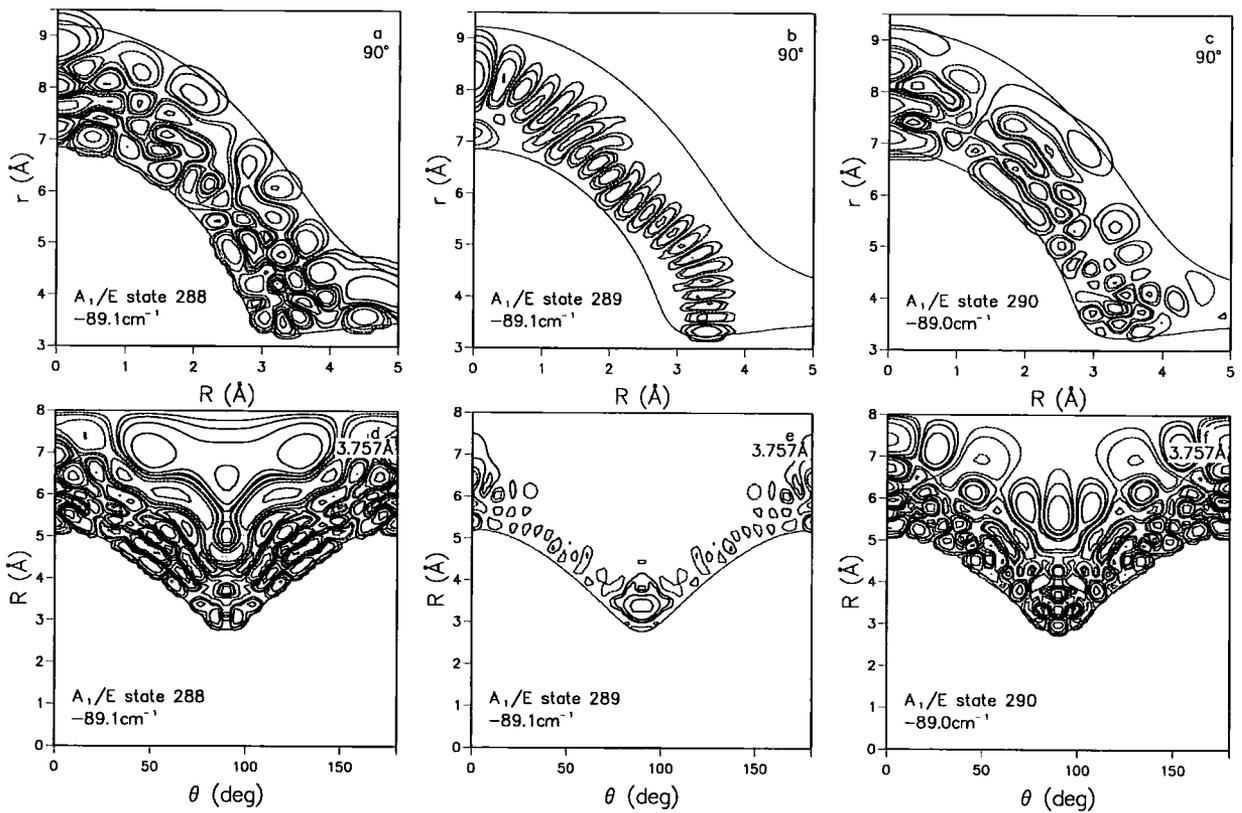
**Figure 6.6:** Cuts through the wave functions of a horseshoe state and two adjacent bath states.
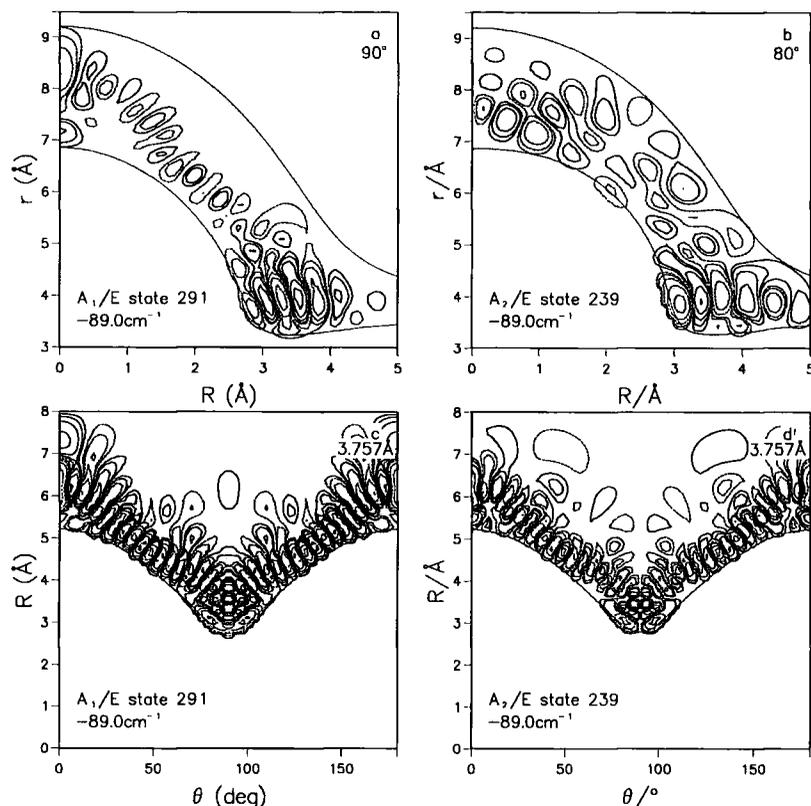
**Figure 6.7:** The other two states that form a triad with the state in figure 6.6b and e.

These three states form a triad that corresponds to the three linear combinations described in section 6.2.

The horseshoe states are expected to show an anharmonic progression amongst the states of $Ar_3$ and this is indeed the case. By inspecting the wave functions visually and counting the nodes it is possible to assign all the horseshoe states from dissociation downwards. The resulting progression is shown in Fig. 6.8. All of the horseshoe states are shown in Fig. 6.9 as cuts through the wave function at $\theta = 90°$ as this the easiest representation to counts the nodes in. From around 16 quanta upwards the horseshoe feature is very difficult to see in one state only and the state shown is the one with the most horseshoe character. The 'pure' state at around $-89$ cm$^{-1}$ in which the number of nodes can be easily counted confirms the assignments of the states where counting the nodes becomes a little more difficult.
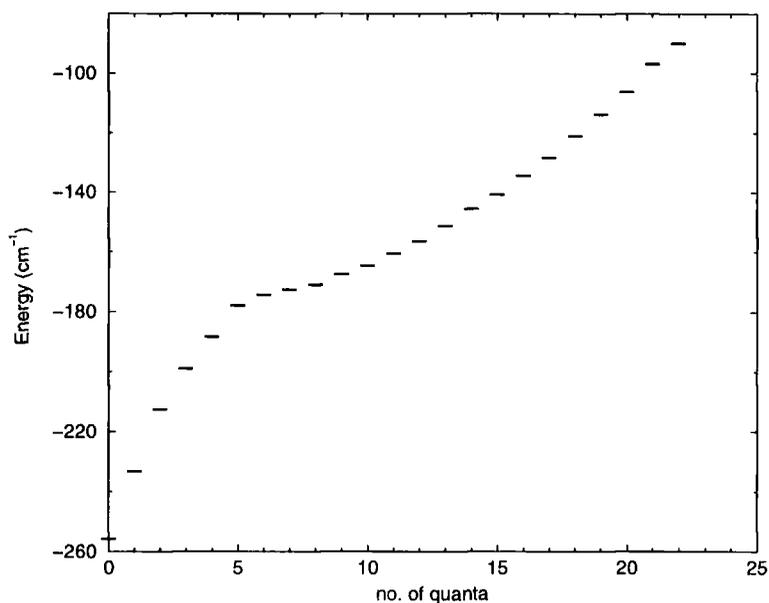
**Figure 6.8:** The progression of horseshoe states in $Ar_3$.

## 6.4.2 Symmetric Stretch

Several additional types of localization effect ("localized anharmonic modes") are visible in the wave functions of $Ar_3$. This section describes the linear symmetric stretch mode. This mode is most clearly seen as excitation in the $r$ coordinate with $R$ close to zero. Figure 6.10 shows states with quantum numbers $n_s = 1$ to 4 in this mode. In contrast to the horseshoe states the symmetric stretch states are much more easily identified. The localisation feature is much more apparent in the wave functions.

The separations between the symmetric stretch energy levels show a regular progression, as shown in table 6.3. The progression is far from being harmonic but the separations between the energy levels decrease in a manner typical of an anharmonic progression.

The equilibrium geometry of $Ar_2$ has $r_m = 3.757$ Å, so the three equivalent linear saddle point structures have $(R, r, \theta) \approx (0, 7.52$ Å, undefined), (5.64 Å, 3.76 Å, 0°) and (5.64 Å, 3.76 Å, 180°). The wave functions for the three states with $n_s = 3$ are shown in Figure. 6.11, and may be seen to show amplitude at all three geometries. Note that the symmetric stretch corresponds to $R$ and $r$ increasing *in phase* with one another in the feature at $r = r_m$. The properly symmetrised states are combinations of the states localised about the
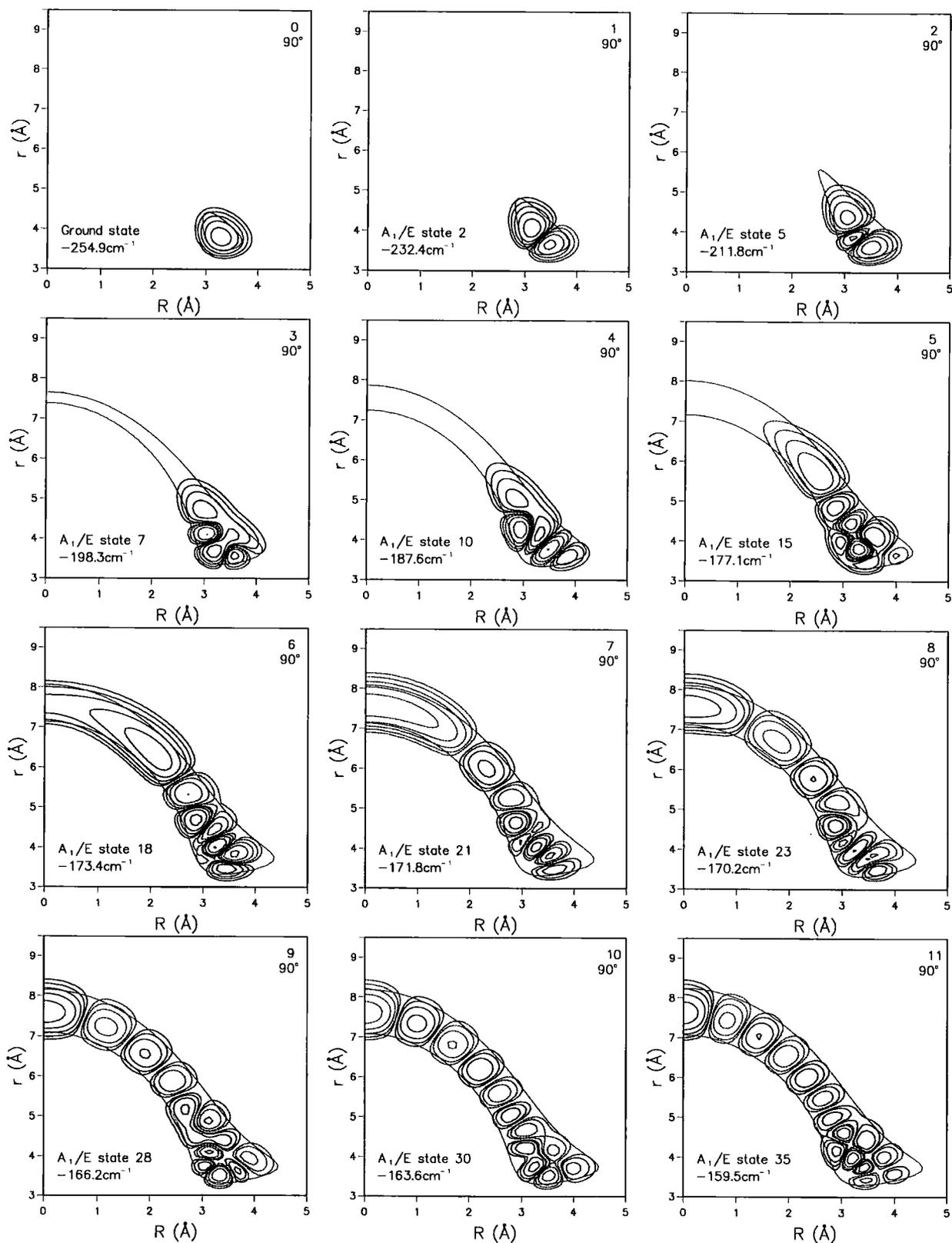
**Figure 6.9:** Progression of horseshoe states in Ar$_3$. The number in the top right corner is the number of quanta in the horseshoe mode.
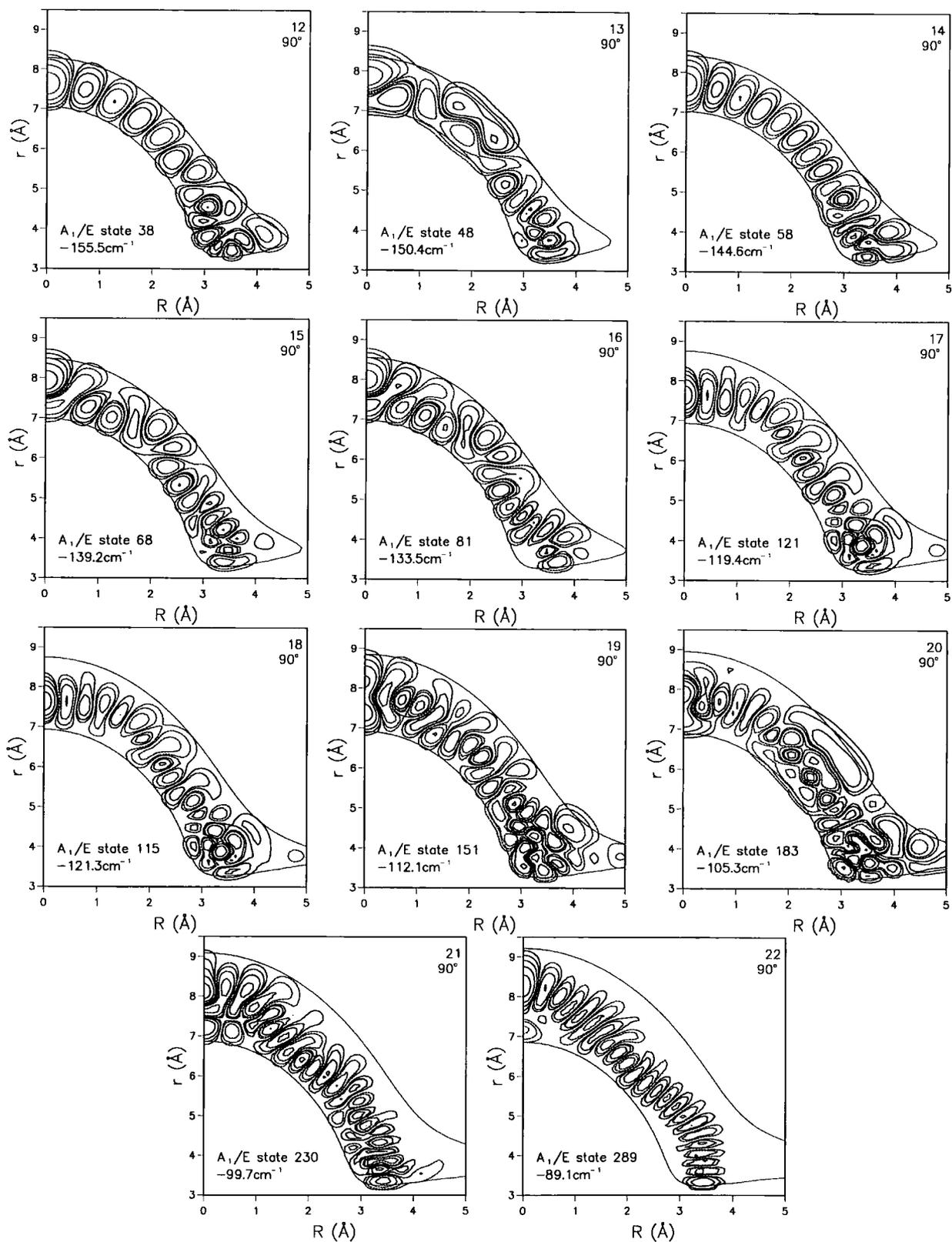
Figure 6.9: continued.
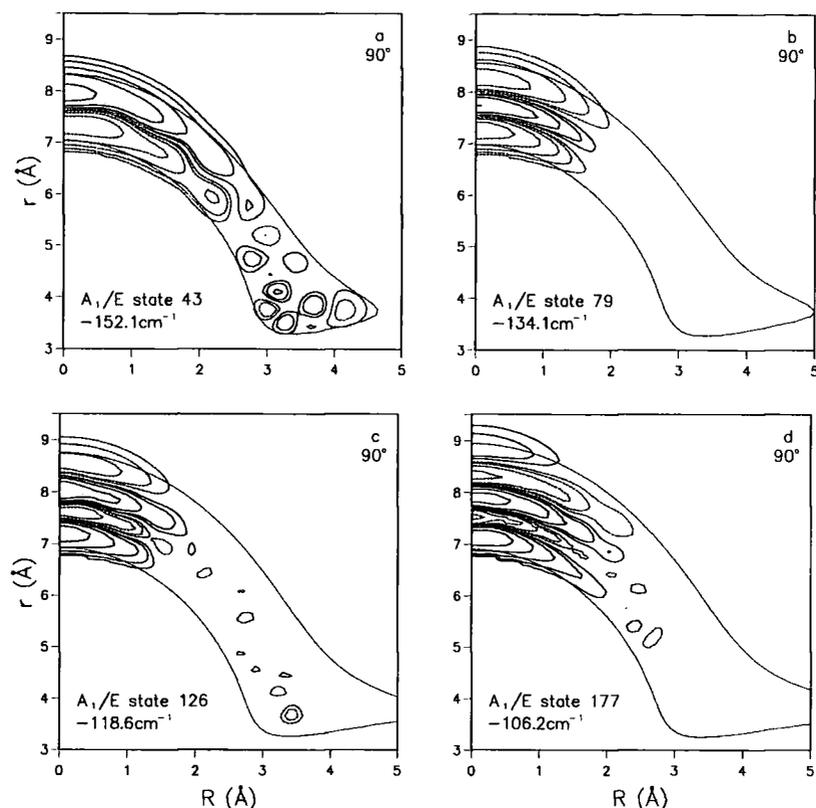
**Figure 6.10:** The wave functions of the states that have $n_s = 1 \rightarrow 4$ of excitation in the symmetric stretch mode.

three equivalent linear geometries, with $A_1$ and $E$ symmetry in the molecular symmetry group $D_{3h}(M)$. It may be seen that the basis set (which does not explicitly impose this symmetry) has produced reasonably well-symmetrised wave functions for these three states. As expected, two of the states ($A_1$, Figure. 6.11 a, and one component of $E$, Figure. 6.11b) are in the even symmetry block, and the third is in the odd block. Figure. 6.11d shows the $A_1$ state for $n_s = 3$ as a function of $R$ and $\theta$ for $r = r_m$; it may be seen that the function is indeed localised around the linear configuration(s), and does not undergo large angular excursions. This is true of all the symmetric stretch states.

There is also a progression of symmetric stretch states in the odd symmetry block of the Hamiltonian. These are shown in figure 6.12 and table 6.4. These states are at higher energies than the corresponding states with the same number of quanta in the symmetric block. By symmetry they also contain a node at $\theta = 90°$ i.e. they contain one quantum of asymmetric bend.

| Quantum number | Energy / $cm^{-1}$ | $E_n - E_{n-1}$ / $cm^{-1}$ |
|:---:|:---:|:---:|
| 1 | $-152.0$ | |
| 2 | $-134.1$ | 17.9 |
| 3 | $-118.6$ | 15.5 |
| 4 | $-106.2$ | 12.4 |

Table 6.3: Progression of the linear symmetric stretch mode for $Ar_3$.

They should therefore lie approximately 22 $cm^{-1}$ (the energy of one quantum of asymmetric bend) above the corresponding states in the even block and this is in fact the case.

| Quantum number | Energy / $cm^{-1}$ | $E_n - E_{n-1}$ / $cm^{-1}$ |
|:---:|:---:|:---:|
| 1 | $-125.6$ | |
| 2 | $-112.0$ | 13.6 |
| 3 | $-101.3$ | 10.7 |

Table 6.4: Progression of the linear symmetric stretch mode in the odd symmetry block for $Ar_3$.

### 6.4.3 Asymmetric stretch

The two localisation features previously described can be explained in terms of vibrations about a symmetric linear geometry, which corresponds to a saddle point on the potential energy surfaces of both $H_3^+$ and $Ar_3$. The horseshoe motion can be considered as a (very) wide-amplitude bending motion about such a geometry. The 'remaining' mode of a linear molecule, the antisymmetric stretch, was the next obvious one to look for.

The obvious place to look for it is at $\theta = 0$, as excitations in $R$ about $R = 0$ with $r \approx 2r_m$. Such features are indeed observed, as seen in Figure. 6.13a (which is for a state in the odd block, because a node is required at $R = 0$). This state also shows amplitude around the configuration corresponding to the "reordered" linear geometries. Since this is an antisymmetric stretch, $R$
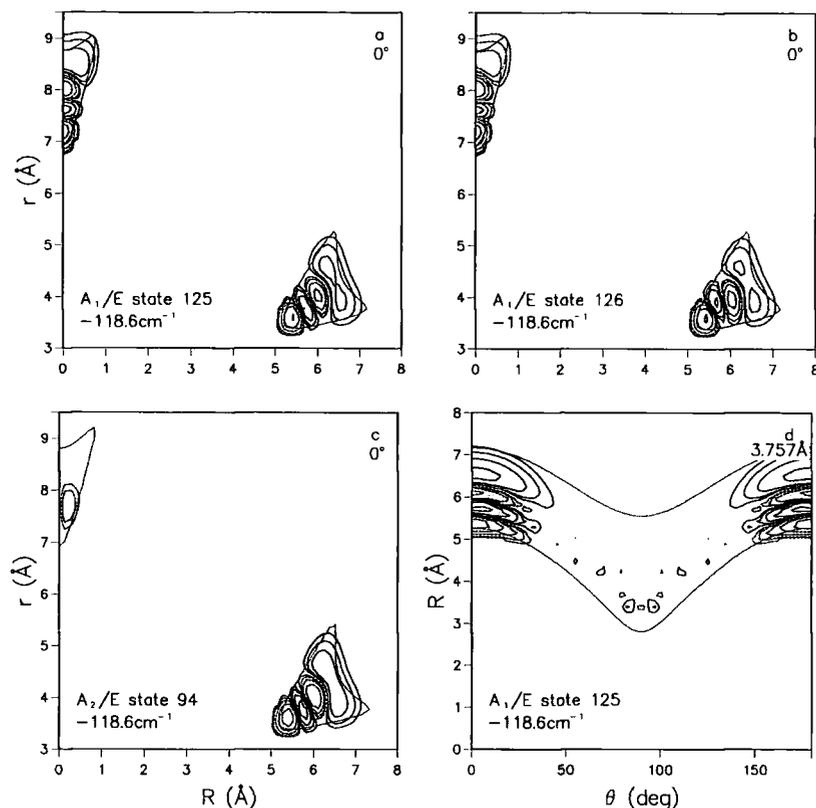
**Figure 6.11:** Several cuts through the wave functions of the triad of $n_s = 3$ states.

and $r$ increase *out of phase* with one another in the feature at $r = r_m$. However, in this case the amplitude is *not* confined to the linear geometries. Figure. 6.13b shows the wave function as a function of $R$ and $\theta$ for $r = r_m$ and Figure. 6.13c shows it as a function of $R$ and $r$ for $\theta = 80°$ (because there is a node at $\theta = 90°$): the molecule is clearly undergoing horseshoe-type motion in addition to the antisymmetric stretch. The stretching motion involved here is perhaps best considered as the intermolecular stretch of an atom–diatom complex. At $\theta = 0$, the radial motion in Figure. 6.13b is essentially the asymmetric stretch of a linear molecule, but near $\theta = 90°$ the amplitude of the "stretching" motion is enough to carry the atom through the center of the diatom, and this is the horseshoe motion.

No state showed a localisation feature that corresponds to excitation in the asymmetric stretch mode on its own. They all show some degree of excitation in the horseshoe mode as well. To understand why this should be
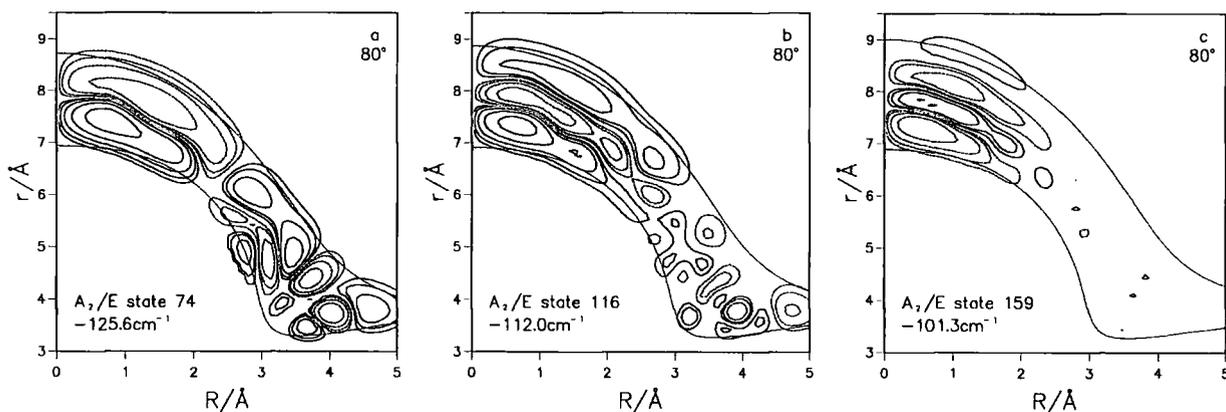
**Figure 6.12:** Several cuts through the wave functions of $A_2/E$ states showing the symmetric stretch mode.

the case it is helpful to consider the phase of the motions in $R$ and $r$ for the horseshoe, symmetric and asymmetric stretch modes.

The symmetric stretch states correspond to $R$ and $r$ increasing in phase with each other whereas both the horseshoe motion and the asymmetric stretch correspond to $R$ and $r$ increasing out of phase with each other. Therefore the symmetric stretch motion cannot couple to either of the other two modes which explains the relatively easy detection of it visually. On the other hand the asymmetric stretch motion and the horseshoe motion can couple quite easily. This explains the difficultly of finding a state that exists with only asymmetric stretch features. The coupling between these two motions will be quite large. It may also go some way to explaining the difficulty of observing the pure horseshoe states also.

The state described in this section is a combination of two of the modes of a linear molecule. It is not unreasonable to expect therefore that combinations involving the symmetric stretch will be observable. These are described in the next section.

## 6.4.4  Combined anharmonic modes

The simplest state to show a combination of the symmetric stretch and the horseshoe mode would contain one quantum of each. This state however is not visible. The simplest visible is a triad of states around $-130$ cm$^{-1}$ shown
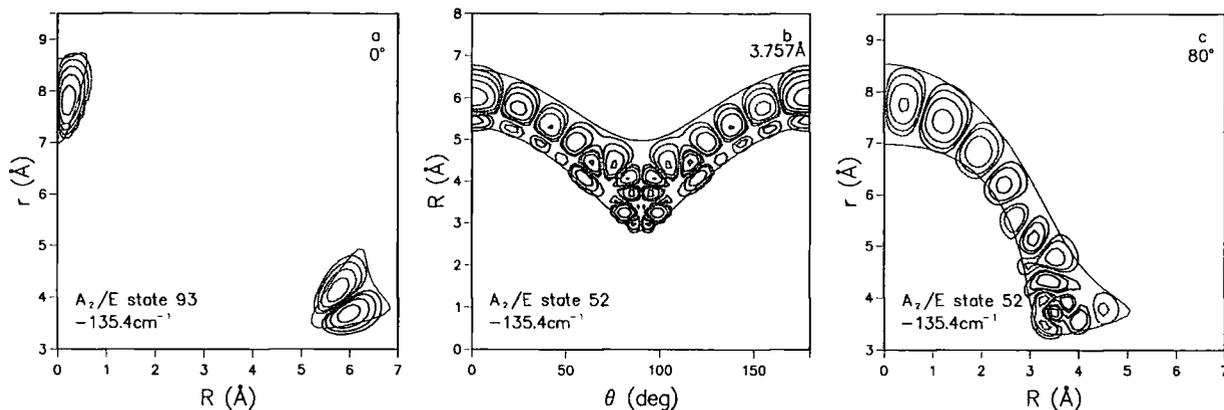
**Figure 6.13:** Several cuts through the wave function of $A_2/E$ state 93 showing the asymmetric stretch mode.

in figure 6.14. These contain two quanta of symmetric stretch and one of the horseshoe mode. Like the other symmetric stretch states these do not sample the full range of possible values of $\theta$. They do however sample a significantly greater amount than the states that only contain excitation in the symmetric stretch mode. This is due to the influence of the one quantum of excitation in the horseshoe mode. The state from the odd symmetry block shows no wave function amplitude around $R = 0$ as was also the case with the state from the odd symmetry block for the pure symmetric stretch.

Figure 6.15 shows another pair of localized states which are combinations of the symmetric stretch and horseshoe modes. These states contain a larger degree of excitement in the horseshoe than the previous example. These states are similar to the "nodal horseshoe" described for $H_3^+$ in Ref. [74]. The fact that the nodal horseshoe is a combination of two localized modes suggests that the linear symmetric stretch mode is probably present in $H_3^+$ as well.

## 6.5 Wave function localisation and periodic orbits

The energy levels above the barrier to linearity can be thought of as a dense bath of states. Superimposed upon this dense bath is a progression of regular states. These correspond to the overtones of several regular kinds of motion,
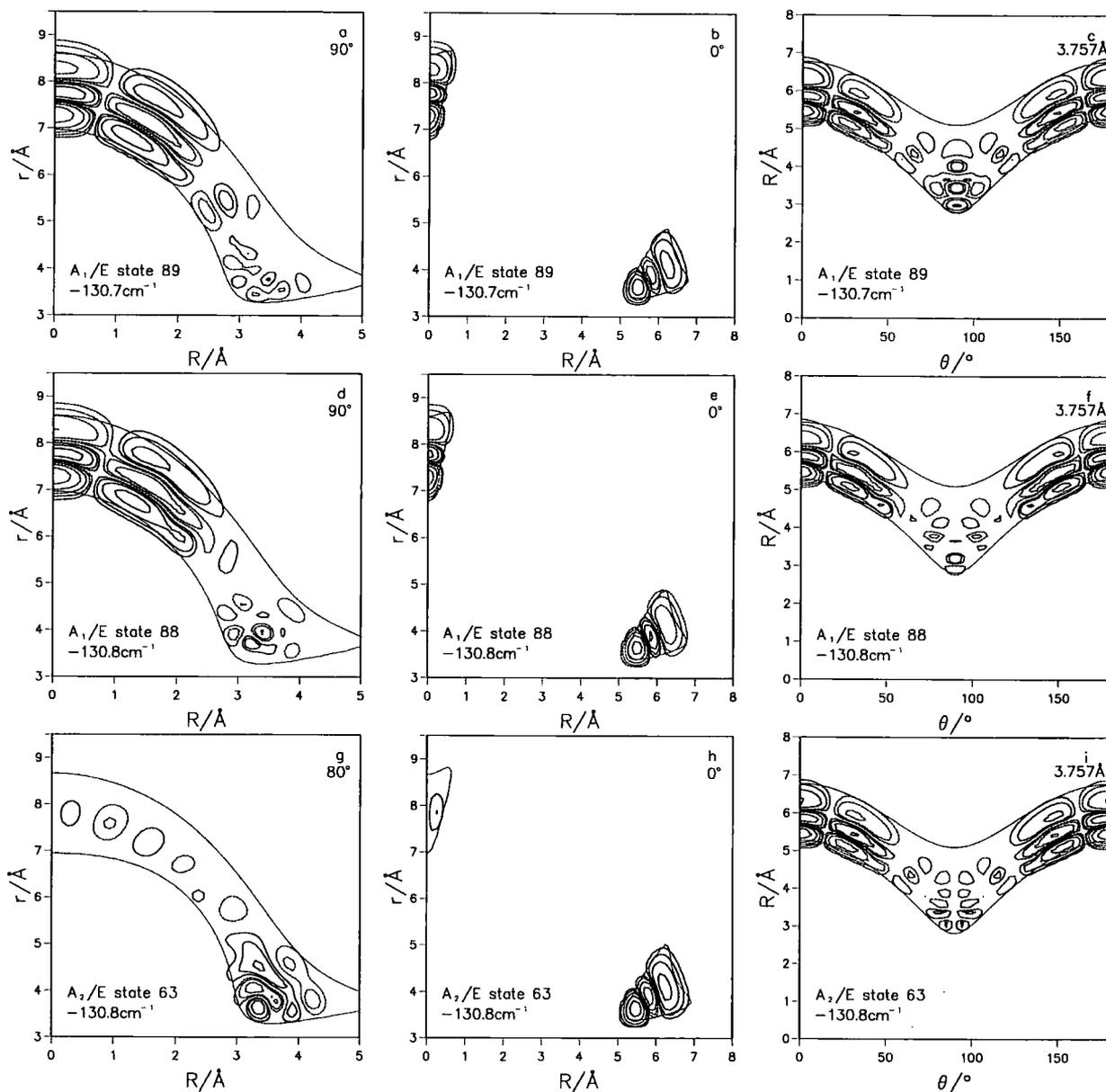
**Figure 6.14:** Several cuts through the wave functions of the triad of states involving excitation in the symmetric stretch mode and the horseshoe mode.
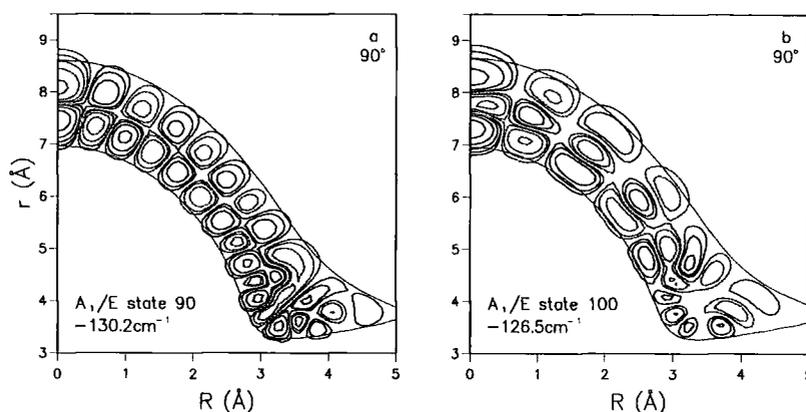
**Figure 6.15:** Wave functions for states involving simultaneous excitation in the linear symmetric stretch and horseshoe modes

such as the horseshoe. Each of these regular states couples to some of the bath states in its immediate vicinity. The greater the coupling to a particular bath state the more the bath state will show localisation in its wave function. The degree of coupling controls whether the localisation feature will be visible or not. If it is strongly coupled to several states the localisation will be smeared out over several bath states and will not be visible. If however the coupling is less strong the feature will only be 'smeared' over a small number of states and will be clearly visible in the wave functions of those states.

The picture of regular features spread over several states accords with the standard "time-independent" picture of intramolecular vibrational energy redistribution [75] (IVR): when a regular state is embedded in a dense "bath" of other states, the character of the regular state is spread out over the bath states, its contribution peaking as a function of energy in a near-Lorentzian manner. At higher energies, the density of "bath" states is greater and the "regular" character is spread over more energy levels. If the bath is dense enough, it may turn out that no one eigenstate ends up with a significant amount of "regular" character. Such effects can be thought of as the bound state analogue of quantum mechanical scattering resonances. When the quasi-continuum becomes an actual (dissociative) continuum, the regular character is spread out over the width of the resulting predissociating state.

In $H_3^+$, the regular states are localized along the trajectories of classical pe-

riodic orbits [76]. Such orbits are (classical) trajectories that describe closed figures in phase space, so that after some time $t$ the classical system has exactly the same position and momentum as before. (For more details, see Refs. [77–79].) A study of the periodic orbits of Ar$_3$ on the potential energy surface used here has been carried out [80], but it concentrated on Ar + Ar$_2$ collisions (at energies above those relevant to bound states). Calculating the bound-state periodic orbits of Ar$_3$ is beyond the scope of this present thesis, but it seems reasonable to attribute the localization effects observed here to such orbits. Investigating the connection between the localization effects and periodic orbits of Ar$_3$ would be an interesting topic for future work.

# CHAPTER

## 7

# Rotationally excited states of $Ar_3$

The aim of this chapter is to describe calculations of states of $Ar_3$ where $J = 1$. This should enable the extraction of the rotational constants by taking differences between energy levels. Whether the barrier to linearity is noticeable in the rotational energy level pattern will be an interesting question. This is not the most rigorous method of determining rotational constants because it does not allow centrifugal distortion constants to be determined, for example. However the time-consuming nature of calculations for $J > 1$ make it suitable for the current purposes.

Hopefully the methods outlined in this chapter can be used to analyse the effect of rotation upon the localisation effects described in the previous chapter. Another possible application is in the determination of the effect of non-additive intermolecular forces upon the rotational energy level structure.

# 7.1 Calculation of Rotationally excited states

The calculation of rotationally excited states is a difficult problem. If the Hamiltonian of Eq. 3.5 is solved directly, the size of the matrix to be diagonalised increases as $(2J + 1)$. Symmetrisation with respect to the parity operator reduces the problem to two separate matrices increasing as $J$ and $J + 1$, but does not solve the basic problem with large $J$ calculations. These difficulties place an upper limit on calculations of around $J = 4$.

One way to avoid the problem of rapidly increasing matrix size is to use the two-step procedure suggested by Tennyson and Sutcliffe [52]. This is described at the end of section 2.5.1. The first stage is to solve a series of 'vibrational' Hamiltonians which are obtained by ignoring the off-diagonal matrix elements which couple rotation and vibration. This involves treating $k$, the projection of the total angular momentum on the body-fixed $z$-axis as a good quantum number. The second stage involves the transformation of the off-diagonal coupling matrix elements to a truncated basis of the eigenvectors of the uncoupled representation and then diagonalising. The resulting matrix is very sparse and can be diagonalised very rapidly using an iterative method. Using this method calculations up to $J = 20$ have been performed [52].

For low $J$ values the two-stage procedure is the method of choice if a conventional diagonaliser, such as that employed for the $ArCO_2$ calculations in chapter 2, is used. In this case the two-stage procedure will scale as $(J + 1)n^3$ (or $(J)n^3$ for $f$ states) because the speed of the conventional diagonaliser scales as the third power of the size of the matrix. If however the whole Hamiltonian matrix were diagonalised without employing the two-stage procedure the calculation would scale as $((J + 1)n)^3$ (or $(Jn)^3$ for $f$ states) which clearly would soon become prohibitively expensive. This is not the case however when a Lanczos diagonaliser is used. The linear scaling of the Lanczos diagonaliser with respect to the size of the matrix means that it will be just as efficient to perform a two-stage calculation as one where the whole matrix is diagonalised in one step. Theoretically therefore the two approaches have equivalent requirements when using a Lanczos diagonaliser. Practically however there will be a limit on the maximum size of matrix it is possible

to treat using a Lanczos diagonaliser because of the memory requirements of the workspace and the storage of the eigenvectors. Therefore for high $J$ values the Tennyson and Sutcliffe approach is the only viable one.

The two-stage procedure assumes in its first stage that $k$ is a good quantum number. For $Ar_3$ this is not even nearly the case. The second stage of such a calculation likely therefore to need to retain a large number of eigenvectors from the first stage to converge the calculation. This source of inefficiency tips the balance in favour of diagonalising the whole Hamiltonian using the Lanczos method. Another factor in my choice is the easier implementation of the diagonalisation of the whole Hamiltonian which for a preliminary study such as this is quite an important aspect.

## 7.2  Quantum numbers, Rotational Constants and Energy Level Expressions.

Rotational energy levels of $Ar_3$ can be labeled by four quantum numbers: the total angular momentum $J$, its projection onto the body-fixed $z$-axis $K$, the vibrational angular momentum associated with the $\nu_2$ vibration $l_2$ and the parity $p$. Both $J$ and $p$ are good quantum numbers. The strong Coriolis interactions present in the molecule mean $K$ and $l_2$ are not good quantum numbers. A quantity called $G$, which is defined to be $|K - l_2|$, is a nearly good quantum number and is sometimes used to label the states of $D_{3h}$ molecules [10]. I will not use it here.

Symmetrisation with respect to the parity operator splits the Hamiltonian into two independent blocks. The parity is the symmetry of the system with respect to space-fixed inversion. Energy levels are usually labeled either $e$ or $f$ which correspond to even and odd combinations of $-K$ and $+K$. For states labeled $e$ with even values of $J$ the parity is even ($p = +1$) and for states with odd values of $J$ the parity is odd ($p = -1$). For $f$ states with even values of $J$ the parity is odd ($p = -1$) and for odd values of $J$ the parity is even ($p = +1$). The $e$ and $f$ labels reflect $(-1)^J p$. For $J = 0$ states no $f$ combination is possible because $K = 0$ and $K = -0$ are the same thing.

The symmetry adaptation used in the $J = 0$ calculations, that of symmetry with respect to exchange of the 'diatom' pair, is still present for states where $J > 0$ which means the Hamiltonian matrix splits into four independent blocks.

Ar$_3$ is an oblate symmetric top. It is shaped like a flying saucer. Two of the moments of inertia, $I_a$ and $I_b$, are equal and are smaller than the third, $I_c$. The largest moment of inertia $I_c$ corresponds to rotation about the $C_3$ axis of the molecule. $I_a$ and $I_b$ can be thought of as rotation about and perpendicular to a $C_2$ axis of the molecule.

An energy level formula for the rotational levels of $D_{3h}$ molecules near equilibrium has been given by Herzberg [81]

$$E(J, K, l_2) = \bar{B}J(J+1) + (C - \bar{B})K^2 - 2\zeta C K l_2 + E_{\text{high}}(J, K, l_2) \qquad (7.1)$$

where $E$ is the rotational energy of the state, $\bar{B} = (A + B)/2$ and $C$ are the rotational constants for the vibrational state and $\zeta$ is the Coriolis coupling constant. $E_{\text{high}}(J, K, l_2)$ can be further divided into three terms

$$E_{\text{high}}(J, K, l_2) = E_{\text{high}}^{\text{Cen}}(J, K, l_2) + E_{\text{high}}^{\text{Cor}}(J, K, l_2) + U E_{\text{high}}^{lres}(J, K, l_2) \qquad (7.2)$$

where $E_{\text{high}}^{\text{Cen}}(J, K, l_2)$ represents higher order centrifugal distortion corrections to the rotational energy. Both $E_{\text{high}}^{\text{Cor}}(J, K, l_2)$ and $U E_{\text{high}}^{lres}(J, K, l_2)$ are higher order Coriolis terms. The former, $E_{\text{high}}^{\text{Cor}}(J, K, l_2)$, is the energy that results from the coupling of states where the $K$ quantum number differs by $\pm 1$. The latter, $U E_{\text{high}}^{lres}(J, K, l_2)$, represents energy that results from the coupling between the $A_1$ and the $A_2$ states described below. The quantity $U$ is not a quantum number, it is simply a label to describe the upper ($U = +1$) and lower ($U = -1$) states split by this interaction. For all other states $U = 0$. The form of all the higher-order terms is quite complicated [10, 82] and with only $J = 1$ calculations there is not enough information available to allow the determination of the individual coefficients that make them up. In this work the $E_{\text{high}}^{\text{Cen}}(J, K, l_2)$ term is ignored completely as it is impossible to determine its magnitude from these calculations. It should be remembered however that the values for the rotational constants obtained will contain a contribution from this term. Eq. 7.2 is only valid near equilibrium and therefore the description of
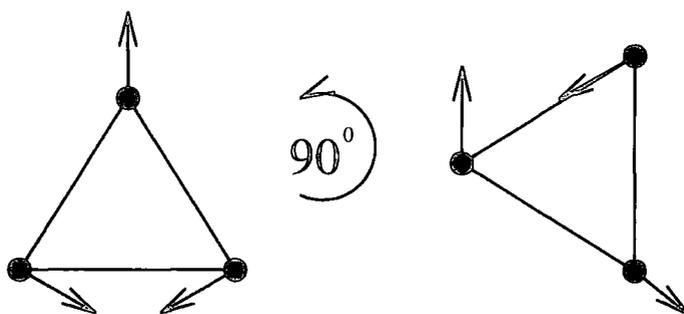
**Figure 7.1:** An illustration of the effect of a 90° rotation upon the $\nu_{2a}$ mode of Ar₃.

the energy level pattern it provides will almost certainly break down at the barrier to linearity if not before.

In rotating molecules the Coriolis force produces an interaction between two different vibrational modes which increases with increasing rotation. The interaction is small as long as the interacting modes have rather different frequencies. In Ar₃ however there is a pair of degenerate vibrations $\nu_{2a}$ and $\nu_{2b}$. In this case the Coriolis interaction is large and cannot be considered as a second-order effect as it is in linear molecules. To understand why there is a large Coriolis effect upon the degenerate modes consider Figure 7.1. This shows the effect of a 90° rotation upon the $\nu_{2a}$ mode of a $D_{3h}$ triatomic molecule. Under this rotation the atoms move but the displacement vectors retain the same orientation. After the rotation the molecule is vibrating in the $\nu_{2b}$ mode. In other words rotation about the $C_3$ axis of the molecule will convert the two vibrational modes from one to the other after every 90° of rotation. Therefore for a molecule that is rotating about this axis, i.e. $K > 0$, the $\nu_{2a}$ and $\nu_{2b}$ modes will become completely mixed. The actual energy levels of the molecule will be linear combinations of the $\nu_{2a}$ and $\nu_{2b}$ vibrational modes. The effect can also be thought of as an interaction between the vibrational angular momentum of the $\nu_2$ modes and the rotational angular momentum. The splitting of the energy levels due to this effect is described by the $2\zeta C K l_2$ term in Eq. 7.1. This first-order Coriolis coupling will affect the pattern of the energy levels. The symmetry of the rotational wave function is $E$ if $K$ or $l_2$ is not divisible by 3 and $A_1$ otherwise. Therefore the $E$ vibrational states, which are states where $\nu_2$ is excited, in the $J > 0$ calculation will form into

$E \times E = A_1 + A_2 + E$ if $K$ or $l_2$ is not divisible by 3 or $A_1 \times E = E$ if they are.

The higher-order term, $UE_{\text{high}}^{lres}(J, K, l_2)$ in Eq. 7.1, splits the $A_1$ and $A_2$ energy levels that occur when $K$ or $l_2$ is not divisible by 3 [82]. This is an $l$-type doubling term, a second order Coriolis effect. It will be possible to determine its magnitude from these calculations although, as previously mentioned, not the individual coefficients that make it up.

The Coriolis coupling will only affect the $C$ rotational constant. Therefore any deviation between the value obtained from energy level differences and from expectation values will be an indication of the magnitude of the term because the expectation values neglect Coriolis coupling. The $A$ and $B$ rotational constants will be unaffected by Coriolis coupling as they both correspond to rotation parallel to the plane formed by the three atoms. Any vibrational motion the atoms undergo will be in this plane and therefore will not be able to couple to the rotation about the $A$ and $B$ axes. In other words the rotational angular momentum vector will be perpendicular to the vibrational one making the coupling between them zero. To reflect the fact that the $C$ rotational constant obtained from energy levels differences is not the same as the one obtained from expectation values it will be denoted $C'$ because it contains a contribution from the $E_{\text{high}}^{Cor}(J, K, l_2)$ term.

## 7.3 Extracting Rotational Constants

The same input parameters as were used for the $J = 0$ calculation were retained for these calculations. In this section the study is restricted to the lowest 40 energy levels which are converged to the order of $0.003$ cm$^{-1}$. Such an exact calculation is not justifiable if one takes the view that any errors in the potential energy surface will be very much larger than the convergence errors. The reason for using such converged calculations is that the rotational constants themselves are very small compared to the magnitude of the energy levels. A rotational constant is typically of the order of $0.05$ cm$^{-1}$ in a system such as Ar₃ and is experimentally determinable to about 1 part in $10^5$. Therefore to be able to produce quantitative agreement with experiment the energy levels must be very accurately determined. As the rotational con-

stants of $Ar_3$ may defy experimental determination this discussion could be dismissed as purely academic. However it is the validity of the method for the determination of rotational constants that is being explored, with a view to future, experimentally more feasible, applications.

The energy level pattern produced for the lowest two vibrational states of $Ar_3$ is shown in figure 7.2. The determination of which $J = 1$ energy levels are associated with which $J = 0$ states is carried out by recognising these two distinct energy level patterns. The different energy level patterns for the states of different vibrational wave function symmetry means the extraction of the rotational constants must be performed differently for each.

| | | | -232.246 | -232.239 | | |
|---|---|---|---|---|---|---|
| E | -232.378 | -232.378 | -232.342 | -232.342 | -232.263 | -232.263 |
| A₁ | -254.895 | | -254.808 | -254.808 | | -254.778 |
| | | | | | | |
| j | e | o | e | o | e | o |
| | e | e | e | e | f | f |
| J | 0 | 0 | 1 | 1 | 1 | 1 |

Figure 7.2: Energy level diagram (not to scale) for the lowest two vibrational states of $Ar_3$. The labels along the bottom are the symmetry with respect to rotation of the 'diatomic fragment' $j$, the spectroscopic parity label $e/f$ and the total angular momentum $J$. The solid lines are states with $A_1$ vibrational wave functions and the dotted lines are those with $E$.

## 7.3.1 Rotational constants of $A_1$ states.

The extraction of rotational constants obviously involves the use of Eq. 7.1. For states of $A_1$ vibrational wave function symmetry $l_2 = U = 0$ and Eq. 7.1 becomes

$$E(J, K, 0) = \bar{B}J(J + 1) + (C' - \bar{B})K^2 \tag{7.3}$$

This expression represents the rotational energy of the state. As $Ar_3$ is an oblate symmetric top the quantum number $J$ will project onto the $C$ axis and the quantum numbers $K$ and $K_C$ will be the same.

To extract the rotational constants asymmetric top labels must be assigned to the energy levels. This can be done using the following arguments

1. Asymmetric top functions have parity $(-1)^{K_C}$, so that even parity states must have even $K_C$ and odd parity states must have odd $K_C$.

2. The highest levels of a given $J$ will have the lowest values of $K_C$ because $C$ is much smaller than $A$ and $B$.

Therefore the three energy levels in question can be labeled

$$E(J = 1^e, j = e) \;\; = \;\; 1_{01} = \bar{B} + C' \tag{7.4}$$

$$E(J = 1^e, j = o) \;\; = \;\; 1_{11} = \bar{B} + C' \tag{7.5}$$

$$E(J = 1^f, j = o) \;\; = \;\; 1_{10} = 2\bar{B} \tag{7.6}$$

where $E(J = 1^e, j = e)$ is the energy the $J = 1^e, j = e$ state is above the $J = 0^e, j = e$ state. Combining this with Eq. 7.3 gives the following expressions from which to obtain the rotational constants

$$2C' \;\; = \;\; +E(J = 1^e, j = e) + E(J = 1^e, j = o) - E(J = 1^f, j = o) \tag{7.7}$$

$$2\bar{B} \;\; = \;\; +E(J = 1^e, j = e) - E(J = 1^e, j = o) + E(J = 1^f, j = o) \tag{7.8}$$

$$2\bar{B} \;\; = \;\; -E(J = 1^e, j = e) + E(J = 1^e, j = o) + E(J = 1^f, j = o) \tag{7.9}$$

These equations allow the rotational constants for the $A_1$ states to be extracted quite straightforwardly. For the $A_2$ states the situation is similarly straightforward and the equations used are

$$2C' \;\; = \;\; +E(J = 1^e, j = e) + E(J = 1^e, j = o) - E(J = 1^f, j = e) \tag{7.10}$$

$$2\bar{B} \;\; = \;\; +E(J = 1^e, j = e) - E(J = 1^e, j = o) + E(J = 1^f, j = e) \tag{7.11}$$

$$2\bar{B} \;\; = \;\; -E(J = 1^e, j = e) + E(J = 1^e, j = o) + E(J = 1^f, j = e) \tag{7.12}$$

The difference between the two values of $\bar{B}$ gives a measure of the error involved in the calculation. The error will be due to any calculated difference between the theoretically degenerate $E(J = 1^e, j = e)$ and $E(J = 1^e, j = o)$ levels. In practice this gave differences of no more than 0.3 MHz. In such cases the average of the different calculated values is reported.

## 7.3.2 Rotational constants of $E$ states.

For states of $E$ vibrational wave function symmetry the situation is much more complicated as outlined in section 7.2. It is only possible to attach a symmetric top label to one state which occurs as a degenerate $E$ pair

$$E(J = 1^f, j = e) = 1_{10} \tag{7.13}$$

$$E(J = 1^f, j = o) = 1_{10} \tag{7.14}$$

as this is not subject to the strong Coriolis interactions because $K = 0$. It is not possible to attach symmetric top labels to the other energy levels as was done for the states of $A_1$ symmetry because $K$ is no longer a good quantum number for them. There are four states in question: two in the $J = 1^e, j = e$ stack and two in the $J = 1^e, j = o$ stack. The lower energy levels in each stack are degenerate, they form an $E$ pair. The upper two levels are of $A_1$ and $A_2$ overall symmetry and are split by the second order Coriolis term $E_{\text{high}}^{lres}(J, K, l_2)$ of Eq. 7.1. This energy level pattern is what was predicted theoretically as $K$ and $l_2$ are not divisible by 3. Therefore there are four energy levels described by the following equations

$$E(J = 1^e, j = e, \Gamma = A_1) = 2\bar{B} + (C' - \bar{B}) + 2\zeta C - E_{\text{high}}^{lres}(1, 1, 1) \tag{7.15}$$

$$E(J = 1^e, j = o, \Gamma = A_2) = 2\bar{B} + (C' - \bar{B}) + 2\zeta C + E_{\text{high}}^{lres}(1, 1, 1) \tag{7.16}$$

$$E(J = 1^e, j = e, \Gamma = E) = 2\bar{B} + (C' - \bar{B}) - 2\zeta C \tag{7.17}$$

$$E(J = 1^e, j = o, \Gamma = E) = 2\bar{B} + (C' - \bar{B}) - 2\zeta C \tag{7.18}$$

where the $\Gamma$ label refers to the overall symmetry of the state. By averaging Eq. 7.15 and Eq. 7.16 it is possible to cancel the $E_{\text{high}}^{lres}(1, 1, 1)$ term

$$[E(J = 1^e, j = e, \Gamma = A_1) + E(J = 1^e, j = o, \Gamma = A_2)]/2 =$$
$$2\bar{B} + (C' - \bar{B}) + 2\zeta C \tag{7.19}$$

This energy will be denoted $E_{\text{average}}$. By taking the mean of $E_{\text{average}}$ with Eq. 7.17 and Eq. 7.18 expressions for $\bar{B}$ and $C'$ are obtained in the same fashion as above,

$$2C' = [E_{\text{average}} + E(J = 1^e, j = e, \Gamma = E)]/2$$
$$+[E_{\text{average}} + E(J = 1^e, j = o, \Gamma = E)]/2 - E(J = 1^f, j = e) \tag{7.20}$$

$$2\bar{B} = [E_{\text{average}} + E(J = 1^e, j = e, \Gamma = E)]/2$$

$$-[E_{\text{average}} + E(J = 1^e, j = o, \Gamma = E)]/2 + E(J = 1^f, j = e) \quad (7.21)$$

$$2\bar{B} = -[E_{\text{average}} + E(J = 1^e, j = e, \Gamma = E)]/2$$

$$+[E_{\text{average}} + E(J = 1^e, j = o, \Gamma = E)]/2 + E(J = 1^f, j = e) \quad (7.22)$$

It is also possible to extract $\zeta C$ and $E^{lres}_{\text{high}}(J, K, l_2)$ as well and these numbers are quoted in the results section.

## 7.3.3   Rotational constants from expectation values

The rotational constants of Ar₃ can also be estimated by calculating the expectation values of the following quantities over the $J = 0$ wave functions. They are determined using numerical quadrature over the FBR wavefunctions obtained in the previous chapter.

$$A = \frac{\hbar^2}{2} \left\langle \frac{1}{\mu_2 r^2 \sin^2 \theta} + \frac{1}{\mu_1 R^2 \tan^2 \theta} \right\rangle$$

$$B = \frac{\hbar^2}{2} \left\langle \frac{1}{\mu_2 R^2} \right\rangle$$

$$C = \frac{\hbar^2}{2} \left\langle \frac{1}{\mu_2 R^2 + \mu_2 r^2} \right\rangle \quad (7.23)$$

These equations are not strictly correct as they do not take proper account of the Eckart condition [83]. This is expected to cause errors in the values of $A$ and $B$ calculated in this manner. It will not however cause errors in the value of $\bar{B}$. The amount that the value of $A$ is overestimated by not taking account of the Eckart condition will be the same as the amount $B$ is underestimated. The Eckart corrected value of $C$ was found to be less accurate than the uncorrected one [83] and therefore the uncorrected expression is used here. The value of $C$ calculated in this way takes no account of Coriolis coupling and therefore will be subject to an additional source of error.

Equation 7.23 corresponds to the body-fixed $z$-axis being embedded along the intermolecular axis $R$. At the linear configuration, $R = 0$, the expression for $B$ is infinite but the volume element is zero ($R^2 r^2 \sin \theta d\theta$), which will cancel out the singularity. However as $R \to 0$ the value of $B$ will get unphysically large making the value of $\bar{B}$ unphysically large also. Therefore this method of

| | This work | | Ernesti and Hutson [7] |
|---|---|---|---|
| | Energy level differences | Expectation Values | |
| $A$/MHz | | 1749.73 | 1741.01 |
| $B$/MHz | | 1732.93 | 1741.69 |
| $\bar{B}$/MHz | 1741.34 | 1741.33 | 1741.35 |
| $C$/MHz | | 862.23 | 862.23 |
| $C'$/MHz | 864.25 | | |

**Table 7.1:** A comparison of the ground state rotational constants calculated in this work and those calculated by Ernesti and Hutson [7].

calculating rotational constants, with the $z$-axis embedded along $R$, is valid only for states below the barrier to linearity.

The equilibrium geometry of Ar₃ is $\theta = 90°$, $r = 3.757$ Å and $R = 3.254$ Å. Putting these numbers into Eqs. 7.23, i.e. treating Ar₃ as a rigid body, the rotational constants are $A = B = 1791.58$ MHz and $C = 895.79$ MHz (1 cm$^{-1} \equiv 29979.2458$ MHz). In this case $2C = B = A$. The difference between these values and ones obtained for the vibrational ground state gives an idea of the degree of floppiness of the molecule.

## 7.4   Comparison with previous result

The rotational constants for the ground vibrational state were previously calculated by Ernesti and Hutson [7]. They used a different method of solving the Schrödinger equation which only allowed them to treat the $J = 0$ problem. The rotational constants were then obtained by calculating expectation values [83] over the $J = 0$ wave functions. Energy level differences have also been evaluated here. Table 7.1 shows a comparison between the results. The agreement between all three methods is very good. The value of $\bar{B}$ is obtained very accurately by all three methods. The values of $A$ and $B$ obtained from the two different methods of taking expectation values clearly show the error involved in neglecting the Eckart condition. The difference between

$C$ and $C'$ shows that for the ground vibrational state the Coriolis coupling term is approximately 2 MHz. Comparison with the rigid-body values of $A = B = 1791.58$ MHz and $C = 895.79$ MHz shows that Ar$_3$ is quite floppy in its vibrational ground state.

## 7.5   Rotational Constants for the energy levels below the barrier to linearity.

The rotational constants for the 17 lowest energy levels, all of which are below the barrier to linearity, are shown in table 7.2.

The agreement between the values of $\bar{B}$ obtained via the two different methods is very good. The good agreement shows that the centrifugal distortion is very small for these levels. It also suggests that although the individual values of $A$ and $B$ obtained from Eqs. 7.23 are in error this method does provide a simple way of obtaining the mean of $A$ and $B$.

The deviation between the values of $C$ and $C'$ can be attributed to Coriolis coupling. The deviations are much larger for some the states of $A_1$ or $A_2$ vibrational wave function symmetry because all of the Coriolis coupling occurs in the $E_{\text{high}}^{\text{Cor}}(J, K, l_2)$ term which is part of $C'$. For the states of $E$ vibrational wave function symmetry there are other Coriolis terms that contribute and the deviation between $C$ and $C'$ is much less.

The values of $\zeta C$ and $E_{\text{high}}^{l\text{res}}(J, K, l_2)$ show no clear trends. Negative values of $\zeta C$ indicate that the $E$ levels are above the $A_1/A_2$ pair. For two of the states in table 7.2 the magnitude of $E_{\text{high}}^{l\text{res}}(J, K, l_2)$ is much larger than $\zeta C$. As Eq. 7.2 is only really valid for states near the equilibrium geometry I suspect that this is an indication of it failing. The interactions between the neighbouring vibrational levels will invalidate the approach. To determine the values of $\zeta C$ and $E_{\text{high}}^{l\text{res}}(J, K, l_2)$ a matrix should be diagonalised to take account of the influence of the different vibrational states upon one another. Figure 7.3 shows the energy levels for the region below linearity. The density of states for all but the lowest 3 or 4 vibrational states is clearly too great to expect a one-state model to describe the coupling present.

| | | | | | | |
|---|---|---|---|---|---|---|
| | | | -176.892 | -176.873 | | |
| E | -176.982 | -176.982 | -176.926 | -176.892 | -176.859 | -176.859 |
| $A_1$ | -177.138 | | -177.058 | -177.058 | | -177.013 |
| | | | -179.894 | -179.879 | | |
| E | -179.984 | -179.984 | -179.919 | -179.919 | -179.872 | -179.872 |
| $A_1$ | -182.276 | | -182.194 | -182.194 | | -182.163 |
| | | | -184.183 | -184.183 | | |
| E | -184.306 | -184.306 | -184.276 | -184.255 | -184.193 | -184.193 |
| $A_1$ | -186.312 | | -186.228 | -186.228 | | -186.199 |
| | | | -187.521 | -187.508 | | |
| E | -187.609 | -187.610 | -187.542 | -187.542 | -187.499 | -187.498 |
| $A_2$ | | -190.216 | -190.135 | -190.135 | -190.105 | |
| $A_1$ | -193.528 | | -193.448 | -193.448 | | -193.418 |
| | | | -195.316 | -195.294 | | |
| E | -195.399 | -195.399 | -195.329 | -195.329 | -195.287 | -195.287 |
| $A_1$ | -198.254 | | -198.172 | -198.172 | | -198.142 |
| | | | -204.949 | -204.947 | | |
| E | -205.042 | -205.042 | -204.970 | -204.970 | -204.931 | -204.931 |
| | | | -211.688 | -211.688 | | |
| E | -211.834 | -211.834 | -211.819 | -211.811 | -211.722 | -211.721 |
| $A_1$ | -211.955 | | -211.872 | -211.872 | | -211.842 |
| $A_1$ | -224.294 | | -224.209 | -224.209 | | -224.181 |
| | | | -232.246 | -232.239 | | |
| E | -232.378 | -232.378 | -232.342 | -232.342 | -232.263 | -232.263 |
| $A_1$ | -254.895 | | -254.808 | -254.808 | | -254.778 |
| j | e | o | e | o | e | o |
| | e | e | e | e | f | f |
| J | 0 | 0 | 1 | 1 | 1 | 1 |

**Figure 7.3:** Energy level diagram (not to scale) for the lowest 17 vibrational states of $Ar_3$. The labels along the bottom are the symmetry with respect to rotation of the 'diatomic fragment' $j$, the spectroscopic parity label $e/f$ and the total angular momentum $J$. The solid lines are states with $A_1$ vibrational wave functions and the dotted lines are those with $E$.

| | E/cm$^{-1}$ | Rotational constants/MHz | | | | $\zeta C$ | $E^{lres}_{high}(J,K,l_2)$ |
|---|---|---|---|---|---|---|---|
| | | $\frac{1}{2}(\langle A \rangle + \langle B \rangle)$ | $\bar{B}$ | $\langle C \rangle$ | $C'$ | | |
| $A_1$ | $-254.89$ | 1741.3 | 1741.3 | 862.2 | 864.2 | | |
| $E$ | $-232.38$ | 1715.5 | 1715.5 | 838.6 | 841.3 | 751.4 | $-101.6$ |
| $A_1$ | $-224.29$ | 1694.4 | 1694.5 | 832.3 | 835.4 | | |
| $A_1$ | $-211.96$ | 1691.3 | 1691.5 | 813.5 | 807.8 | | |
| $E$ | $-211.83$ | 1690.1 | 1690.2 | 810.6 | 801.3 | $-953.4$ | $-121.9$ |
| $E$ | $-205.04$ | 1672.1 | 1672.2 | 807.3 | 825.0 | 169.4 | $-28.4$ |
| $A_1$ | $-198.25$ | 1668.8 | 1668.9 | 784.8 | 784.3 | | |
| $E$ | $-195.40$ | 1676.9 | 1677.1 | 774.6 | 766.0 | 181.6 | $-320.3$ |
| $A_1$ | $-193.53$ | 1655.9 | 1656.2 | 790.0 | 753.8 | | |
| $A_2$ | $-190.22$ | 1658.4 | 1658.2 | 789.7 | 768.5 | | |
| $E$ | $-187.61$ | 1664.5 | 1664.7 | 772.7 | 757.6 | 207.2 | $-195.9$ |
| $A_1$ | $-186.31$ | 1683.0 | 1683.1 | 752.8 | 816.7 | | |
| $E$ | $-184.31$ | 1686.4 | 1686.5 | 741.1 | 747.8 | $-619.7$ | $-310.2$ |
| $A_1$ | $-182.28$ | 1684.8 | 1685.0 | 750.1 | 763.2 | | |
| $E$ | $-179.98$ | 1670.1 | 1670.1 | 747.8 | 752.2 | 242.5 | $-218.4$ |
| $A_1$ | $-177.14$ | 1868.8 | 1868.3 | 667.8 | 522.4 | | |
| $E$ | $-176.98$ | 1845.1 | 1844.0 | 678.5 | 737.9 | $-53.3$ | $-789.9$ |

**Table 7.2:** Calculated rotational constants and Coriolis terms for the 17 lowest energy levels of $Ar_3$.

The value of $\bar{B}$ shows an overall decrease until the 9th level at $-193.13$ cm$^{-1}$ which is an indication of the larger average size of $Ar_3$ as it gets more vibrationally excited. At this point $\bar{B}$ starts getting slowly bigger. This is a reflection of the increasing amount of wave function density at smaller values of $R$ which will increase $\bar{B}$. The value of $\bar{B}$ shows a quite dramatic increase for last two states in table 7.2 which indicates that they are sampling much smaller values of $R$. The values of $C$ show a overall gradual decrease as the $Ar_3$ gets more vibrationally excited. This is because $C$ is a measure of the overall size of the molecule. The value of $C$ depends inversely on the sum of $R^2$ and $r^2$. As $R$ decreases $r$ will increase leaving the value of $C$ unchanged

overall. The information contained in $\bar{B}$ and $C$ indicates that as the molecule gets more vibrationally excited it samples a larger range in $R$ and $r$ which is exactly what the wave functions in chapter 6 show.

## 7.6 Rotational Constants for the energy levels above the barrier to linearity.

Above the barrier to linearity, as expected, the approximation inherent in Eq. 7.2 breaks down. The pattern recognition being used to tell which $J = 1$ levels correspond to which $J = 0$ ones fails and makes the extraction of rotational constants very difficult and eventually impossible. To predict the values of the rotational constants, and hence the $J = 1$ energy levels, from the expectation values is not possible either as the expressions used fail above the barrier to linearity.

The rotational constants for the 6 levels immediately above the barrier are shown in table 7.3. For the first level in the table the value of $E_{\text{high}}^{\text{Cor}}(J, K, l_2)$ is larger than the value of $C$ itself and the resulting value of $C'$ is negative. The next three levels show behaviour similar to the ones below the barrier and have feasible rotational constants. After this point the mixing between the $J = 1$ levels becomes large. The energy levels themselves are shown in table 7.4. The patterns overlap and it is no longer possible to assign each $J = 1$ state as being associated with a particular $J = 0$ state. For the $E$ level at $-170.176$ cm$^{-1}$ the $J = 1$ levels are below the $J = 0$ one. Clearly any method based on pattern recognition fails at this point as the simple patterns illustrated in figure 7.2 are no longer visible in the energy level structure. The model used here to describe the rotationally excited states is failing. A more sophisticated model that takes explicit account of the strong couplings present is clearly needed.

| | $E/\text{cm}^{-1}$ | Rotational constants/MHz | | $\zeta C$ | $E^{lres}_{high}(J,K,l_2)$ |
|---|---|---|---|---|---|
| | | $\bar{B}$ | $C'$ | | |
| $A_1$ | $-173.53$ | 2405.1 | $-72.1$ | | |
| $E$ | $-173.43$ | 2806.6 | 874.2 | $-271.6$ | $-1974.6$ |
| $A_1$ | $-172.75$ | 2623.6 | 667.8 | | |
| $E$ | $-172.42$ | 1687.8 | 738.1 | 716.5 | 70.1 |
| $E$ | $-171.78$ | 9965.6 | 2953.5 | 844.7 | 9273.5 |
| $A_1$ | $-171.62$ | 7717.4 | 6813.8 | | |

**Table 7.3:** Calculated rotational constants and Coriolis terms for 4 energy levels of Ar₃ immediately above the barrier to linearity.

| $\Gamma$ | $0^e e/\text{cm}^{-1}$ | $0^e o/\text{cm}^{-1}$ | $1^e e/\text{cm}^{-1}$ | $1^e o/\text{cm}^{-1}$ | $1^f e/\text{cm}^{-1}$ | $1^f o/\text{cm}^{-1}$ |
|---|---|---|---|---|---|---|
| $A_1$ | $-173.525$ | | $-173.447$ | $-173.447$ | | $-173.364$ |
| $E$ | $-173.433$ | $-173.433$ | $-173.395$ | | | |
| | | | $-173.292$ | $-173.292$ | $-173.245$ | $-173.246$ |
| | | | | $-173.263$ | | |
| $A_1$ | $-172.747$ | | $-172.637$ | $-172.637$ | | $-172.572$ |
| $E$ | $-172.425$ | $-172.425$ | $-172.392$ | $-172.391$ | $-172.312$ | $-172.312$ |
| | | | $-172.293$ | $-172.298$ | | |
| $E$ | $-171.789$ | $-171.789$ | $-171.745$ | | | |
| | | | $-171.675$ | $-171.675$ | $-171.125$ | $-171.124$ |
| $A_1$ | $-171.615$ | | $-171.130$ | $-171.130$ | | |
| | | | | $-171.126$ | | $-170.852$ |
| $E$ | $-170.176$ | $-170.176$ | $-170.994$ | $-170.994$ | $-169.169$ | $-169.169$ |
| | | | $-170.132$ | | | |
| $A_1$ | $-169.811$ | | $-169.962$ | $-169.961$ | | |
| | | | | $-169.180$ | | $-168.696$ |

**Table 7.4:** The energy levels of Ar₃ above the barrier to linearity. The states are labeled as in Fig. 7.2 with the total angular momentum $J$, the spectroscopic parity $e/f$ and the symmetry with respect to exchange of the diatom $e/o$.

CHAPTER

8

# Conclusions

The preceding chapters chronicle my development of a method of calculating all of the $J = 0$ bound states of a triatomic floppy molecule. The method was successfully applied to the prototype molecule $Ar_3$ in a study of its wave functions. A preliminary study of the $J = 1$ states of $Ar_3$ has also been carried out.

The bound-state method is based upon a potential-optimised discrete variable representation. This facilitates an efficient representation of the wave function and allows the use of a Lanczos-based diagonalisation scheme because of the sparse nature of the Hamiltonian matrix. The method uses numerically defined basis functions which allow the quadrature error that occurs as $R \to 0$ in DVR calculations to be easily corrected for. By combining successive diagonalisation and truncation with the Lanczos diagonaliser the efficiency of the originally proposed method of obtaining the energy levels and wave functions was improved. The efficiency of the method bodes well for its possible extension to the 5-dimensional systems $Ar_2HF$ and $Ar_2HCl$.

The bound-state method developed was used to calculate the $J = 0$ wave functions of $Ar_3$. The wave functions for the low lying states show quite regular character and in most cases can be assigned in terms of the normal modes of vibration of a $D_{3h}$ molecule. The wave functions of most of the states of $Ar_3$ that lie above the isomerisation barrier are irregular in character; they fill all the energetically accessible configuration space, and their wave functions have no obvious nodal pattern. However, embedded among these irregular states are some more regular states, which are more localized and have simple nodal patterns. These regular and irregular states are mixed to a greater or lesser extent, and in some cases the regular character is spread over several eigenstates. This general behaviour is similar to that observed previously for the $H_3^+$ molecular ion.

The "horseshoe" localization effect previously observed in $H_3^+$ is also present in $Ar_3$. I have also found additional types of localization effect, corresponding to symmetric and antisymmetric stretching motions about a linear configuration. If the horseshoe motion is considered as the (highly excited) bending motion of a linear molecule then all three modes of a linear molecule are apparent in the wave functions of $Ar_3$. The different localized modes can be combined to form more complex localized features in a manner similar to the combinations of normal modes found in chemically bound molecules.

The wave functions of $Ar_3$ reveal a fascinating range of dynamical behaviour. Future work in this area should lead to a better understanding of the relationship between the quantum and classical descriptions of such systems. At the moment it is possible to calculate the wave functions and explain their localized features with reference to the periodic orbits of the system. A theory in which the periodic orbits are used to predict the quantum behaviour is, however, not yet available. By studying a range of different molecules, it may be possible to develop such a theory. An especially attractive system would be $Xe_3$. The differences between $Ar_3$ and $H_3^+$ were mostly that the localisation features were more visible in $Ar_3$. If an even heavier system with a deeper potential is studied the localisation features may become more apparent and other types of motion could be discovered.

The $J = 1$ states of $Ar_3$ show that a large amount rotation-vibration cou-

pling is present in the system. Below the barrier to linearity the molecule shows quite regular behaviour in terms of its rotational constants and the increasing average size of the molecule with vibrational excitation is quite clearly observable. Above the barrier to linearity the degree of mixing between the states became so large that the simple pattern-based analysis scheme broke down and the extraction of rotational constants became impossible using this method. The expectation values provided a very accurate method of determining the value of the $\bar{B}$ rotational constant. If the more correct formula that took account of the Eckart condition were used I believe the values of $A$ and $B$ could be determined very accurately without the need for $J > 0$ calculations even for the levels above linearity. Clearly further work is needed to investigate whether this is in fact the case. For the $C$ rotational constant the strong Coriolis interactions present cloud the picture slightly. However it is clear that a formula based upon expectation values that takes account of the Coriolis coupling as well as the Eckart condition is needed to be able to predict the values of $C$ accurately. A calculation of the $J = 1$ wave functions to investigate the effect of rotation upon the localisation features would also be a very interesting future avenue to explore.

One property of $Ar_3$ that dominates its behaviour throughout this work is the barrier to linearity. It influences the dynamical calculations, the wave functions, the energy level distribution and the rotational constants. As more studies are performed the effects of such barriers on the behaviour of molecular systems should become more and more apparent. Studies of this region between strongly bound and dissociative states will provide information on the mechanisms by which molecules dissociate and react with each other. Another way of thinking of the horseshoe motion is as motion along a reactive pathway from reactant to product via a linear transition state. An understanding of these processes in simple molecules such as $Ar_3$ should lead to much better models for chemical reaction dynamics.

# BIBLIOGRAPHY

[1] A. J. Stone, *The theory of intermolecular forces* (Oxford University Press, Oxford, 1996).

[2] J. M. Hutson, Ann. Rev. Phys. Chem. **41**, 123 (1990).

[3] D. J. Nesbitt, Ann. Rev. Phys. Chem. **45**, 367 (1994).

[4] C. Tessier, A. Terlain, and Y. Larher, Physica A **113**, 286 (1982).

[5] A. R. Cooper and J. M. Hutson, J. Chem. Phys. **98**, 5337 (1993).

[6] M. J. Elrod and R. J. Saykally, Chem. Rev. **94**, 1975 (1994).

[7] A. Ernesti and J. M. Hutson, J. Chem. Phys. **103**, 3386 (1995).

[8] A. Ernesti and J. M. Hutson, J. Chem. Phys. **106**, 6288 (1997).

[9] E. B. Wilson, J. C. Decius, and P. C. Cross, *Molecular vibrations. The theory of infrared and Raman Vibrational spectra* (Dover, New York, 1955).

[10] J. K. G. Watson, J. Mol. Spectrosc. **103**, 350 (1984).

[11] Y. Xu, W. Jäger, and M. C. L. Gerry, J. Chem. Phys. **100**, 4171 (1994).

[12] Y. Xu and W. Jäger, J. Chem. Phys. **107**, 1788 (1997).

[13] R. A. Aziz, J. Chem. Phys. **99**, 4518 (1993).

[14] J. M. Hutson, J. Phys. Chem. **96**, 4237 (1992).

[15] J. M. Hutson, J. Chem. Phys. **96**, 6752 (1992).

[16] C.-C. Chuang *et al.*, J. Chem. Phys. **107**, 7041 (1997).

[17] J. T. Farrell Jr. and D. J. Nesbitt, J. Chem. Phys. **105**, 9421 (1996).

[18] A. McIlroy, R. Lascola, C. M. Lovejoy, and D. J. Nesbitt, J. Phys. Chem. **95**, 2636 (1991).

[19] Z. Bačić and J. C. Light, Annu. Rev. Phys. Chem. **40**, 469 (1989).

[20] J. C. Light, I. P. Hamilton, and J. V. Lill, J. Chem. Phys. **82**, 1400 (1985).

[21] J. R. Henderson, J. Tennyson, and B. T. Sutcliffe, J. Chem. Phys. **98**, 7191 (1993).

[22] M. J. Bramley, J. W. Tromp, T. Carrington Jr., and G. C. Corey, J. Chem. Phys. **100**, 6175 (1994).

[23] V. A. Mandelshtam and H. S. Taylor, J. Chem. Soc. Faraday Trans. **93**, 847 (1997).

[24] J. Tennyson and J. R. Henderson, J. Chem. Phys. **91**, 3815 (1989).

[25] J. R. Henderson and J. Tennyson, Chem. Phys. Lett. **173**, 133 (1990).

[26] C. R. Le Sueur, J. R. Henderson, and J. Tennyson, Chem. Phys. Lett. **206**, 429 (1993).

[27] G. García de Polavieja, N. Fulton, and J. Tennyson, Mol. Phys. **83**, 361 (1994).

[28] D. A. Sadovski *et al.*, J. Chem. Phys. **99**, 906 (1993).

[29] T. R. Horn, R. B. Gerber, J. J. Valentini, and M. A. Ratner, J. Chem. Phys. **94**, 6728 (1991).

[30] D. M. Leitner, R. S. Berry, and R. M. Whitnell, J. Chem. Phys. **91**, 3470 (1989).

[31] A. R. Cooper, S. Jain, and J. M. Hutson, J. Chem. Phys. **98**, 2160 (1993).

[32] R. Bryan, Ph.D. thesis, University of Durham, 1997.

[33] J. Tennyson and B. T. Sutcliffe, J. Mol. Spectrosc. **101**, 71 (1983).

[34] R. T. Pack and G. A. Parker, J. Chem. Phys. **87**, 3888 (1987).

[35] S. Carter and N. C. Handy, Comp. Phys. Reports **5**, 115 (1986).

[36] B. R. Johnson and W. P. Reinhardt, J. Chem. Phys. **85**, 4538 (1986).

[37] B. R. Johnson, J. Chem. Phys. **69**, 4678 (1978).

[38] J. M. Hutson, Comput. Phys. Comm. **84**, 1 (1988).

[39] D. O. Harris, G. G. Engerholm, and W. D. Gwinn, J. Chem. Phys. **43**, 1515 (1965).

[40] A. S. Dickinson and P. R. Certain, J. Chem. Phys. **49**, 4209 (1968).

[41] R. J. Le Roy and J. S. Carley, Adv. Chem. Phys. **42**, 353 (1980).

[42] J. Echave and D. C. Clary, Chem. Phys. Lett. **190**, 225 (1992).

[43] J. Tennyson and B. T. Sutcliffe, J. Chem. Phys. **77**, 4061 (1982).

[44] S. E. Choi and J. C. Light, J. Chem. Phys. **92**, 2129 (1990).

[45] J. M. Hutson *et al.*, J. Chem. Phys. **105**, 9130 (1996).

[46] R. T Pack and G. A. Parker, J. Chem. Phys. **87**, 3888 (1987).

[47] E. Yurtsever, O. Yilmaz, and D. D. Shillady, Chem. Phys. Lett. **85**, 111 (1982).

[48] R. J. Le Roy, University Of Waterloo Chemical Physics Research Report **CP-555**, (1995).

[49] R. N. Zare, *Angular Momentum* (John Wiley, New York, 1988).

[50] M. Abramowitz and I. E. Stegun, *Handbook of Mathematical Functions* (Dover, New York, 1965).

[51] H. Y. Mussa, J. Tennyson, C. J. Noble, and R. J. Allan, Comput. Phys. Comm. **108**, 29 (1998).

[52] J. Tennyson and B. T. Sutcliffe, Mol. Phys. **58**, 1067 (1986).

[53] J. V. Lill, G. A. Parker, and J. C. Light, J. Chem. Phys. **85**, 900 (1986).

[54] M. J. Weida, J. M. Sperhac, D. J. Nesbitt, and J. M. Hutson, J. Chem. Phys. **101**, 8351 (1994).

[55] Routine F02FAF from the NAG FORTRAN Library, Mark 16 (1993), supplied by the Numerical Algorithms Group, Oxford, UK.

[56] J. R. Henderson, C. R. Le Sueur, S. G. Pavett, and J. Tennyson, Comput. Phys. Comm. **74**, 193 (1993).

[57] D. S. Watkins, *Fundamentals of matrix computations* (Wiley, New York, 1991).

[58] D. C. Sorensen, SIAM J. Matrix Anal. Appl. **13**, 357 (1992).

[59] R. B. Lehoucq, K. Maschoff, D. C. Sorensen, and C. Yang, ARPACK, is available from
ftp://ftp.caam.rice.edu/pub/software/ARPACK.

[60] R. B. Lehoucq, K. Maschoff, D. C. Sorensen, and C. Yang, ARPACK, for more details see: http://www.caam.rice.edu/software/ARPACK/ .

[61] P. P. Korambath, X. T. Wu, and E. F. Hayes, J. Phys. Chem. **100**, 6116 (1996).

[62] X. T. Wu and E. F. Hayes, J. Chem. Phys. **107**, 2705 (1997).

[63] C. Lawson, R. Hanson, D. Kincaid, and F. Krogh, ACM Trans. Math. Softw. **5**, 308 (1979).

[64] M. J. Bramley and T. Carrington Jr., J. Chem. Phys. **99**, 8519 (1993).

[65] J. Tennyson and B. T. Sutcliffe, J. Mol. Spectrosc. **101**, 71 (1983).

[66] H. Wei, J. Chem. Phys. **106**, 6885 (1997).

[67] J. Tennyson, Private communication.

[68] R. Prosmiti, H. Y. Mussa, and J. Tennyson, in *Molecular quantum states at dissociation, ISBN 0-9522736-5-9*, edited by R. Prosmiti, J. Tennyson, and D. C. Clary (Collaborative Computational Project No.6 of the UK Engineering and Physical Sciences Research Council, Daresbury, 1998).

[69] J. K. Cullum and R. A. Willoughby, *Lanczos Algorithms for Large Symmetric Eigenvalue computations* (Birkhäuser, Boston, 1985).

[70] F. Göğtas and G. G. Balint-Kurti and A. R. Offer, J. Chem. Phys. **104**, 7927 (1996).

[71] O. Brass, J. Tennyson, and E. Pollak, J. Chem. Phys. **92**, 3377 (1990).

[72] J. R. Henderson and J. Tennyson, Mol. Phys. **69**, 639 (1990).

[73] J. R. Henderson, H. A. Lam, and J. Tennyson, J. Chem. Soc. Faraday Trans. **88**, 3287 (1992).

[74] G. Garćia de Polavieja, N. Fulton, and J. Tennyson, Mol. Phys. **87**, 651 (1996).

[75] M. Bixon and J. Jortner, J. Chem. Phys. **50**, 3284 (1969).

[76] J. Tennyson, O. Brass, and E. Pollak, J. Chem. Phys. **92**, 3005 (1990).

[77] J. M. Gomez Llorente and E. Pollak, Ann. Rev. Phys. Chem. **43**, 91 (1992).

[78] S. C. Farantos, Int. Rev. Phys. Chem. **15**, 345 (1996).

[79] in *Les Houches Lectures LII: Chaos and quantum physics*, edited by M. J. Giannoni, A. Voros, and J. Zinn-Justin (North Holland, North Holland, 1991), p. 547.

[80] K. M. Atkins and J. M. Hutson, J. Chem. Phys. **103**, 9218 (1995).

[81] G. Herzberg, *Molecular Spectra and Molecular Structure, II. Infrared and Raman Spectra of Polyatomic molecules* (Krieger, Florida, 1991).

[82]  T. Oka, J. Chem. Phys. **47**, 5410 (1967).

[83]  A. Ernesti and J. M. Hutson, Chem. Phys. Lett. **222**, 257 (1994).

# APPENDIX

## A

# Conferences, Courses and Seminars Attended

Royal Society of Chemistry High Resolution Spectroscopy Group. Conference on High Resolution Spectroscopy (Annual meeting of the HRSG).
Reading University, 17th-19th December 1995.

6th Annual Informal Northern Universities Meeting on Chemical Physics.
Newcastle University 4th July 1996.

Charles Coulson Summer School in Theoretical Chemistry.
Oxford University 8th-18th September 1996.

Photoionisation Dynamics, Rydberg States and Large Amplitude Motion.
University of York 3rd-5th November 1996.

Optical, Electric and Magnetic properties of molecules: A conference to celebrate the career of Prof. A. D. Buckingham.
University of Cambridge. 4th-8th July 1997.

Second European Computational Chemistry Conference.
University of Lisbon. 2nd-6th September 1997.

The Dynamics of Electronically-Excited States in Gaseous, Cluster and condensed media. Faraday Discussion 108.
University of Sussex. 15th-17th December 1997.

Royal Society of Chemistry High Resolution Spectroscopy Group. Conference on High Resolution Spectroscopy (Annual meeting of the HRSG).
Exeter University, 17th-19th December 1997.

Molecular and Ionic Clusters.  Gordon Conference in Ventura California. (Poster presented 'Vibrational eigenstates of Van der Waals trimers'.) 3rd-8th January 1998

Fashioning a model: Optimisation methods in chemical physics.
University of Durham. 24th-27th March 1998.

Molecular quantum states at dissociation.
University College London. 28th-30th June 1998.

. . . . . . . . . . . . . . . . . . . . . . . . . . . . . . .

The following pages contain lists of the seminars in the chemistry department from 1995-1998. Those marked with an asterisk were attended.

**1995 - 1996**

1995

October 11 * Prof. P. Lugar, Frei Univ Berlin, FRG
Low Temperature Crystallography

October 13 Prof. R. Schmutzler, Univ Braunschweig, FRG.
Calixarene-Phosphorus Chemistry: A New Dimension in Phosphorus Chemistry

October 18 Prof. A. Alexakis, Univ. Pierre et Marie Curie, Paris,
Synthetic and Analytical Uses of Chiral Diamines

October 25 Dr.D.Martin Davies, University of Northumbria
Chemical reactions in organised systems.

November 1 Prof. W. Motherwell, UCL London

New Reactions for Organic Synthesis

November 3 Dr B. Langlois, University Claude Bernard-Lyon

Radical Anionic and Pseudo Cationic Trifluoromethylation

November 8 Dr. D. Craig, Imperial College, London

New Strategies for the Assembly of Heterocyclic Systems

November 15 Dr Andrea Sella, UCL, London

Chemistry of Lanthanides with Polypyrazoylborate Ligands

November 17* Prof. David Bergbreiter, Texas A&M, USA

Design of Smart Catalysts, Substrates and Surfaces from Simple Polymers

November 22 * Prof. I Soutar, Lancaster University

A Water of Glass? Luminescence Studies of Water-Soluble Polymers.

November 29 Prof. Dennis Tuck, University of Windsor, Ontario, Canada

New Indium Coordination Chemistry

December 8 Professor M.T. Reetz, Max Planck Institut, Mulheim

Perkin Regional Meeting

1996

January 10 * Dr Bill Henderson, Waikato University, NZ

Electrospray Mass Spectrometry - a new sporting technique

January 17 * Prof. J. W. Emsley , Southampton University

Liquid Crystals: More than Meets the Eye

January 24 Dr Alan Armstrong, Nottingham University

Alkene Oxidation and Natural Product Synthesis

January 31* Dr J. Penfold, Rutherford Appleton Laboratory,

Soft Soap and Surfaces

February 7 Dr R.B. Moody, Exeter University

Nitrosations, Nitrations and Oxidations with Nitrous Acid

February 12 Dr Paul Pringle, University of Bristol

Catalytic Self-Replication of Phosphines on Platinum(O)

February 14 Dr J. Rohr, Univ Gottingen, FRG

Goals and Aspects of Biosynthetic Studies on Low Molecular Weight Natural Products

February 21 Dr C R Pulham , Univ. Edinburgh

Heavy Metal Hydrides - an exploration of the chemistry of stannanes and plumbanes

February 28* Prof. E. W. Randall, Queen Mary & Westfield College

New Perspectives in NMR Imaging

March 6 Dr Richard Whitby, Univ of Southampton

New approaches to chiral catalysts: Induction of planar and metal centred asymmetry

March 7 Dr D.S. Wright, University of Cambridge

Synthetic Applications of Me2N-p-Block Metal Reagents

March 12* RSC Endowed Lecture - Prof. V. Balzani, Univ of Bologna

Supramolecular Photochemistry

March 13 Prof. Dave Garner, Manchester University

Mushrooming in Chemistry

April 30 Dr L.D.Pettit, Chairman, IUPAC Commission of Equilibrium Data

pH-metric studies using very small quantities of uncertain purity

**1996 - 1997**

1996

October 9 Professor G. Bowmaker, University Aukland, NZ

Coordination and Materials Chemistry of the Group 11 and Group 12 Metals: Some Recent Vibrational and Solid State NMR Studies

October 14 Professor A. R. Katritzky, University of Gainesville,

University of Florida, USA

Recent Advances in Benzotriazole Mediated Synthetic Methodology

October 16 Professor Ojima, Guggenheim Fellow, State University of New York at Stony Brook

Silylformylation and Silylcarbocyclisations in Organic Synthesis

October 22 Professor Lutz Gade, Univ. Wurzburg, Germany

Organic transformations with Early-Late Heterobimetallics: Synergism and Selectivity

October 22 * Professor B. J. Tighe, Department of Molecular Sciences and Chemistry, University of Aston

Making Polymers for Biomedical Application - can we meet Nature's Challenge? Joint lecture with the Institute of Materials

October 23 Professor H. Ringsdorf (Perkin Centenary Lecture)

Johannes Gutenberg-Universitat, Mainz, Germany

Function Based on Organisation

October 29 * Professor D. M. Knight, Department of Philosophy, University of Durham.

The Purpose of Experiment - A Look at Davy and Faraday

October 30 Dr Phillip Mountford, Nottingham University

Recent Developments in Group IV Imido Chemistry

November 6 Dr Melinda Duer, Chemistry Department, Cambridge

Solid-state NMR Studies of Organic Solid to Liquid-crystalline Phase Transitions

November 12 * Professor R. J. Young, Manchester Materials Centre, UMIST

New Materials - Fact or Fantasy?

Joint Lecture with Zeneca & RSC

November 13 Dr G. Resnati, Milan

Perfluorinated Oxaziridines: Mild Yet Powerful Oxidising Agents

November 18 Professor G. A. Olah, University of Southern California, USA

Crossing Conventional Lines in my Chemistry of the Elements

November 19 Professor R. E. Grigg, University of Leeds

Assembly of Complex Molecules by Palladium-Catalysed Queueing Processes

November 20 Professor J. Earnshaw, Department of Physics, Belfast

Surface Light Scattering: Ripples and Relaxation

November 27 Dr Richard Templer, Imperial College, London

Molecular Tubes and Sponges

December 3 * Professor D. Phillips, Imperial College, London
"A Little Light Relief" -

December 4 * Professor K. Muller-Dethlefs, York University
Chemical Applications of Very High Resolution ZEKE Photoelectron Spectroscopy

December 11 Dr Chris Richards, Cardiff University
Stereochemical Games with Metallocenes

1997

January 15 Dr V. K. Aggarwal, University of Sheffield
Sulfur Mediated Asymmetric Synthesis

January 16 Dr Sally Brooker, University of Otago, NZ
Macrocycles: Exciting yet Controlled Thiolate Coordination Chemistry

January 21 Mr D. Rudge, Zeneca Pharmaceuticals
High Speed Automation of Chemical Reactions

January 22 Dr Neil Cooley, BP Chemicals, Sunbury
Synthesis and Properties of Alternating Polyketones

January 29 Dr Julian Clarke, UMIST
What can we learn about polymers and biopolymers from
computer-generated nanosecond movie-clips?

February 4 Dr A. J. Banister, University of Durham
From Runways to Non-metallic Metals - A New Chemistry Based on Sulphur

February 5 Dr A. Haynes, University of Sheffield
Mechanism in Homogeneous Catalytic Carbonylation

February 12 Dr Geert-Jan Boons, University of Birmingham
New Developments in Carbohydrate Chemistry

February 18 * Professor Sir James Black, Foundation/King's College London
My Dialogues with Medicinal Chemists

February 19 Professor Brian Hayden, University of Southampton
The Dynamics of Dissociation at Surfaces and Fuel Cell Catalysts

February 25 Professor A. G. Sykes, University of Newcastle

The Synthesis, Structures and Properties of Blue Copper Proteins

February 26 Dr Tony Ryan, UMIST

Making Hairpins from Rings and Chains

March 4 Professor C. W. Rees, Imperial College

Some Very Heterocyclic Chemistry

March 5 Dr J. Staunton FRS, Cambridge University

Tinkering with biosynthesis: towards a new generation of antibiotics

March 11 * Dr A. D. Taylor, ISIS Facility, Rutherford Appleton Laboratory

Expanding the Frontiers of Neutron Scattering

March 19 * Dr Katharine Reid, University of Nottingham

Probing Dynamical Processes with Photoelectrons

**1997 - 1998**

1997

October 8 Prof. E. Atkins, Department of Physics, University of Bristol

Advances in the control of architecture for polyamides: from nylons to genetically engineered silks to monodisperse oligoamides

October 15 Dr. R. Mark Ormerod, Department of Chemistry, Keele University

Studying catalysts in action

October 21 Prof. A. F. Johnson, IRC, Leeds

Reactive processing of polymers: science and technology

October 22 Prof. R.J. Puddephatt (RSC Endowed Lecture),

University of Western Ontario

Organoplatinum chemistry and catalysis

October 23* Prof. M.R. Bryce, University of Durham, Inaugural Lecture

New Tetrathiafulvalene Derivatives in Molecular, Supramolecular and Macromolecular Chemistry: controlling the electronic properties of organic solids

October 29 Prof. Bob Peacock, University of Glasgow

Probing chirality with circular dichroism

October 28 Prof. A P de Silva, The Queen's University, Belfast
Luminescent signalling systems

November 5 Dr Mimi Hii, Oxford University
Studies of the Heck reaction

November 11* Prof. V Gibson, Imperial College, London
Metallocene polymerisation

November 12* Dr Jeremy Frey, Department of Chemistry, Southampton University
Spectroscopy of liquid interfaces: from bio-organic chemistry to atmospheric chemistry

November 19* Dr Gareth Morris, Department of Chemistry, Manchester Univ.
Pulsed field gradient NMR techniques: Good news for the Lazy and DOSY

November 20 Dr Leone Spiccia, Monash University, Melbourne, Australia
Polynuclear metal complexes

November 25 Dr R. Withnall, University of Greenwich
Illuminated molecules and manuscripts

November 26* Prof. R.W. Richards, University of Durham, Inaugural Lecture
A random walk in polymer science

December 2 Dr C.J. Ludman, University of Durham
Explosions

December 3 Prof. A.P. Davis, Department. of Chemistry,
Trinity College Dublin.
Steroid-based frameworks for supramolecular chemistry

December 10* Sir Gordon Higginson, former Professor of Engineering in
Durham and retired Vice-Chancellor of Southampton Univ.
1981 and all that.

December 10 Prof. Mike Page, Department of Chemistry,
University of Huddersfield
The mechanism and inhibition of beta-lactamases

1998

January 14 Prof. David Andrews, University of East Anglia
Energy transfer and optical harmonics in molecular systems

January 20 Prof. J. Brooke, University of Lancaster
What's in a formula? Some chemical controversies of the 19th century

January 21 Prof. David Cardin, University of Reading

January 27 Prof. Richard Jordan, Dept. of Chemistry, Univ. of Iowa, USA.
Cationic transition metal and main group metal alkyl complexes in olefin polymerisation

January 28 Dr Steve Rannard, Courtaulds Coatings (Coventry)
The synthesis of dendrimers using highly selective chemical reactions

February 3 Dr J. Beacham, ICI Technology
The chemical industry in the 21st century

February 4* Prof. P. Fowler, Department of Chemistry, Exeter University
Classical and non-classical fullerenes

February 11 Prof. J. Murphy, Dept of Chemistry, Strathclyde University

February 17 Dr S. Topham, ICI Chemicals and Polymers
Perception of environmental risk; The River Tees, two different rivers

February 18* Prof. Gus Hancock, Oxford University
Surprises in the photochemistry of tropospheric ozone

February 24 Prof. R. Ramage, University of Edinburgh
The synthesis and folding of proteins

February 25 Dr C. Jones, Swansea University
Low coordination arsenic and antimony chemistry

March 4 Prof. T.C.B. McLeish, IRC of Polymer Science Technology,
Leeds University
The polymer physics of pyjama bottoms (or the novel rheological characterisation of long branching in entangled macromolecules)

March 11 Prof. M.J. Cook, Dept of Chemistry, UEA
How to make phthalocyanine films and what to do with them.

March 17 Prof. V. Rotello, University of Massachusetts, Amherst

The interplay of recognition & redox processes - from flavoenzymes to devices

March 18* Dr John Evans, Oxford University

Materials which contract on heating (from shrinking ceramics to bullet proof vests).